Università degli Studi di Padova

Dipartimento di Fisica e Astronomia "Galileo Galilei"

Corso di Laurea Magistrale in Astronomia

Spatial Variation of Stellar Ages in GASP

Galaxies Observed with MUSE

Relatore
Prof. Giulia Rodighiero
Università di Padova

Co-Relatore
Dr. Marco Gullieuszik
INAF-OAPd

Laureando
Aishwarya Girdhar
Astromundus

Contro-Relatore
Dr. Paolo Cassata
Università di Padova

Anno Academico 2018-2019

"All things in the universe are constantly engaged in challenge.
All things quietly and tenaciously persevere,
working unceasingly to fulfill their unique mission."
- Dr. Daisaku Ikeda

Abstract

The question of how and where galaxies build up their mass over time by converting their gas into stars is key to the understanding of galaxy evolution. In the hierarchical model of galaxy evolution, galaxies are thought to build their mass through inside-out growth (negative age gradients). This theoretical picture is widely supported for high-mass galaxies. However, in low-mass disk galaxies, star formation is seen to proceed through outside-in growth (positive age gradients) or equally at all radii (flat-gradients).

The GASP program provides high-quality integral field spectroscopic data observed with MUSE, which can be used to investigate this issue. GASP is an ESO large program that was awarded 120 hours to observe 114 galaxies at z $\sim$ 0.04-0.1, with MUSE. This thesis probes 34 regular and undisturbed GASP galaxies, with the aim to study the spatially resolved star formation history (SFH) and the connection of the stellar mass growth to the global and spatially resolved galactic properties. It improves upon the current research in this field by quantifying the rate at which mass is being built from star formation by estimating the age-gradients and thus being able to differentiate between the inside-out and outside-in scenarios. A transition of growth mechanism is witnessed from outside-in to inside-out as the stellar mass increases. A critical mass limit of M_*=$10^{10.15}$ $M_\odot$ is identified in agreement with previous studies beyond which only negative age-gradients are seen. These galaxies also comply with the downsizing argument indicating that more massive galaxies are also older. On disentangling the sample into galaxies with and without a bulge, both the luminosity-weighted and mass-weighted age gradients of galaxies with bulge are found to show a more negative correlation with respect to M_*, as compared to the entire sample. Contrary to this, the bulgeless galaxies show a positive correlation with respect to M_*. This work can be extended to the analysis of galaxies at different evolutionary phases which can thus help to form a complete picture of galaxy evolution.

Contents

Listing of figures

Listing of tables

"The surface of the Earth is the shore of the cosmic ocean. From it we have learned most of what we know. Recently, we have waded a little out to sea, enough to dampen our toes or, at most, wet our ankles. The water seems inviting."

- Carl Sagan

1 Introduction

GALAXIES ARE A BEAUTIFUL and complex mix of stars, gas, dust, and dark matter in varying proportions that make up the disk, bulge, and halo of the galaxy. Studying the present day structure and dynamics of these components can help us understand their assembly and evolution over the history of the Universe.

Thanks to a large number of imaging and spectroscopic surveys, the knowledge of galaxies has drastically increased in the past two decades. We are now able to observe galaxies at redshifts up to $z \sim 7$, and can also find plausible candidates at even higher redshifts (Schneider, 2006). We can thus observe galaxies at nearly all epochs of cosmic evolution. However, even though we observe the galaxy population throughout 90% of the cosmic history, we cannot suppose that galaxies seen at different redshifts represent various subsequent stages of evolution of the same kind of galaxy. The main reason for this difficulty is that different selection criteria need to be applied to find galaxies at different redshifts. This means that we are actually seeing different galaxies all together at different redshifts and not the same galaxy at different times. However, galaxy evolution models provide us simulations of the same galaxy over different times. To understand galaxy evolution, we need to understand what in galaxy's history resulted in it to have the present properties like stellar mass (M_*), Star Formation Rate (SFR), etc. This can only be done through a combined study of the observed data and the models.

Through this thesis, an attempt has been made to understand galaxy evolution by using observations of galaxies at nearby redshifts combined with models that help us break down the observations to different time-frames.

1.1 Galaxy Evolution: How galaxies build their mass

The question of how and where galaxies build up their mass over time is key to the understanding of galaxy evolution. In presence of favourable conditions for star formation (SF), galaxies can grow in mass through the conversion of available gas into stars (in-situ). Galaxies can also grow in stellar mass by the accretion of stars via galaxy mergers and tidal stripping of smaller satellite galaxies (ex-situ). Simulations suggest that the majority of galaxies in the Universe, with M_*< few times 10^{11} $M_\odot$, grow primarily through in-situ star formation (Rodriguez-Gomez et al., 2016).

The work in this thesis is based on the undisturbed and regular galaxies, selected from the galaxy sample of GASP survey, that are growing their mass through star formation.

1.1.1 The different formation scenarios

Galaxies appear to assemble their stellar mass mainly in two distinct modes: "**inside-out**" and "**outside-in**" (Pérez et al. 2013; Ibarra-Medel et al. 2016; Pan et al. 2015; Goddard et al. 2017).

1. **Inside Out Mode**
   In the hierarchical model of galaxy evolution, galaxies are thought to build their mass through the inside-out growth mechanism (IO) (White & Frenk 1991; Kauffmann et al. 1993; Mo et al. 1998; Roškar et al. 2008), i.e., mass assembly is first finished in the galactic central region.

   Consider a young disk galaxy; the disk instability in it will induce gas inflow and trigger starburst in the galactic center as it evolves. Other than fuelling star formation, the inflow gas can also fuel the central supermassive blackhole. The subsequent AGN feedback (such as blowing the gas out of the galaxy, or heating it against cooling down to form new stars) will then suppress the central star formation, leaving a compact, quiescent galactic bulge (Dekel & Burkert 2014; Bournaud et al. 2014). In these galaxies, we can see that compared to their central parts, the outskirts form through much gentler processes, such as the star formation driven by the gradual accretion of cold

inter-galactic medium (IGM), or the accretion of small satellite galaxies.

2. **Outside In Mode**
   Compared to their massive counterparts, low mass galaxies have much shallower potential wells, making them less capable to retrieve the gas lost by the galactic outflows, or accrete cold gas to form new stars. In addition, the role of AGN feedback may not be so efficient in low mass galaxies, as their AGN occupation fraction is very low (Kauffmann et al. 2003b). Thus it is no surprise to see the low mass galaxies evolve through a different mass assembly mode. In fact, observations support that the evolution of low mass galaxies can be better interpreted in an "outside-in" framework (Gallart et al. 2008; Zhang et al. 2012).

While evidence for both these scenarios is seen, it has been difficult to ascertain the true physical causes behind each of these phenomena. Thus the formation and evolution of galaxies remains as one of the key problems in modern astrophysics. Observations with an increased spatial resolution can help understand the complex physics of star formation and suppression in galaxies and the interplay of SF with dark and baryonic matter. However, the spatially resolved stellar mass assembly histories of galaxies are still poorly understood. The biggest advancements in this field have been thanks to the advent of integral field spectroscopy.

1.2 Integral Field Spectroscopy

The spatial distribution of stellar populations in galaxies has been studied for several decades, starting with earliest work by Faber & Dressler (1977) on radial gradients of colours and absorption line-strength indices.

The early spectroscopic studies of the stellar populations with large galaxy samples, were mostly limited to spatially unresolved studies using single fibre spectroscopy (e.g. Kauffmann et al. 2003a; Brinchmann et al. 2004; Gallazzi et al. 2005). Single fibre spectroscopy only samples the inner parts of the galaxy and is prone to aperture bias depending on the redshift range of the sample (Kewley et al. 2005; Pracy et al. 2012; Brough et al. 2013; Richards et al. 2016). Another method is to use broad-band photometry, since it can be used for resolved studies (e.g. Bell & de Jong 2000; Muñoz-Mateos et al. 2007; Wang et al. 2011; Fang et al. 2012). However, with this method, the detailed studies of the stellar populations remains limited due to the larger uncertainty on parameters such as stellar population age. Another suitable method to study the stellar population properties is through long-slit spectroscopy.

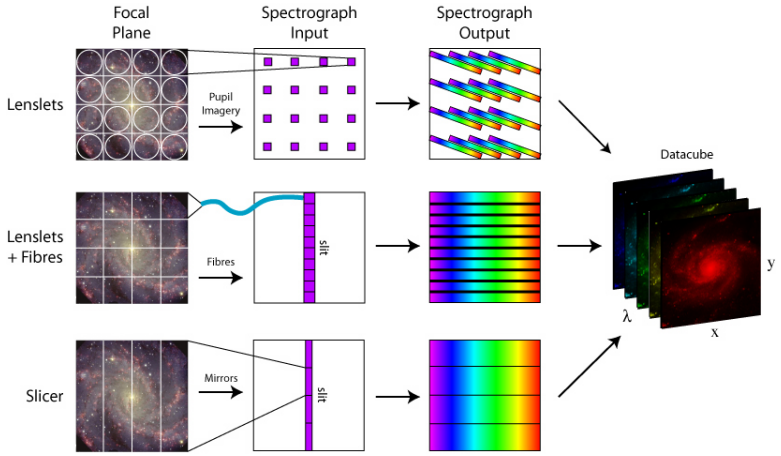

Figure 1.1: Schematic diagram describing the different IFS designs and the final 3D spectra obtained.

Using this technique, we can study the long-slit cross-sections of galaxies in different orientations which provide details to the stellar components as well as for the gaseous components through the strong emission lines.

A big leap came about with the advent of **Integral Field Spectroscopy (IFS)**, providing 3D information (2D spatial + 1D spectral) on galaxies. Hence with IFS, we have the opportunity to perform two-dimensional spatial studies on nearby galaxies and to acquire hundreds of spectra for each pixel of the observation which cover the galaxy from the centre to the outskirt, with a wide wavelength coverage. Figure 1.1 shows the different IFS designs that produce a 3D spectra of an extended object.

Initial integral-field-unit (IFU) surveys focused on small numbers of specifically selected galaxies (e.g. SAURON, Bacon et al. 2001; Davies et al. 2001; ATLAS 3D, Cappellari et al. 2011; DiskMass, Bershady et al. 2010). Long slit spectroscopic studies of galaxies were undertaken for more representative samples of galaxies by Moran et al. 2012 and Huang et al. 2013, however samples were limited to relatively small numbers (~ 100) with a limited mass range ($M_* > 10^{10} M_\odot$).

Recently, several large IFS surveys have been performed, such as ATLAS 3D Cappellari et al. 2011, Calar Alto Large Integral Field Area (CALIFA; Sánchez et al. 2012), the Sydney Australian Astronomical Observatory Multi-object Integral Field Spectrograph (SAMI; Bryant et al. 2015), Mapping Nearby Galaxies at the Apache Point Observatory (MaNGA; Bundy et al. 2015), and GAs Stripping Phenomena in galaxies (GASP; Poggianti et al. 2017b). These programs have enabled the community to study the spatially resolved mass assembly histories of galaxies. We look into these programs in brief detail before going to a description

of GASP in Chapter 2.

1.2.1 Calar Alto Legacy Integral Field Area Survey (CALIFA)

The Calar Alto Legacy Integral Field Area Survey has obtained spatially resolved spectroscopic information of a sample of 667 galaxies in the local universe (0.005< z <0.03). CALIFA was designed to allow the building of two-dimensional maps of the following quantities: (a) stellar populations: ages and metallicities; (b) ionized gas: distribution, excitation mechanism and chemical abundances; and (c) kinematic properties: both from stellar and ionized gas components. CALIFA used the PPAK Integral Field Unit (Kelz et al. 2006), of the Potsdam Multi-Aperture Spectrograph (PMAS; Roth et al. 2006) instrument at the 3.5m telescope of Centro Astronómico Hispano Alemán (CAHA) at Calar Alto, Spain.

The IFU has a hexagonal field-of-view of ~1.3 arcmin^2, with a 100% covering factor. The optical wavelength range is covered from 3700 to 7000 Å, using two overlapping setups (V500 and V1200), with different spectral resolutions: R~850 and R~1650, respectively. These integral field spectra, have been supplied by periodic data releases (Husemann et al. 2013; García-Benito et al. 2015; Sánchez et al. 2016) to the public, and they provide an important contribution to understand evolutionary processes which occur in galaxies like merging and secular mechanisms, environment effects, star formation history and Active Galaxy Nuclei (AGN) influence.

1.2.2 Mapping Nearby Galaxies at Apache Point Observtory (MaNGA)

The MaNGA survey started as a result of the demand to extend the IFS research to a wider sample of galaxies. This led to the forth-generation Sloan Digital Sky Survey (SDSS) team (Blanton et al. 2017) to start MaNGA with the ambitious purpose of obtaining integral field spectra of a sample of 10,000 galaxies at low redshifts. MaNGA makes use of an instrumental system consisting of the 2.5m Sloan Telescope in its spectroscopic mode (Gunn et al. 2006), a set of 17 hexagonal fiber bundle IFUs (Drory et al. 2015) and the BOSS spectrographs covering a long, continuous wavelength range, from 3600 to 10300 Å with a resolution R ~ 2000 (Smee et al. 2013). The observation targets span a wide range of environments with $M_*>10^9 M_\odot$ and redshifts of 0.01 to 0.18. The MaNGA released sample is mainly composed of the "primary" (~2/3) and "secondary" (~1/3) samples (SDSS Collaboration et al. 2017), which are defined by two radial coverage goals, in terms of effective radius (R_e): the former of 1.5 R_e, and the latter of 2.5 R_e.

MaNGA was started with the aim to probe gas ionization, shed light on recent star formation and quenching, enable dynamical modeling, decompose constituent components, and map the composition of stellar populations.

1.2.3 Sydney Australian Astronomical Observatory Multi-object Integral Field Spectrograph (SAMI)

The SAMI Galaxy Survey has observed 3400 galaxies with the Sydney-AAO Multi-object Integral-field spectrograph (SAMI; Croom et al. 2012) on the Anglo-Australian Telescope (AAT). The survey has galaxies selected from the Galaxy And Mass Assembly survey (GAMA; Driver et al. 2009, 2011). The targets have been selected to cover a broad range in stellar mass and environment, thus covering redshifts $0.004 < z < 0.113$, stellar masses in range of $7.5<\log(M_*/M_\odot)<11.6$, and environments from isolated field galaxies to groups and to clusters of $\sim 10^{15}$ $M_\odot$.

The main scientific driver of this survey has been the investigation of how both mass and angular momentum build in galaxies and the mechanisms driving gas into and out of galaxies, and the impact of these gas flows on star formation.

1.3 Current status of research in this field

For the first time, multi-object IFU observations from these surveys are allowing the study of the spatially resolved stellar populations and ionised gas in large, unbiased samples of galaxies spanning a wide mass range. Most studies determining stellar mass growth now rely on full-spectrum fitting with stellar population synthesis models to obtain the star formation histories of galaxy regions.

- By applying the fossil record method to 105 CALIFA galaxies, Pérez et al. (2013) found that the spatially resolved stellar mass assembly pattern of local galaxies depends on the global stellar mass. Specifically, massive galaxies grow their stellar mass inside-out, while less massive galaxies show a transition to outside-in growth.

- In agreement with this, Pan et al. (2015) proposed that the typical galaxy assembly mode is transitioning from outside-in to inside-out from low to high stellar masses, indicated by the NUV - r color gradients of ~10,000 low-redshift galaxies.

- By analyzing 533 galaxies selected from MaNGA, Ibarra-Medel et al. (2016) generated the global and radial stellar mass growth histories with the fossil record method and confirmed that the massive SF galaxies, on average, show a pronounced inside-out

mass assembly mode. They also found that the less massive galaxies show diverse mass assembly histories, with periods of both outside-in and inside-out modes.

- González Delgado et al. (2015, 2016), generated maps of the mean stellar age and metallicity for 416 galaxies from CALIFA and found that the negative gradients of light-weighted stellar age are consistent with the inside-out growth of galaxies, especially for Sb-Sbc galaxies. These findings agree well with the negative stellar age gradients for massive SF galaxies as found by others (e.g., Wang et al. 2011; Lin et al. 2013; Li et al. 2015; Dale et al. 2016; Goddard et al. 2017).

- Rowlands et al. (2018) explored the influence of galaxy physical properties (M_*, morphology) on star formation histories for 2404 MaNGA galaxies. They found that the spatial distribution of SF is dependent primarily on M_*, with a noticeable change in the distribution at $M_*>10^{10}M_\odot$, agreeing with the value found by Pan et al. (2015) using broadband color gradients and by Wang et al. (2018) using spectral indices. Galaxies above this mass show an increasing fraction of regions that are forming stars with increasing radius, whereas lower mass galaxies have a constant fraction of star forming regions with radius. Thus their findings support a picture of inside-out growth and quenching at high masses however, since they are not able to quantify the rates at which mass is being built by SF, they are not able to differentiate between I-O and O-I mechanisms for lower mass galaxies.This point was also made by Wang et al. (2018), who found no/weak radial gradients in tracers of recent SF in low mass galaxies and were unable to support either the I-O or O-I picture.

- In a different but related mechanism, Lin et al. (2019) studies the inside-out and outside-in quenching in MaNGA galaxies. They find that the fraction of galaxies showing inside-out quenching increases with halo mass, irrespective of stellar mass or galaxy type (satellites vs. centrals). In contrast, they report that the fraction of outside-in quenching galaxies do not depend on halo mass.

- Also, to consider other studies, using spatially resolved broad and narrow band/grism derived colours and measurements of the stellar mass and SFR densities, studies have found evidence for inside-out galaxy growth out to $z \sim 2$ in star-forming galaxies (Bezanson et al. 2009; Wuyts et al. 2012; Nelson et al. 2012, 2013; van de Sande et al. 2013; Patel et al. 2013; Tacchella et al. 2015; Nelson et al. 2016; Tacchella et al. 2016).

Hence, it looks clear from current as well as earlier observations that, the radial growth of galaxies is mass dependent. (Lin et al. 2019; Rowlands et al. 2018; Goddard et al. 2017; González Delgado et al. 2017; Ibarra-Medel et al. 2016; González Delgado et al. 2015; Sánchez-Blázquez et al. 2014; Pérez et al. 2013; Zhang et al. 2012; Gallart et al. 2008).

However there are also some curious observations like the one made by Wang et al. (2017). They found that some high mass spiral galaxies grow outside-in, and they have smaller sizes, higher stellar surface mass density, higher SFR and higher oxygen abundance than normal star-forming galaxies of a similar stellar mass.

So, while there is consensus in some aspects on where stellar mass growth occurs, there still remain disagreements in facets. In this thesis, an investigation of this dependence of radial growth on stellar mass is also carried out and can be read in detail in Section 4.2.1.

1.4 Scope and Structure of thesis

This thesis aims to take maximum advantage of IFS data from the **M**ulti-**U**nit **S**pectroscopic **E**xplorer (MUSE; detailed in Section 2.3). The data is suitable to perform a spatially resolved study of the stellar ages and to understand the spatial variation of the stellar ages over the galaxy. MUSE couples the discovery potential of a large imaging device to the measuring capabilities of a high-quality spectrograph, while taking advantage of the increased spatial resolution of $0''.2$/pixel. Its performance is supported by an expected spectacular gain achieved in spatial resolution without any loss in throughput and with almost full sky coverage. With its 400 megapixels per frame and 90000 spectra in one exposure, MUSE is the largest integral field spectrograph ever built, and the only one that allows to achieve a very high level on the spatially resolved studies of the stellar population and gas properties. Thus these observations from MUSE helps improve the status of research in this field by quantifying the stellar age-gradients and thus being able to differentiate between the inside-out and outside-in scenarios for 34 undisturbed galaxies from the GASP sample. The wide field-of-view of the observations from MUSE aid in observing until distant radial distances, to include the galaxy outskirts, thus helping to estimate thorough disk gradients of the galaxy. The potential of this data with regard to the extent of radial coverage is described in detail in Section 2.6. Further, this work also investigates the dependence of the stellar age gradients on galaxy's physical properties like M_* and morphology as discussed in Section 4.2.

Following is a brief outline of how the thesis is organised into different chapters:

1. **Chapter 1**: This chapter introduces the problem statement and defines the aims of this thesis. It explains how the study of spatial variation of stellar ages can tell where and how the galaxy builds its stellar mass, which can thus further elucidate galaxy evolution itself. It further talks about the various IFS surveys that have contributed to this study and discusses the current status of research in this field.

2. **Chapter 2**: This chapter introduces and explains the GASP program and it describes its main scientific drivers. It also establishes the galaxy sample of 34 GASP galaxies, observed with MUSE and analysed in this work.

3. **Chapter 3**: All the methods used to derive and analyse the main quantities, namely star formation rate, stellar mass, stellar age, stellar age gradients and star formation history are described in detail in this chapter.

4. **Chapter 4**: This chapter explains the observations for the 34 galaxies and discusses the results. The clear definition of inside-out and outside-in mechanism is laid out and the age gradient is compared with the star formation history of each galaxy. The chapter further explores the effects of the galaxy's physical properties like stellar mass and morphology (presence of bars, bulges) on age gradients. The origin of growth mechanism seen in each galaxy owing to an influence of these properties is analysed.

5. **Chapter 5**: The last chapter summarises the work and the results of this analysis. It further describes the future prospects that can be investigated using this analysis as a primary step.

"A galaxy is composed of gas and dust and stars - billions upon billions of stars. Every star may be a Sun to someone."

- Carl Sagan

2

The GASP Data

GASP (**GA**s **S**tripping **P**henomena in galaxies with MUSE) is an ESO Large Programme (Poggianti et al. 2017b) studying gas removal processes in galaxies with the **M**ulti-**U**nit **S**pectroscopic **E**xplorer (MUSE), which is an Integral Field spectrograph on the Very Large Telescope (VLT) at Cerro Paranal in Chile. GASP had been allocated 120 hours of observation with MUSE over four semesters, with which it has obtained deep MUSE data for 114 galaxies at redshift, z = 0.04–0.07, in varied environments (clusters, groups, and field), and with stellar mass range of $10^9 < M_* < 10^{11.5}$. The most important characteristic of the survey is its large coverage area. At GASP redshifts, the MUSE field of view covers 50–100 kpc, which makes it possible to study extraplanar gas and stars out to large distances from the galactic disk using only one or two MUSE pointings. This makes GASP the only existing IFU survey that can cover the main galaxy body, along with the outskirts and surroundings, and eventual tails out to $> 10R_e$ from the main galaxy body.

The main aim of this project is to significantly improve the understanding of effects that cause the galaxy to lose only its gas. The GASP targets are mainly galaxies showing optical signatures of unilateral debris or disturbed morphology due to gas-only removal processes. However, regular galaxies devoid of such signatures are also included to constitute a control-sample. The most convincing evidence for gas-only removal comes from observations of internally driven outflows and ram-pressure stripping. The most striking examples of galaxies with unilateral gas debris, are the so-called "jellyfish galaxies" that exhibit long tails/tentacles

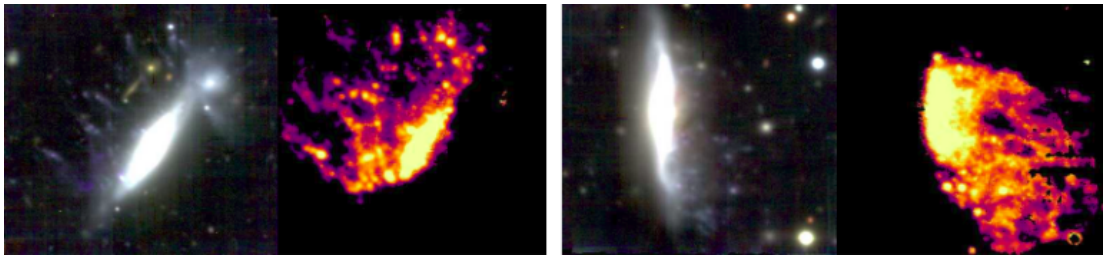

Figure 2.1: Example jellyfish galaxies from GASP sample. The first two images on left: RGB image of JO204 showing the stellar component of galaxy, Hα image of JO204 shoiwng the stripped gas. The right panel showing the respective two images for JW100 galaxy.

of material stripped from the galaxy body, making the galaxy look like a jellyfish (Ebeling et al. 2014, Fumagalli et al. 2014, Rawle et al. 2014). The GASP team defines *jellyfish galaxies* as those which have ionised tails as long as the diameter of the galaxy disk as seen in Hα, stripped due to ram pressure stripping.

Ram pressure stripping (RPS) is believed to be an efficient mechanism to remove gas from a galaxy, affecting only the interstellar gas and not the stars. When a galaxy moves through a hot, dense inter-cluster medium (ICM), the ICM exerts pressure on the gas of the galaxy and can remove it from the disk and halo. The expected ram pressure intensity exerted by the cluster can be estimated from the following expression (Gunn & Gott 1972):

$$P_{ram} = \rho_{ICM} \times \Delta v_{cl}^2 \tag{2.1}$$

where $\rho_{ICM}(r_{cl})$ is radial density profile of the ICM, r_{cl} is the clustercentric distance and Δv_{cl} is the velocity of the galaxy with respect to the cluster. Thus the efficiency of this mechanism depends on the density of the intergalactic medium and the relative galaxy velocity with respect to the cluster. Since the stellar component is undisturbed, it retains the memory of the galaxy history before stripping. Figure 2.1 shows examples of two jellyfish galaxies from the sample, JW100 and JO204.

This chapter presents the GASP program, the main scientific drivers of this program and the data reduction techniques involved. The chapter then establishes the sample of 34 galaxies used in this work and taken from the GASP sample.

2.1 Scientific Drivers

The key science questions that GASP is addressing are as following:

- What processes cause the removal of gas from the galaxy disk and from which part

of the galaxy and how is this gas removed? (Gullieuszik et al. 2017, Fritz et al. 2017, Moretti et al. 2018)

- How does the removal of gas affect the star formation activity of the galaxy? Does the gas stripping also affect the quenching? (Vulcani et al. 2018, George et al. 2018, Poggianti et al. 2019)
- How does the central black hole interact with the gas present in the galaxy? (Poggianti et al. 2017a, George et al. 2019, Radovich et al. 2019)
- How does the galaxy behave dynamically during its motion through the intra-cluster medium? (Bellhouse et al. 2017, Jaffé et al. 2018)
- What is the chemical evolution history of galaxies prior to and in absence of gas removal? (Franchetto et al. 2018)
- What is the spatially resolved star formation history and the stellar ages of galaxies prior to and in absence of the gas removal? This scientific driver forms the motivation for the work in this thesis.

2.2 GASP Data Sample

In order to cover the whole range of environments and ensure a good stellar mass distribution at low redshifts, GASP chose its targets based on three parent surveys as follows.

1. **WINGS** (Fasano et al., 2006) is a multiwavelength survey of 76 galaxy clusters at z = 0.04-0.7 covering both the northern and the southern hemisphere. The WINGS database is presented in Moretti et al. (2014) and is publicly available through the Virtual Observatory.
2. **OMEGAWINGS** (Gullieuszik et al., 2015) is an extension of the WINGS project that quadrupled the area covered in each cluster (1 deg^2). For 46 galaxy clusters from WINGS, B- and V- band deep imaging was obtained with OmegaCAM at VLT Survey Telescope (VST).
3. **PM2GC** The Padova Millenium Galaxy and Group Catalog (PM2GC; Calvi et al. 2011) was used for a comparison sample consisting of field and group galaxies within the same stellar mass and redshift range as that of WINGS.

The primary targets of GASP were taken from the atlas of Poggianti et al. (2016). The atlas consists of a large sample of galaxies which show disturbed morphologies and are suggestive of gas-only removal mechanisms as seen in optical bands. The B-band images from WINGS,

OMEGAWINGS and PM2GC were visually inspected for galaxies with (a) debris or tails on one side of the galaxy, (b) disturbed morphologies suggestive of unilateral external forces, (c) a distribution of star forming regions on one side of galaxy suggesting triggered SF on that side. Since GASP aims to study the gas-only removal processes, mainly ram-pressure stripping, it consciously avoided the selection of targets that showed irregularities due to tidal interactions or mergers.

GASP finally observed **114 targets** in service mode. Of these targets, 94 were seen to be disturbed in optical and hence selected as ram pressure stripped candidates and 20 other undisturbed galaxies were observed to constitute a control sample.

- **Ram Pressure Stripping candidates**: The primary targets of the GASP survey are the **94 galaxies** identified as ram-pressure stripping candidates. Of these, 64 galaxies belong to a cluster and 30 are field galaxies.
- **Control Sample**: This sample has 12 galaxies in clusters and 8 field galaxies. This sample of **20 galaxies** was selected to observe galaxies with no optical sign of stripping, i.e, no disturbed morphologies.

The integral field spectroscopy obtained by GASP has been an optimal method to identify the physical processes at work because it probes both gas and stars and can discriminate processes affecting only the gas, such as ram pressure, from those affecting both gas and stars, such as tidal effects and mergers.

2.3 MUSE Spectrograph

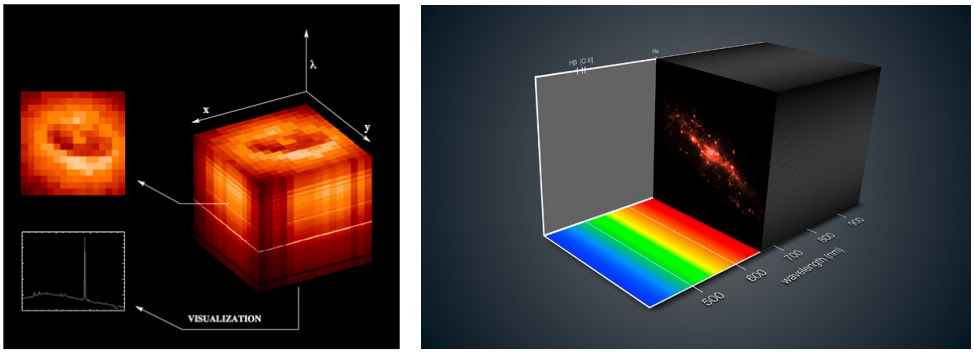

Figure 2.2: Schematic representation of a MUSE datacube showing the spatial axes along x and y axis and the spectral axis along the third z-axis, thus producing a 3D spectroscopy datacube.

All GASP observations were carried out in service mode with the MUSE spectrograph (Bacon et al. 2010), mounted at the Nasmyth focus of UT4 VLT, at Cerro Paranl in Chile.

The constraints demanded for the observations were clear conditions, moon illumination < 30%, moon distance > 30°, and <1″ seeing at zenith. This spatial resolution of 1″ corresponds to about 1 kpc at GASP redshifts. Since MUSE is such an integral part of GASP, a brief description of the essential features of MUSE and the understanding of the MUSE datacube are highlighted in this section.

MUSE is composed of 24 IFU models and each of them is equipped with a 4k × 4k CCD. The spectral range of MUSE is between 4500 and 9300 Å, and data is sampled at 1.25 Å/pixel, with a spectral resolution of 2.6 Å. Thus each datacube of MUSE has $\sim 10^5$ spectra. The resolving power at 7000Å is R=2700, corresponding to 110kms^{-1} or 53 kms^{-1}pixel^{-1}. The GASP data were observed using the wide field mode of MUSE and thus has a 1′×1′ field of view and with natural seeing (without the adaptive optics aid) it produced data sampled at 0.″2/pixel.

Figure 2.2, shows the schematic representation of a MUSE datacube. Each spaxel, or spatial pixel, contains spectral information of the galaxy and together makes up for the 3D datacube of MUSE. As can be seen from the figure, each layer of the datacube represents the image of the observed galaxy at every wavelength in the spectral range of 4500 to 9300 Å making upto 10^4-10^5 spectra in every datacube.

2.4 Data Reduction

For the analysis of all the GASP galaxies, the standard concordance cosmology was adopted with H_0=70 kms^{-1} Mpc^{-1}, Ω_M=0.3, and Ω_λ=0.7 and a Chabrier (2003) Initial Mass Function (IMF).

The standard GASP procedure for data reduction is described in detail in Poggianti et al. (2017b). In this section, we briefly outline the main steps used in the data reduction for the entire galaxy sample. We dedicate a separate section to explain the reduction done by SINOPSIS in Section 2.4.1, owing to the significance of this step for producing the data that is paramount for this thesis.

All the data was reduced with the most recent version of the MUSE pipeline at the time of data production. Along with the targets, at least one spectrophotometric standard star was also observed each night for flux and telluric correction purposes. The data and the standard star frames were thus flat-fielded, wavelength-calibrated and corrected for differential atmospheric refraction using the telluric lines from standard star. Due to the wide field of view of MUSE, the observations have >50% area for sky measurements and hence the sky

was modeled directly from the individual frames using the 20% pixels that had the lowest counts.

Next, the final flux-calibrated data cube was generated by lining up the individual frames using sources in the white-light images to calculate the offsets. This reduced cube is then first corrected for extinction due to our own Galaxy, using the extinction value pertaining to the RA and Dec of the observed galaxy from the catalogue of Schlafly & Finkbeiner (2011), and using the extinction law from Cardelli et al. (1989). The extinction correction then produces the second reduced datacube. From here, the procedure can be divided to analyse different components, namely,

- Analysing the gas kinematics using KUBEVIZ
- Analysing the stellar kinematics using pPXF
- Using the gaseous and stellar redshifts from KUBEVIZ and pPXF respectively as inputs to the spectral synthesis code, SINOPSIS

The main emission lines in the spectrum of galaxies were extracted using the publicly available IDL software KUBEVIZ (Fossati et al. 2016). Starting from an initial redshift, KUBEVIZ uses the MPFit (Markwardt 2009) package to fit gaussian line profiles, yielding gaseous velocities (with respect to given redshift), velocity dispersions and total line fluxes. Then, as recommended by Fossati et al. (2016), the errors on the line fluxes are scaled to achieve a reduced χ^2 =1.

Next, to extract the stellar kinematics from the spectrum, the Penalized Pixel-Fitting (pPXF; Cappellari & Emsellem 2004) code was used along with the stellar population templates by Vazdekis et al. (2010). Single stellar populations (SSP) of six different metallicities ([M/H]=-1.71 to 0.22) and 26 ages (1 to 17.78Gyr) calculated with the Girardi et al. (2000) isochrones. After this step, the maps of stellar rotational velocity and stellar velocity dispersion were obtained. This allows us to derive a redshift estimate that is then used as an input for the stellar population analysis with SINOPSIS which is described in detail in Section 2.4.1.

SINOPSIS produces a best-fit model cube (stellar plus gaseous emission) and stellar-only model cube. The latter is subtracted from the former to produce an emission-only datacube. KUBEVIZ is run again on this datacube and the emission-line, absorption-subtracted fluxes measured are corrected for extintion due to the dust internal to the galaxy under observation. The correction is derived from the Balmer decrement using an intrinsic Hα/Hβ ratio as 2.86 and adopting the Cardelli et al. (1989) extinction law. These values are then used for further analysis.

2.4.1 SINOPSIS

The stellar population analysis was done using the spectrophotometric fitting code, SINOPSIS (**SI**mulati**N**g **OP**tical Spectra w**I**th **S**tellar population models; Fritz et al. 2007, 2011, 2017) for deriving the spatially resolved stellar population properties. This code works by searching the combination of single stellar population (SSPs) spectra that best fit the equivalent widths of the main lines in absorption and in emission and the continuum at various wavelengths, minimizing the χ^2 using an Adaptive Simulated Annealing algorithm. The star formation history is let free with no analytic priors.

The GASP version of SINOPSIS has been described in full detail in Fritz et al. (2017). The code was improved to include the latest SSP model from S. Charlot and G.Bruzual (in preparation) with a higher spectral and age resolution. The latest version of PADOVA evolutionary tracks (PARSEC) by Bressan et al. (2012) and metallicity values covering the range Z=0.0001 to 0.04 have been used. In addition, nebular emission was added for the youngest (i.e.age < 2×10^7 yr) SSP, by ingesting the original models into CLOUDY (Ferland et al. 2013).

SINOPSIS requires the spectrum redshift as input, thus the redshift at each location of the datacube was taken from pPXF (stellar) and KUBEVIZ (gaseous). To avoid errors due to the possible decoupled nature of gas and stars, thus having different redshifts, another option was added to SINOPSIS. It allowed the use of the gas redshift, when available, to detect and measure the equivalent width of emission lines, while the stellar redshift was used to fit the continuum and to measure absorption lines.

Finally, SINOPSIS gives spatially resolved estimates of the stellar population properties, and maps are produced for:

- Stellar masses
- Luminosity-weighted and Mass-weighted stellar ages
- Average star formation rate in 4 age bins:

  1. Young (ongoing SF) : t $\leq 2\times10^7$ yr;
  2. Recent : 2×10^7 < t $\leq 5.7\times10^8$ yr;
  3. Intermediate : 5.7×10^8 < t $\leq 5.7\times10^9$ yr;
  4. Old : t > 5.7×10^9 yr

The choice and number of age bins were based on the integrated spectra of WINGS Survey. However, it is extremely difficult to disentangle the contribution to the integrated light of stellar populations in the 7-14 Gyr range. Further, effects like age-metallicity degeneracy and dust extinction, make the spectra in this age range very similar. This issue was dealt with by using a free-free approach and not assigning an analytic form (like log-normal, a double exponential) to the star formation history. It should be mentioned that, SINOPSIS is fitting only half of the entire MUSE spectrum, as the red part is heavily contaminated by telluric lines (detailed in Poggianti et al. 2017b).

Treatment of Dust Extinction: Since light emitted by the youngest population is the most affected by the presence of dust, the code simulates a selective extinction effect (Calzetti et al. 1994). Once a stellar population ages, it progressively gets rid of this interstellar medium envelope (and hence the dust), either by means of supernova explosions, which will blow it away or because of the proper motions of the star clusters in the galaxy. Since dust is found in the ISM and is also well mixed with the stars, a proper treatment would account for a 3D dust geometry. However, SINOPSIS includes the effect of dust extinction by modeling it as a uniform dust layer in front of the source. This approach also reproduces the effects of dust at large scales satisfactorily, as shown by Liu et al. (2013).

2.5 Data Sample analysed in this thesis

The study sample for this thesis, has been sourced from the GASP galaxy sample. On surveying the entire GASP sample, 34 undisturbed galaxies were identified for the study in this thesis. Some of these galaxies were the ones that were originally part of the sample of RPS-candidates. Hence, the target sample includes galaxies from both the control sample (20 galaxies) and the RPS-candidates (14 galaxies). However, the galaxies taken from the sample of RPS-candidates were the ones that were seen to be fairly regular in optical as well as the Hα emission and were hence perceived to be morphologically undisturbed. An in-depth analysis of the gas in these 14 jellyfish galaxies didn't show signs of stripping or disturbed morphology. Further, these galaxies neither show a lopsided morphology nor unilateral gas stripping and thus, all are fairly regular.

A fundamental requirement while making the target sample was to only consider galaxies with presence of gas and hence all the galaxies of this sample are emission line galaxies and further neither of them hosts an AGN. While most of the galaxies are spiral galaxies (Sb-Sd),

the sample comprises of varying morphological differences on the basis of presence of bar and/or bulge. In addition, there are also a few lenticulars and early spirals for comparison. The morphological classification is taken from the WINGS/OmegaWINGS catalogue and it is based on an automatic classification tool, MORPHOT (Calvi et al. 2012; Fasano et al. 2012). The target galaxies span a wide range in stellar mass, $9 < M_{\odot} < 11.5$, and of environments with 17 galaxies belonging to a cluster and 17 being field galaxies.

It should be noted that the GASP scientific driver forming the basis of this thesis is to understand the spatially resolved SFH of galaxies prior to and in absence of the gas removal. This thesis hence undertakes the primary step to comprehend the star formation histories for regular galaxies prior to any gas removal. The next step will be to extend this work to the primary GASP sample consisting of the jellyfish candidates. Tables 2.1 and 2.2, summarise the properties of the cluster and field galaxies respectively used for this study.

Table 2.1: Table summarising the RA, Declination, membership, redshift and the stellar mass of the 17 **cluster galaxies** studied in this work.

Cluster Galaxies					
Galaxy	R.A. (J2000)	Declination (J2000)	Membership	Redshift* (z)	M_* ($10^{10} M_{\odot}$)
A3128_B_0148	03:27:31.09	-52:59:07.655	A3128	0.0603	0.7±0.2
A3266_B_0257	04:27:52.58	-60:54:11.565	A3266	0.0596	0.8±0.2
A3376_B_0261	06:00:13.68	-39:34:49.232	A3376	0.0463	3.4±0.6
A970_B_0338	10:19:01.65	-10:10:36.924	A970	0.0588	1.2±0.2
JO5	10:41:20.38	-08:53:45.559	A1069	0.0651	1.9±0.4
JO17	01:08:35.33	+01:56:37.043	A147	0.0447	1.4±0.3
JO41	12:53:54.79	-15:47:20.096	A1631a	0.0465	1.6±0.3
JO45	01:13:16.58	+00:12:05.839	A168	0.0453	0.15±0.04
JO68	21:56:22.00	-07:54:28.971	A2399	0.0577	1.0±0.2
JO73	22:04:25.99	-05:14:47.041	A2415	0.0578	1.1±0.3
JO102	03:29:04.69	-52:50:05.364	A3128	0.0603	1.0±0.2
JO128	12:54:56.84	-29:50:11.184	A3530	0.0548	0.8±0.2
JO138	12:56:58.51	-30:06:06.284	A3532	0.0555	0.4±0.1
JO159	13:26:35.70	-30:59:36.920	A3558	0.0486	0.7±0.2
JO180	21:45:15.00	-44:00:31.188	A3809	0.0626	1.0±0.2
JO197	09:06:32.58	-09:31:27.282	A754	0.0545	1.1±0.3
JO205	21:13:46.12	+02:14:20.355	IIZW108	0.0486	0.33±0.08

*The $z_{cluster}$ are used here so our results are not biased due to peculiar motions of galaxies in clusters.

†Since these are field galaxies, they don't have strong peculiar motions and hence the redshift of the galaxy itself is used.

Table 2.2: Table summarising the RA, Declination, membership, redshift and the stellar mass of the 17 **field galaxies** studied in this work.

Field Galaxies				
Galaxy	R.A. (J2000)	Declination (J2000)	Redshift† (z)	M_* ($10^{10} M_\odot$)
P648	10:01:27.74	+00:09:18.372	0.0660	2.8±0.6
P669	10:02:00.62	+00:10:44.299	0.0458	3.2±0.6
P954	10:02:03.33	-00:12:49.836	0.0451	0.4±0.1
P5215	10:16:58.24	-00:14:52.876	0.0629	3.35
P13384	10:53:03.15	-00:13:30.932	0.0512	0.7±0.2
P14672	11:01:55.10	+00:11:41.095	0.0498	0.8±0.1
P15703	11:06:33.28	+00:16:48.192	0.0423	10.0±2.0
P17945	11:15:26.45	+00:16:11.586	0.0439	0.6±0.1
P19482	11:22:31.25	-00:01:01.601	0.0406	2.2±0.4
P20769	11:27:17.60	+00:11:24.388	0.0489	0.3±0.1
P20883	11:27:45.41	-00:07:16.580	0.0614	0.8±0.2
P21734	11:31:07.90	-00:08:07.914	0.0686	6.0±1.0
P25500	11:51:36.28	+00:00:01.929	0.0604	7.0±1.0
P42932	13:10:44.71	+00:01:55.540	0.0410	3.3±0.6
P45479	13:23:34.73	-00:07:51.673	0.0515	3.7±0.6
P48157	13:36:01.59	+00:15:44.696	0.0615	3.9±0.8
P57486	14:11:34.45	+00:09:58.293	0.0529	0.9±0.2

2.6 The MUSE Perk

As described in Section 2.3, MUSE offers remarkably high quality data with a fine spatial resolution of about 1″ along with a good sensitivity and excellent field of view (1′×1′). At redshifts of the GASP targets, this spatial resolution translates to as 1″ ∼ 1 kpc. Hence the high spatial resolution of IFU data facilitates in studying the galaxy outskirts out to tails of 50-100 Kpc (∼10R_e). A detailed analysis of the spatial variation of galaxy properties over the entire galaxy body can help give fundamental insights in galaxy evolution.

Table 2.3 provides a quantitative comparison of the radial coverage ranges from 7 previous studies carried out to study the radial gradients of galaxy properties in disk galaxies. Even though there are a lot more studies done for early type (ET) galaxies, we limit this comparison only to the late types (LT) since our sample is comprised of mostly the disk galaxies. The list combines a large variety of different observational approaches, sample sizes and radial coverage. The majority are based on IFU observations and some on long-slit spectroscopy. The radial coverage of these studies varies between 1 - 2 R_e.

In comparison to this, we observe the radial coverage of the galaxies in our work. In the

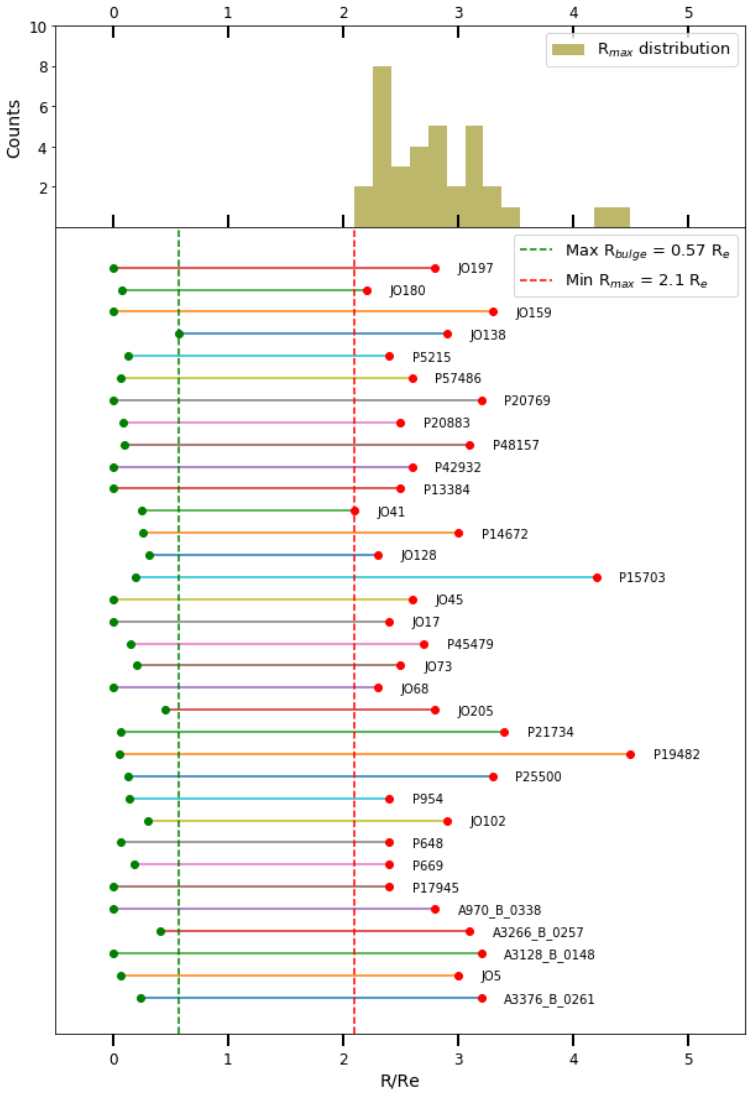

Figure 2.3: The radial ranges for all the 34 galaxies of this sample are shown here. The minimum radius starts after the bulge radii (R$_{bulge}$) and the maximum radius is defined as per a method to get the R$_{max}$. The green and red vertical lines trace the maximum R$_{bulge}$ and the minimum R$_{max}$ respectively. The two lines thus mark the common radial range for all the galaxies. In the upper panel, the distribution of the galaxies is shown for the different radial coverage extents (R$_{max}$).

Figure 2.3, the radial range of all the 34 galaxies of our sample can be seen. The radial ranges shown in the figure are not of the raw data that we get from MUSE. These ranges are after some analytic cuts performed for each galaxy to use only the range with the most reliable results. The methods for these cuts are described better in the next chapter, Chapter 3. Since the analysis is focused on the disk-dominated region, we focus in the radial range between R$_{bulge}$ and R$_{max}$. The R$_{max}$ refers to the farthest radial distance, identified uniquely for each galaxy, where the signal-to-noise ratio is sufficient to measure the properties of the stellar

population gradients. The method to estimate R_{max} will be further explained in Section 3.7.1. Some of the galaxies have a bulge and the contribution of the bulge has been subtracted from these ranges. Thus after R_{bulge}, we have the region of the galaxy disk which dominates the galaxy surface brightness by more than 90%. While some of the galaxies in this work have a radial coverage upto $5R_e$, even the minimum of the radial range shown by a galaxy is at $2.2R_e$ which is also greater than most of the studies done in the past as highlighted in Table 2.3. The common radial range for all galaxies is also shown in the figure and it ranges from 0.57 R_e - 2.2 R_e. In the top panel of the figure, a histogram is also shown to summarise the distribution of the galaxies for different maximum radial coverage extents (R_{max}).

Table 2.3: Table providing the results of 7 previous literature studies on stellar population gradients taken from Goddard et al. (2017).

Author	Galaxy Type	Sample Size	Observation method	Radial range[‡]
Goddard et al. (2017)	LT	216	IFU	$1.5R_e$
Zheng et al. (2017)	LT	422	IFU	$0.5 - 1.5R_e$
González Delgado et al. (2015)	LT	227	IFU	1HLR
Morelli et al. (2015)	LT	10	Long-slit	$r_{d95} - r_{Last}$
Sánchez-Blázquez et al. (2014)	LT	62	IFU	$1.5R_e - r_{Disc}$
Morelli et al. (2012)	LT	8	Long-slit	$1.5R_e$
Jablonka et al. (2007)	LT	32	Long-slit	$< 2R_e$

Finally, we present the RGB images of all the 34 galaxies in our sample in Figure 2.4 and Figure 2.5.

[‡]Radial range nomenclature:

- In González Delgado et al. (2015), HLR is the half-light radius.
- In Morelli et al. (2015), the analysis is focused on the disc-dominated region between r_{d95}, which is the radius where the disc contributes more than 95% of the galaxy surface brightness, and r_{Last}, which is the farthest radius where the signal-to-noise ratio is sufficient to measure the properties of the stellar populations.
- In Sánchez-Blázquez et al. (2014), r_{Disc} corresponds to the radius at which the light starts being dominated by the disc.

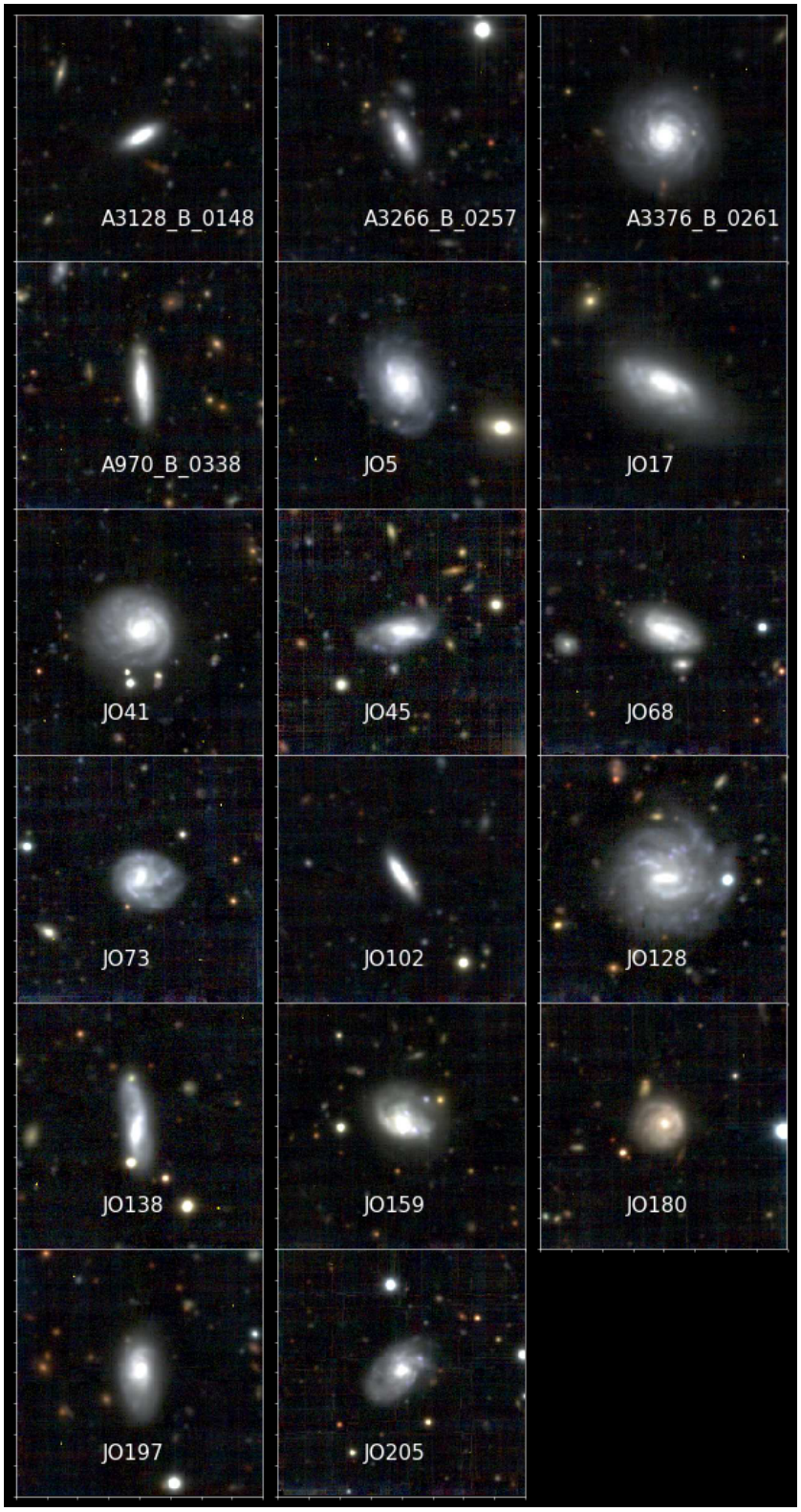

Figure 2.4: The galaxy data sample forming the cluster sub sample for this thesis. The names of each of the galaxy are written within the galaxy sub-pane.

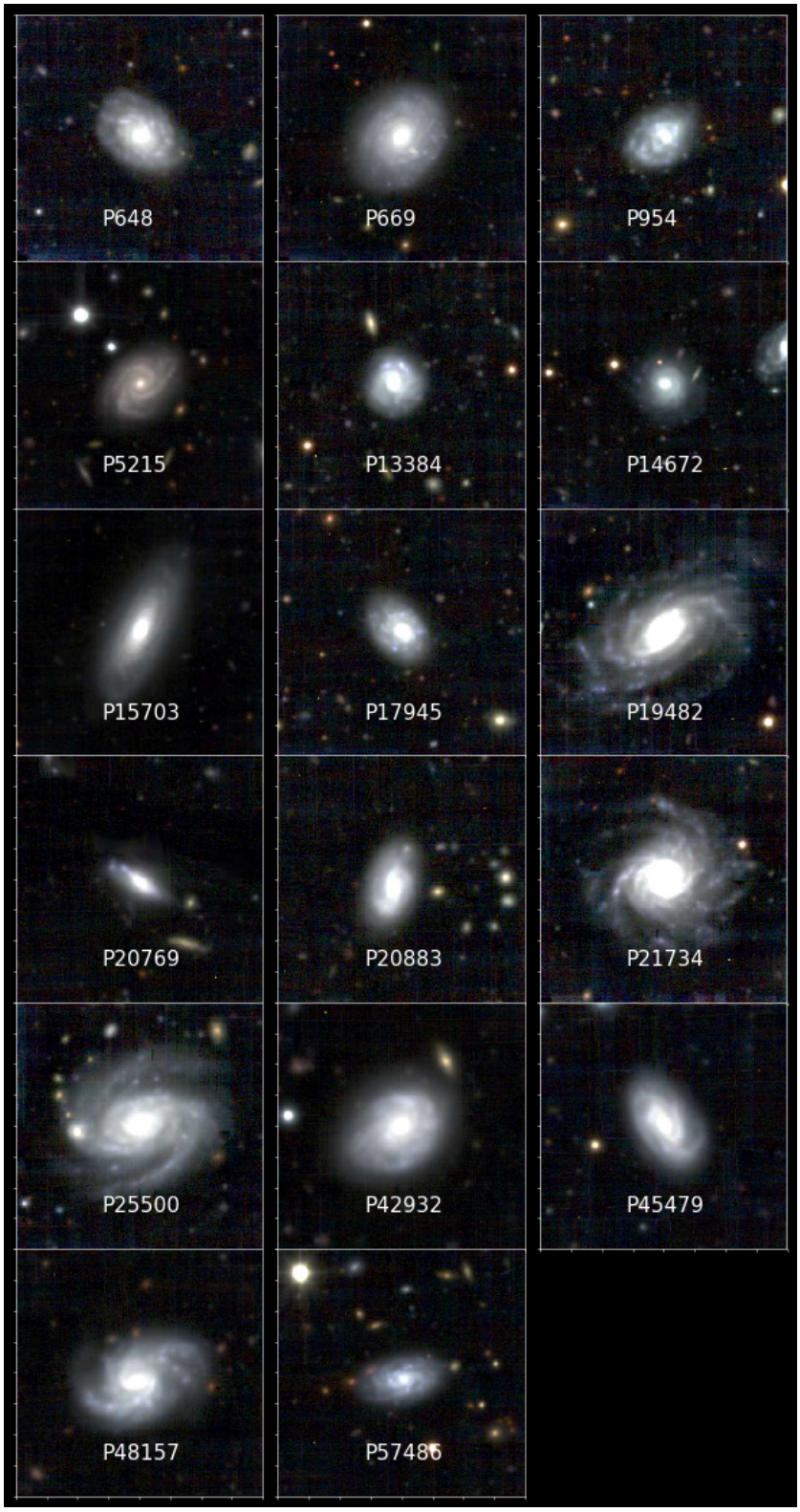

Figure 2.5: The galaxy data sample forming the field sub sample for this thesis. The names of each of the galaxy are written within the galaxy sub-pane.

"Equipped with his five senses, man explores the universe around him and calls the adventure Science."

- Edwin Hubble

3 Methods

In this chapter, we dive into the details of the methods used to analyse the data sample. As outlined in Chapter 2, the data was reduced using GASP's standard reduction procedure, at the end of which stellar population properties of age, metallicity and star formation rates in different age bins were obtained.

This chapter is organised into following sections: it begins with the description of the coordinate transformations adapted in section 3.1; followed by which in section 3.2, the cleaning measures taken to obtain reliable data for analysis are reported; in section 3.3, the SFR maps are presented and discussed; in section 3.4 the procedure to estimate the structural parameters of the galaxies using a photometric analysis are explained; in section 3.5, the deprojected distance calculations are described; in section 3.7, the spatial binning methods and the related parameters are detailed and finally in sections 3.6, 3.9 and 3.10 the methods incorporated to infer stellar ages, stellar age gradients and star formation histories are outlined respectively.

The galaxy **A3376_B_0261** is used as an example to describe the methods used in the data analysis. All the procedures described in this chapter are then applied to all target galaxies; the results are presented and discussed in the following chapter. This galaxy is a fairly regular and face-on spiral galaxy. Hence, it serves as an immaculate choice to be the representative of the entire study sample of this thesis. The figures and plots for all the other galaxies can be found in the Appendix A.1.

3.1 Coordinate Transformations

The raw frames obtained from SINOPSIS had dimensions of about $\sim 320 \times 320$ pixels. Since the observations were taken with MUSE in the wide field mode, each frame had a field of view of about $1' \times 1'$. This gives a pixel size of about $0''.2$, which translates as area in every pixel to $0''.2 \times 0''.2$. Hence, in order to have values appropriate for analysis, these frames were first transformed from per pixel values to units of arcsec^2 and then to units of kpc^2. To describe these transformations, some basic terms are briefly elucidated below:

• **Cosmological Redshift**: For all purposes in this thesis, we are using the cosmological redshift (z) only. Cosmological redshift is a result of the stretching of photons emitted from distant galaxies and quasars due to the expansion of space itself and not due to the motion of the celestial body, as shown in Figure 3.1. For GASP redshifts (relatively nearby), the z can be estimated from the spectra of each galaxy using the following equation,

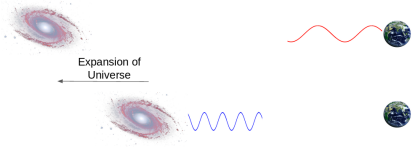

Figure 3.1: An illustration of the cosmological redshift.

$$z = \frac{\lambda_{obs} - \lambda_{rest}}{\lambda_{rest}} \tag{3.1}$$

where z is cosmological redshift, λ_{obs} is the observed wavelength at Earth and λ_{rest} is the emitted/absorbed wavelength by the distant galaxy. Hence, in case of cluster galaxies, we have used only the redshift of the cluster ($z_{cluster}$), while for the field galaxies we use the redshift of the galaxy itself (z_{galaxy}).

• **Angular Distances**: As illustrated in Figure 3.2, when observed from Earth, a celestial body of size d, at redshift z, will subtend an angular size of dθ at the observer, ie., the body has the angular size of dθ. The angular diameter distance (D_A) of this body from the observer on Earth can be estimated as,

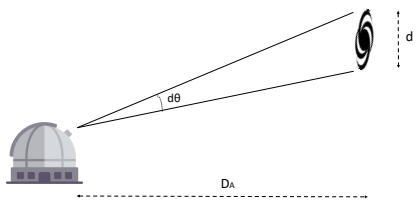

Figure 3.2: An illustration to explain angular distances.

$$d\theta = \frac{d}{D_A} \tag{3.2}$$

and if dθ is in arcseconds,

$$d\theta('') = 206265 \times \frac{d}{D_A} \tag{3.3}$$

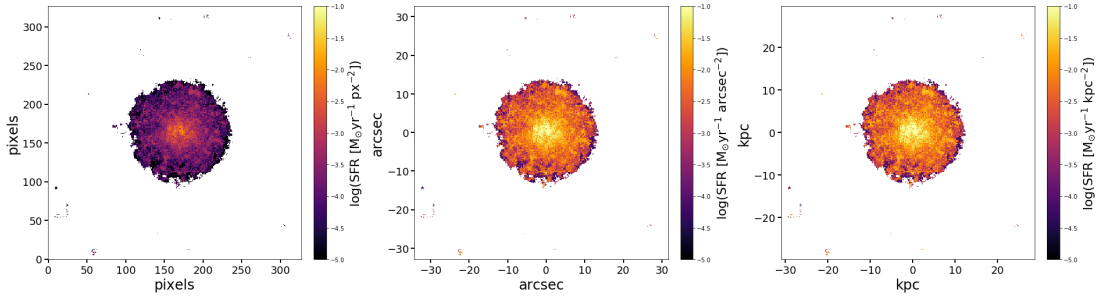

Figure 3.3: SFR maps of galaxy A3376_B_0261 in units of per px^2, per arcsec^2 and per kpc^2. The SFR maps in arcsec and kpc can seen to be centred at the galaxy. The color bar shows the log SFR density in the respective units. The range of the color bar is same in all the cases to present a comparison.

Using the above two definitions and the ASTROPY.COSMOLOGY package of python, the number of transverse proper kpc in every arcsec at the redshifts of each of the galaxy was estimated. For computing angular distances, the cosmological redshifts are used to circumvent the variations arising due to the peculiar motion of the galaxies in cluster. Hence for the case of galaxy A3376_B_0261, the $z_{cluster}$=0.0463 is used, as is also listed in the Table 2.1. Specifically for the case of A3376_B_0261, every arcsecond corresponds to a value of about 0.91 kpc and for the galaxies of this sample in general, $1'' \sim 1$ kpc. Using this, the values in the frames were converted from per arcsec^2 to per kpc^2.

Further, in order to work in the galacto-centric frame from here on, the origin was shifted to the centre of the galaxy for all the galaxy frames. Figure 3.3, shows the Star Formation Rate (SFR) map of the case study galaxy A3376_B_0261 with values in units of pixels, arcsec and kpc, respectively. The SFR maps in arcsec and kpc units are in a galacto-centric frames. For analysis from here on, the galacto-centric frames in units of kpc are used.

3.2 Cleaning the data

First and foremost, in order to ensure that the analysis was based upon the most reliable pixels of the galaxies only, some cleaning measures were adopted.

3.2.1 Signal to Noise Ratio

Since there were some low signal pixels, it was decided to sever these pixels based on the signal to noise ratio (SNR) values for each galaxy. The average signal-to-noise ratio of flux over the entire spectrum was obtained for each pixel from SINOPSIS.

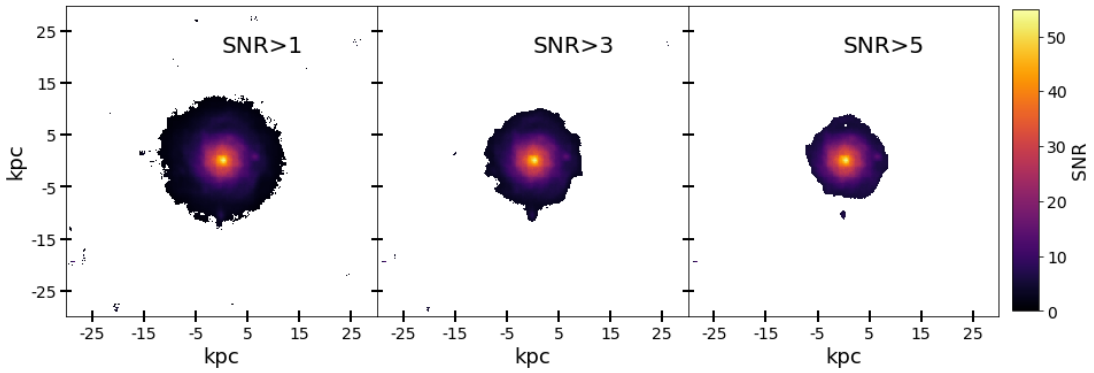

Figure 3.4: The different SNR levels, SNR>1,SNR>3,SNR>5 respectively, for galaxy A3376_B_0261.

Figure 3.4 demonstrates the three signal-to-noise ratio maps with cut levels as SNR >1, SNR >3, SNR >5 for galaxy A3376_B_0261. The central regions of the galaxy have very high SNR, well above 50, as also rooted by the colorbar next to the figure. It is evident from the figure that the SNR >5 and SNR >3 cuts are filtering the galaxy pixels a bit too strongly in the outer radii of the galaxy. Since we want to ensure we are also able to study the distant galaxy disks for each of the galaxy, we adapt the SNR >1 cut for our analysis as it ensures to filter most of the bad pixels. Further, the choice of this S/N level is justified as this cut is on values for each pixel while for this study, values averaged over galaxy regions comprising of a few pixels are used.

3.2.2 Flux Contribution

SINOPSIS provides the output of flux contribution, i.e., how much does the population in each pixel contribute to the stellar continuum in the respective age bin. Small amount of light attributed to old stellar populations can contribute significantly to the total mass budget, since the old stellar populations have a much larger mass-to-light ratio than young ones. As a consequence, small inaccuracies in the fitting (in terms of flux) can produce spurious detections of old stellar populations inducing large errors in the computed mass. Therefore, all spaxels for which the contribution of the two oldest age bins to the total light is lower than 5% were excluded. Figure 3.5 illustrates the SFR maps of galaxy A3376_B_0261, before (upper panel) and after (lower panel) the flux contribution correction in the third and the fourth (the two old) age bins.

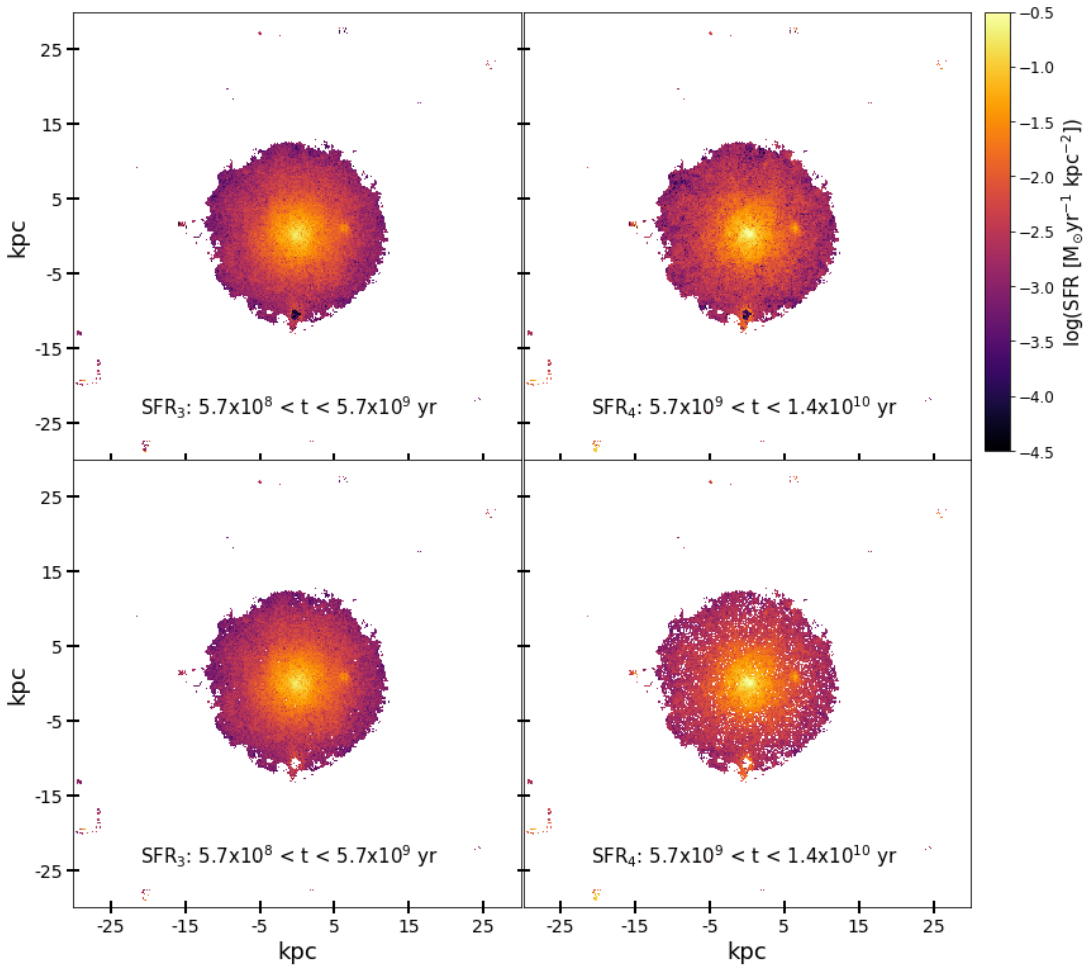

Figure 3.5: Filtering the pixels contributing less than 5% to the flux continuum in the third (left panel) and the fourth (right panel) age bins for galaxy A3376_B_0261. The upper panel shows the galaxy SFR map before the filtering and the lower panel shows after the filtering.

3.2.3 Cleaning Masks to filter foreground and background sources

Figure 3.6 illustrates the RGB composite image of galaxy A3376_B_0261. As highlighted by the red markings, there are two background galaxies to the south and the west of this galaxy. Their presence can be clearly ascertained from the SFR maps, as their intensity becomes stronger for the older age bins. This helps us see that this is not an increased emission from the galaxy but actually a background galaxy disturbing our analysis. Further, the spectra of all the sources in the MUSE datacubes were also checked to confirm they are background galaxies. Hence, to filter all such foreground and background sources, cleaning maps for all the galaxies were made.

Figure 3.7 presents the SFR maps of the galaxy A3376_B_0261 in the four different age

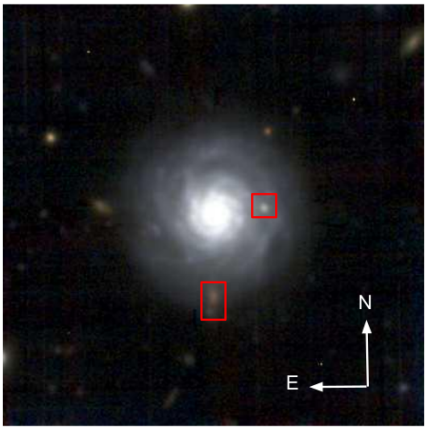

Figure 3.6: An image of galaxy A3376_B_0261 in RGB with the background galaxies within the galaxy's area highlighted.

bins, after all the cleaning processes are applied. It should be noted that from here on, only the pixels that remain after these cleaning steps, are used for the further analysis.

3.3 Star Formation Rate

Figure 3.7 shows the spatially resolved star formation surface density in four age bins, as labelled in the figure. The observations from it can be summarised as follows:

- As seen from **Age bin 1: t < 2×10^7**, the top-left panel of the figure, the most intense star formation is seen within the central regions of the disk with values of the order $\sim 10^{-1} M_{\odot} yr^{-1} kpc^{-2}$. While outside this region, SF can be seen to decrease more rapidly to lower values.
- **Age bin 2: 2×10^7 < t < 5.7×10^8**, is the intermediate-age range as shown by the upper-right panel of the figure. It shows mostly similar SFR values for most of the galaxy body with some pixels showing only slightly higher SFR.
- **Age bin 3: 5.7×10^8 < t < 5.7×10^9** and **Age bin 4: 5.7×10^9 < t < 1.4×10^{10}**, are the two older age bins represented by the two lower panels. The older populations seem to be concentrated only in the very centre thus being dominant in what we expect to be the bulge of the galaxy.

3.4 Photometric Analysis

In order to derive the radial gradients of the galaxies, structural parameters were obtained through photometric analysis. To obtain the mean position angle, ellipticity, and effective radius of the galaxy disk, a simple surface brightness analysis was undertaken for only three

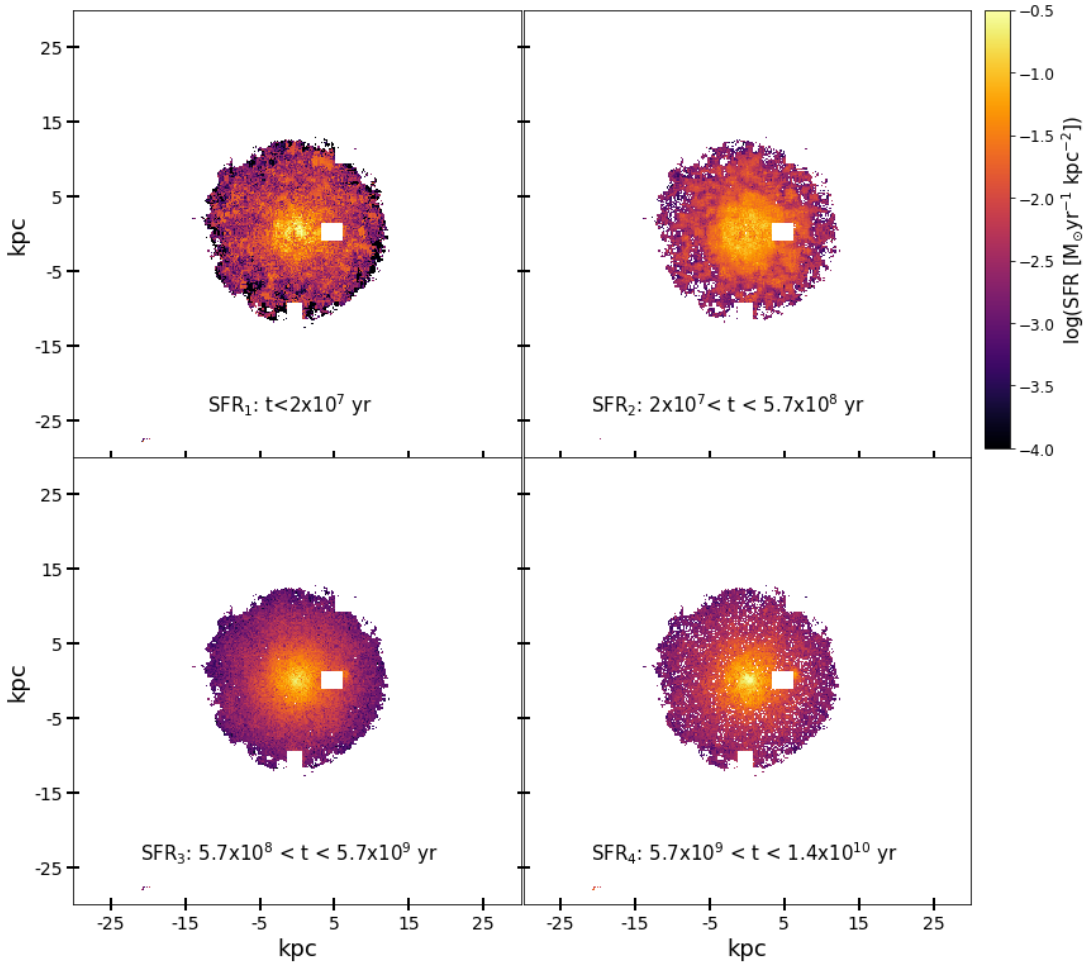

Figure 3.7: The cleaned and filtered SFR maps of four different age bins, for galaxy A3376_B_0261.

galaxies of the sample, namely, A3376_B_0261, JO17 and P25500. The structural parameters for the rest of the galaxies were taken from Franchetto et al. (2018). The effective radius of a galaxy, R_e is the radius that encloses half of the total galaxy luminosity. The estimation of this parameter is essential since it is then used to scale the galacto-centric distances.

For the extraction of the surface brightness profile of each galaxy, an isophotal analysis was done using the g-band images of the galaxies. These images in g-band were obtained by integrating the MUSE datacube over the g-band of the SDSS. The galaxy isophotes (contours of constant surface brightness) were fitted using the ELLIPSE package of IRAF (Jedrzejewski 1987). This package uses a guess intermediate isophote defined by initial parameters, and then proceeding from it, elliptically segments the galaxy based on different levels of surface

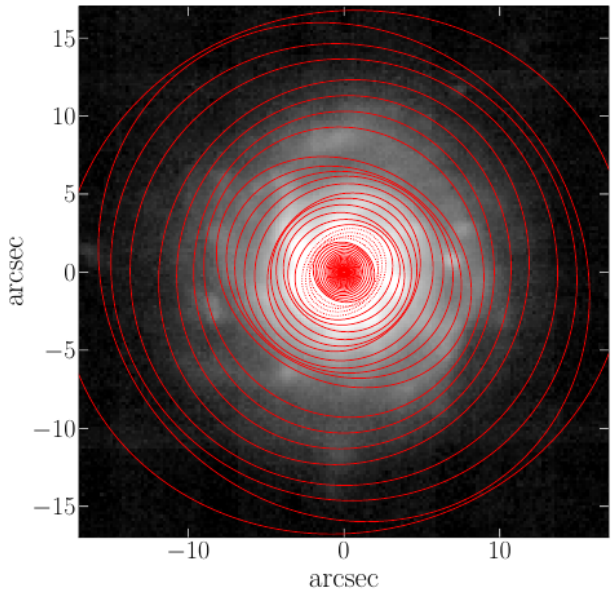

Figure 3.8: Elliptical segmentation of surface brightness performed by ellipse on the g-band image of control-galaxy A3376_B_0261. The dotted ellipses indicate the invalid isophotes (Franchetto et al. 2018).

brightness as shown in Figure 3.8 for galaxy A3376_B_0261. The set of initial parameters includes the values of central coordinates (x_c, y_c) in the image, semi-major axis length (a) in pixel units, ellipticity (e) and position angle (PA) measured anti-clockwise from the North direction. During the fitting procedure, the central coordinates are re-measured each time, and the center of each fitted isophote is kept fixed. Both the position angle and ellipticity of each ellipse are unconstrained and the final best fit value is chosen.

For this part of the analysis, different cleaning maps were used. These cleaning maps also masked the spiral arms along with the foreground and background sources. This was done since we are interested in the structural properties of the underlying disk. IRAF fits a series of isophotes through the galaxy and outputs a table with the structural parameters for each isophote, namely, the semi-major axis length, the area, the luminosity intensity integrated into the area, the ellipticity and the position angle.

In order to derive the effective radius, mean ellipticity and mean PA, a multi-component fitting was done to account for the different contributions to the surface brightness profile as follows:

- The disk and the bulge are described using Sérsic profiles with indices n=1 and n=4, respectively. The general form of the Sérsic Law (Sersic 1968), can be expressed as,

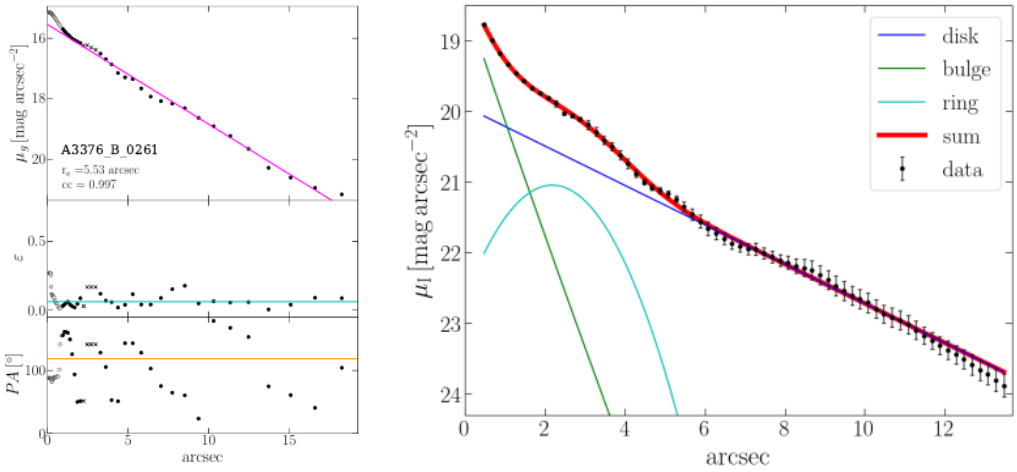

Figure 3.9: The fit for the surface brightness profile fit, ellipticity and PA (left panel); the galaxy decomposition into different structural parameters based on the surface brightness profile (right panel) for A3376_B_0261. (Franchetto et al. 2018).

$$I(r) = I_e.e^{b_n[(r/r_e)^{1/n}-1]} \tag{3.4}$$

where r_e is the effective radius, which marks the radius from which half of the total luminosity is emitted; I_e is the intensity at the effective radius; b_n is a function of Sérsic index n; r is the radial distance from the centre of the galaxy; and Intensity I is the logarithmic equivalent of surface brightness profile, also presented as,

$$\mu(mag/arcsec^2) = -2.5\ \ logI + const \tag{3.5}$$

where μ is the surface brightness in magnitude units of mag/arcsec^2 and I is the intensity or the surface brightness in physical units of $L_\odot$/pc^2.

- The bar is a central substructure and is fitted using Ferrers' law (Ferrers 1877).
- The ring is a star forming ring that results in the presence of humps in the SBP of galaxies. The rings usually mark the sites of active star formation.

These different components can be seen in the Figure 3.9. Finally, the SBP expressed in magnitude units is fitted with a linear regression as shown in Figure 3.9. Further, this helps in identifying the different structural parameters from the surface brightness profile as shown by the structural decomposition in Figure 3.9, for galaxy A3376_B_0261 (Franchetto et al. 2018). The possible presence of a bulge adds another component to the SB profile using which the bulge radius is also estimated as the radius at which the luminosity due to the

bulge equals the luminosity due to the disk. The procedure closely follows the methods of Sánchez-Blázquez et al. (2014) which can be referred to for further details.

The same procedure was implemented to extract the structural parameters for each of the galaxy and the final parameters for R_e, $R_{bulge,photo}$, PA and e for all galaxies of our sample are listed in Table 3.2.

3.5 De-Projected Distances

Now that we have the position angle and ellipticity for each of the galaxies, we can derive the deprojected radial distance of each spaxel in the galacto-centric frame. As explained in section 3.1, we have already converted our galaxy frames to galacto-centric coordinates $x_g = x - x_c$ and $y_g = y - y_c$, where (x_c , y_c) are the coordinates of the centre of the galaxy and the (x,y) are the coordinates of the initial image. Once we have the coordinates centred on the galaxy's centre, we rotate the galaxy frame by the position angle using the following equations:

$$\begin{aligned} x' &= x_g.sinPA - y_g.cosPA \\ y' &= x_g.cosPA + y_g.sinPA \end{aligned} \tag{3.6}$$

Finally, the positions are deprojected on the galaxy plane and the distance for each pixel is estimated from the centre of the galaxy using the following equation,

$$R^2 = x'^2 + \left(\frac{y'}{(1-e)}\right)^2 \tag{3.7}$$

where R is the deprojected distance of each pixel, and e is the ellipticity of the galaxy.

In order to do a radial analysis and compare for all the galaxies, the deprojected radial distance estimated with equation 3.7, is normalised by using the effective radii, as R/R_e.

3.6 Stellar Ages

Stellar ages are obtained by running the χ^2 procedure in the spectrophotometric code on the galaxy spectra to obtain ages spanning from 10^7 to 10^{10} years, with the maximum age being less than the age of the Universe at the redshift of these galaxies.

However two different ages are obtained from this χ^2 routine, namely the luminosity-weighted age and the mass-weighted age. The two different ages originate as a consequence of the fact that the very young, massive stars formed during the last 10^8 years dom-

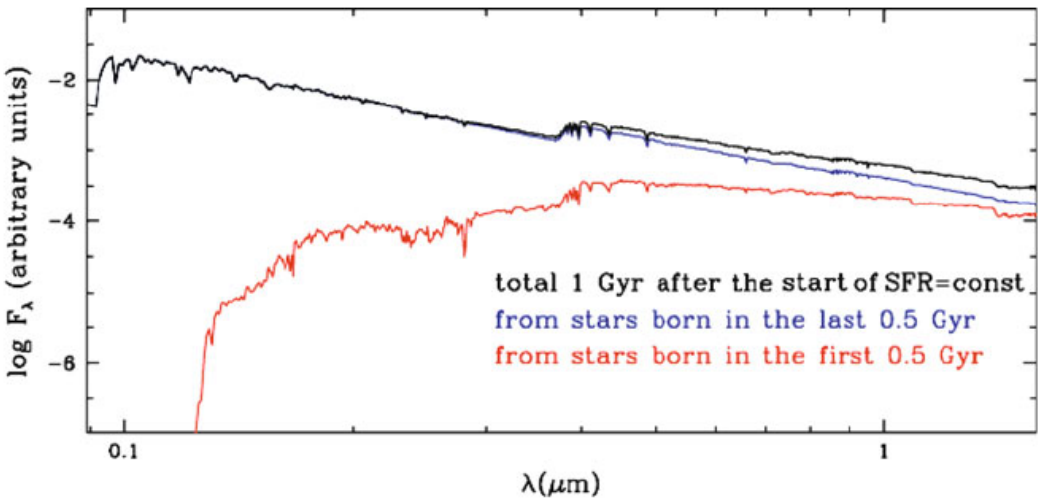

Figure 3.10: The effect of outshining the older generations by the youngest generations in a composite stellar population, for a constant SFR rate over 1 Gyr as shown by, Maraston et al. (2010). The contribution of the stars formed during the first and the second half of this period are shown separately as indicated by the color code, together with the spectrum of the full population.

inate the light at most wavelengths in actively star-forming galaxies, even if they represent a fairly small fraction of the galaxy's stellar mass (Maraston et al. 2010). The capability of a very young population to outshine previous stellar generations is illustrated in Figure 3.10. As can be seen from the figure, the young component clearly outshines the old component at all wavelengths, making it difficult to assess the presence and the contribution of the latter one, even if the old component may contain more than half the total stellar mass. Hence, we reach the two different stellar age definitions. The age of the stars producing the bulk of the light is called the luminosity-weighted age (LWA), and the age since the beginning of the star formation in the galaxy is called the mass-weighted age (MWA). These are defined through the following equations (Citro et al. 2016),

$$MWA = \frac{\int_0^t SFR(t-t').M_*(t').t'dt}{\int_0^t SFR(t-t').M_*(t')dt} \tag{3.8}$$

$$LWA = \frac{\int_0^t SFR(t-t').f_\lambda(t').t'dt}{\int_0^t SFR(t-t').f_\lambda(t')dt} \tag{3.9}$$

where $M_*(t')$ is the stellar mass provided by a single stellar population (SSP) of age t′, f_λ is the flux at a given wavelength of an SSP of age t′ and SFR(t−t′) is the star formation rate at the time (t−t′), when the SSP was formed. These equations account for the fact that a

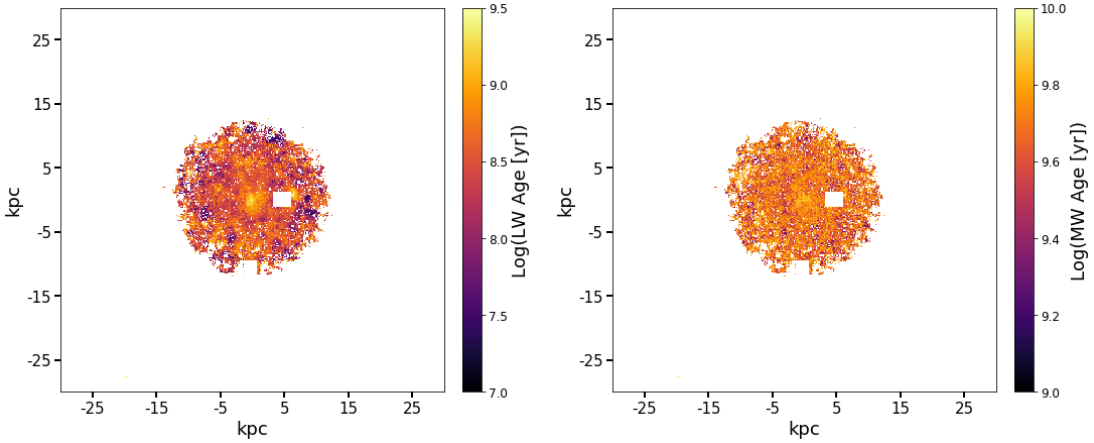

Figure 3.11: The luminosity weighted age map (left) and the mass weighted age map (right) for the galaxy A3376_B_0261. Both present a different range of values as presented by the colorbar.

composite stellar population (CSP), like in a galaxy, can be treated as the sum of many SSPs of different ages. Thus each SSP, with a certain age t′, contributes to the global mass-(light-) weighted age of the CSP according to its mass (flux).

It should be noted that since the LWA is most sensitive to the UV part of the spectrum, it is representative of the current SFR as derived from the spectral energy distribution (SED). On the other hand, the MWA being more sensitive to the near-IR part tells about the global SFH and hence the overall accumulated M_*. Figure 3.11 presents the luminosity-weighted and mass-weighted age maps, for the galaxy A3376_B_0261. It is worth noticing from these age maps that the MWA show clearly greater values, which is expected since the LWA represent only the younger stellar populations.

3.7 Spatial Binning of data

Since we are using galaxy spaxels over the entire radial range until the galaxy outskirts, we spatially bin the data points in intervals of 0.1 R_e. This is also useful for values representing the outer galaxy regions with lower signal-to-noise ratio.

3.7.1 R_{max} Parameter

Using these binned regions, the maximum radial limit, the R_{max} was estimated for each galaxy separately. This parameter defines an upper limit of the radial distance of spaxels from the galaxy centre that shall be used in the analysis. Since the outer bins have a very few pix-

els per bin, it was chosen to retain only the bins with more than 20 pixels. This number was chosen to ensure we do not incorporate any bins with noisy pixels from the galaxy outskirts, thereby also justifying our choice of SNR>1 cut. The radial distance of this last bin is then taken as the R_{max}, which is the maximum radial range till which the study of the stellar population properties is done in this work.

This R_{max} limit is also compared with the maximum radius identified from the Hα map of the galaxy ($R_{H\alpha}$). Hα traces the ongoing star formation in the galaxy and hence serves as a good comparison to check the extent of the stellar component. Figure 3.12 shows the RGB image of A3376_B_0261 with the R_{max} depicted by the red ellipse and the $R_{H\alpha}$ depicted by the green ellipse. As can be seen, the two ellipses are quite similar. This was checked for all the galaxies and the two ellipses either matched in each case or the R_{max} estimate was more precise than the $R_{H\alpha}$ to trace the stellar disk component as seen in the RGB composite images. The R_{max} values for the galaxies are listed in the Table 3.2.

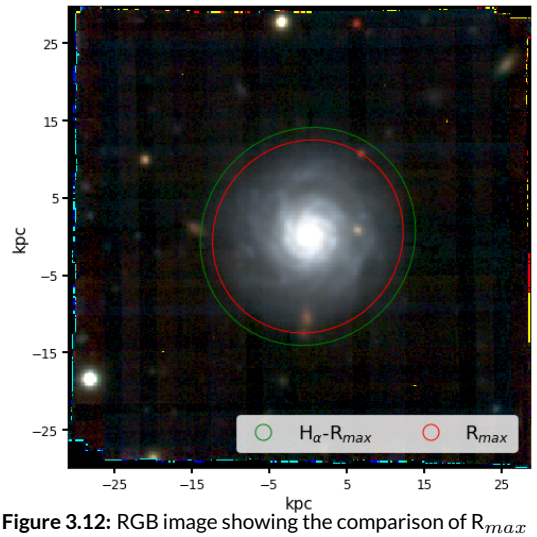

Figure 3.12: RGB image showing the comparison of R_{max} (red) and $R_{H\alpha}$ (green) for galaxy A3376_B_0261.

3.7.2 Estimating values in each bin

The distribution of the pixels for each bin, in steps of 0.5 R_e (instead of 0.1 R_e, for ease of representation) is shown in Figure 3.13. In order to remove the outliers and get a gaussian distribution, the $\kappa - \sigma$ clipping was applied in each bin of 0.1 R_e. The points removed due to the $\kappa - \sigma$ clipping can be seen as the light grey points in Figures 3.14 and 3.16. This clipping helped obtain a gaussian distribution in each bin and hence the representative age value of the bin and the error associated to the value were taken as the mean and standard deviation values respectively. These errors estimated here are then presented as error bars in Figure 3.16.

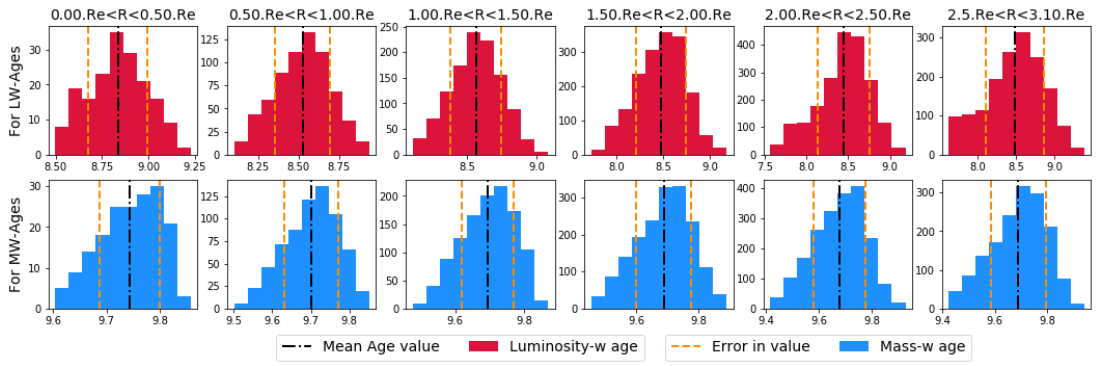

Figure 3.13: Distribution of the LW-age values (upper panel) and the MW-age values (lower panel) for bins of 0.5 R_e. The outliers were removed with $\kappa - \sigma$ clipping after which the mean value (black line) and the standard deviation (yellow line) were estimated.

3.8 Radial variation of Stellar Properties

Now that we have the SFR and age values for each pixel of the galaxy (as can be seen in Figure 3.7 and Figure 3.11), and the deprojected distance of each pixel from galaxy centre, we can next obtain the radial variations.

3.8.1 Radial Variations of SFR

Figure 3.14 represents the radial variation of the star formation rates in the four different age bins as specified earlier for galaxy A3376_B_0261. As can be seen from the figure, all the four age bins show a negative radial trend as expected with respect to the normalised R/R_e distance from the centre of the galaxy. This signifies that moving from the interior of the galaxy to the outer regions, the Star Formation Rate is decreasing in all the age bins. It should be noted that the SFR ranges are seen to be different in all the four age bins thus indicating variable star formation histories of the galaxy over the different timescales.

While smooth trends can be seen for the older age bins, the younger age bins show a comparatively more uneven radial trend. Each of the blue point in the figure represents a SFR value for a pixel. The binned average values are represented with the black points overlapping the blue SFR points. The grey points that can be seen in the background are the points clipped due to bin-wise $\kappa - \sigma$ clipping. The red vertical line represents the R_{max} cut as described before and the pixels beyond it are not accounted for in the analysis and are represented as open circles in the plot.

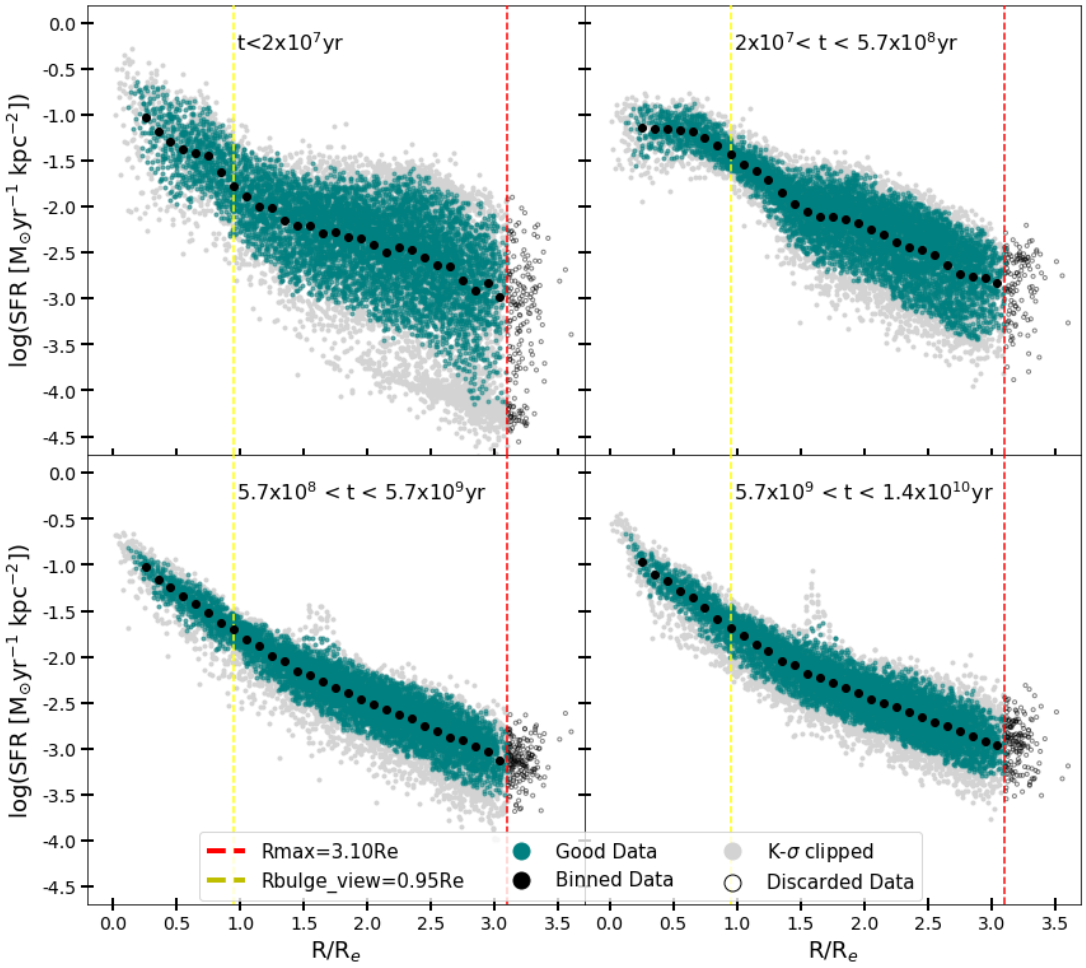

Figure 3.14: Radial variation of the SFR for the galaxy A3376_B_0261 in the four different age bins. Each blue data point represents a clean pixel from the SFR map.

3.8.2 Radial Variations of Age

The radial variation of the LWA and MWA was obtained with respect to the normalised and deprojected distance (R/R_e) of each pixel from the galaxy centre.

Each data point in the Figure 3.16, corresponds to a spaxel in the age maps seen in Figure 3.11. The bigger black points represent the binned values in steps of $0.1R_e$ as explained in section 3.7.

The discarded pixels to the left of the yellow

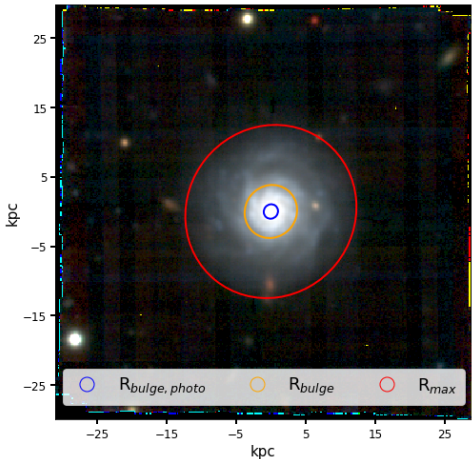

Figure 3.15: RGB image showing the distinction between R_{bulge} and $R_{bulge,photo}$ for A3376_B_0261.

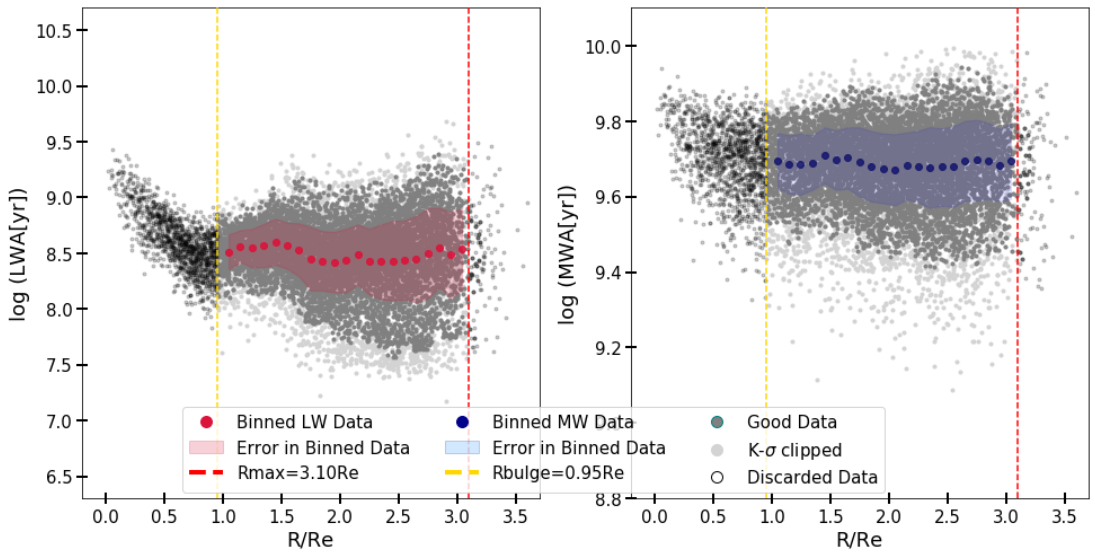

Figure 3.16: Radial variation of the Luminosity-weighted age (left) and Mass-weighted age(right), wrt R/R_e for the galaxy A3376_B_0261. The red and blue data points respectively represent the binned log(LWA) and log(MWA) values.

vertical line in Figure 3.16, represent the pixels belonging to the bulge. The bulge estimate obtained through the photometric analysis as explained in Section 3.4 refers to the radius where the contribution of the bulge equals the disk ($R_{bulge,photo}$). For the purpose of this thesis, it was decided to use a more conservative definition of the bulge, which extends the radial extent of the bulge to minimise the contribution of also the low-luminosity pixels belonging to the bulge for the analysis of LWA and MWA of the galaxy disk. Hence, this forms the definition of the R_{bulge} for this work. Figure 3.15 illustrates the distinction in these two boundaries by over-plotting the corresponding ellipses at these two distances over the RGB image of the galaxy. For most of the galaxies, the R_{bulge} marked the distance from galaxy center at which a clear break could be seen in the radial age-profile probably due to the transition from a central substructure to the disk. This break can also be seen in the LWA- radial profile in Figure 3.16 (left panel).

3.9 Stellar Age Gradients

The main aim of this thesis is to conduct a quantitative study of how stellar mass is growing in the galaxy disk. To find the disk age gradients, the range spanning from R_{bulge} to R_{max} was exploited. To obtain a robust estimate of the age gradients, three different methods were used to compute them. The outputs of the three methods were then compared to assess

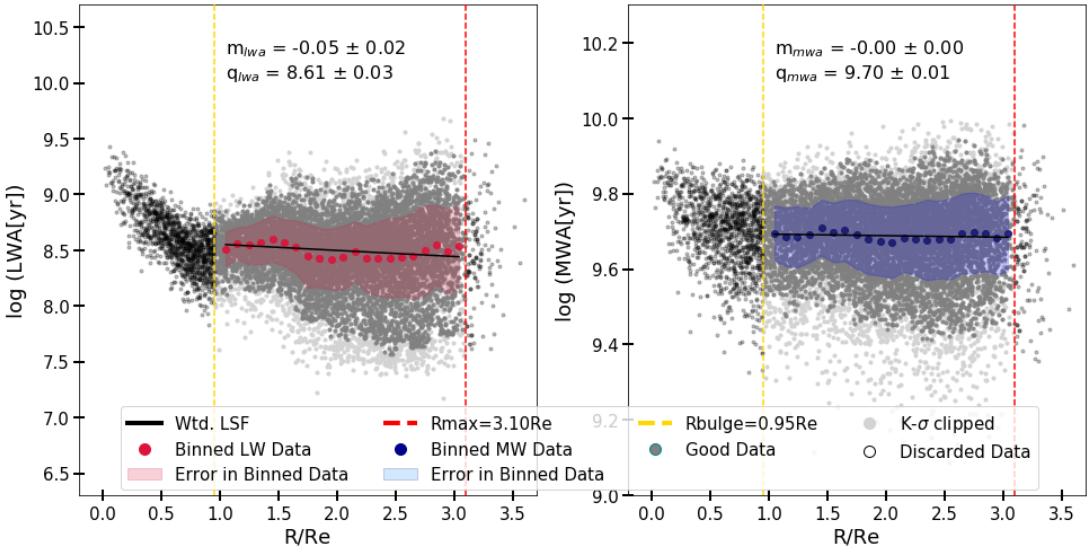

Figure 3.17: Estimating the age gradient using method 1 outlined in section 3.9.1, by using the error-weighted least square fitting for luminosity (left panel) and mass (right panel) weighted ages. The black line shows the weighted LSF line and the respective values of slope (m) and intercept (q) obtained through the fit are mentioned in the plot.

the reliability of the different results. This section elucidates these different methods and compares the results obtained with each. Further this section also explains how the galaxy age was obtained using the gradient values in different regions of the galaxy.

3.9.1 Age Gradient 1: Weighted Least Square Fitting

Figure 3.17 shows the binned LW (red) and MW (blue) age values along with their errors. A least square (LS) regression was implemented weighing each binned value against the respective errors by $1/\sigma$, where σ is the error associated with each data point.

Figure 3.17 illustrates the LS fitted line for both the luminosity and mass weighted ages. The values obtained for the slope and the intercept of the fitted line are also annotated in the plot, for galaxy A3376_B_0261.

3.9.2 Age Gradient 2: Bootstrapping the Binned Points

Followed by the least square estimate, the bootstrapping technique for the binned points was incorporated as seen in Figure 3.16.

Bootstrapping is a statistical re-sampling technique used to estimate statistics of a population by sampling a dataset with replacement. The technique is used to create a new sample of data by re-sampling ('n' no. of points) from the original data set (also of size n) with re-

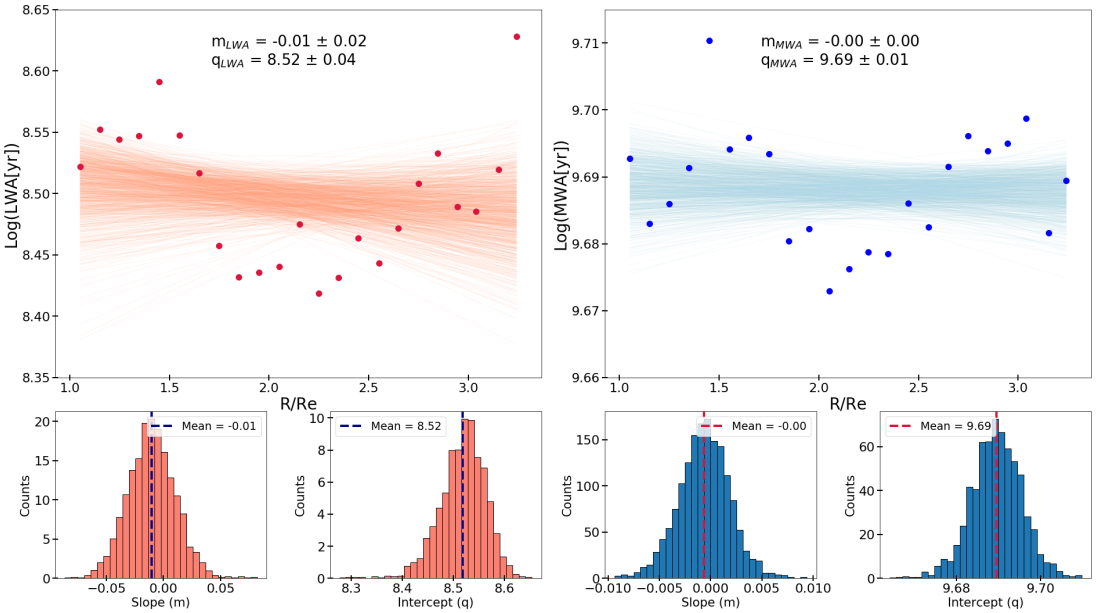

Figure 3.18: The estimation of age gradient using the bootstrapping method with 2000 repeats for LWA(left panel, in red) and MWA(right panel, in blue). Only the binned values (as can also be seen in figure 3.16) are used here as highlighted by the red and blue data points. The lower panels show a distribution of the slope(m) and intercept(q) values obtained from each bootstrapped repetition. Finally, the mean values are used as also annotated in the respective upper panels.

placements. This means in order to complete n data points, the algorithm is allowed to make repetitions and use the same values again, if required. For each new generated sample, an estimate of the slope and intercept of the line fitted through these points using error-weighted LS regression is obtained. This step was repeated about 2000 times, i.e., the data was bootstrapped 2000 times to obtain a distribution of slopes and intercepts from each repetition. Figure 3.18 shows in the upper panels the 2000 fitted lines. Each line was fitted on a resampled data sample from the original sample of binned values, shown in the figure in blue and red for LWA and MWA respectively.

The distribution of the slope and intercept obtained for each age is shown in the subpanels below the plots. As can be seen, each of the distribution shows a gaussian distribution. Hence, the distributions were summarised by estimating the mean value of slope as the age gradient, and the mean value of intercept as the age of galaxy at $0R_e$. Along with these values, the respective errors (standard deviation) associated to each value for both the mass and luminosity weighted ages were also obtained.

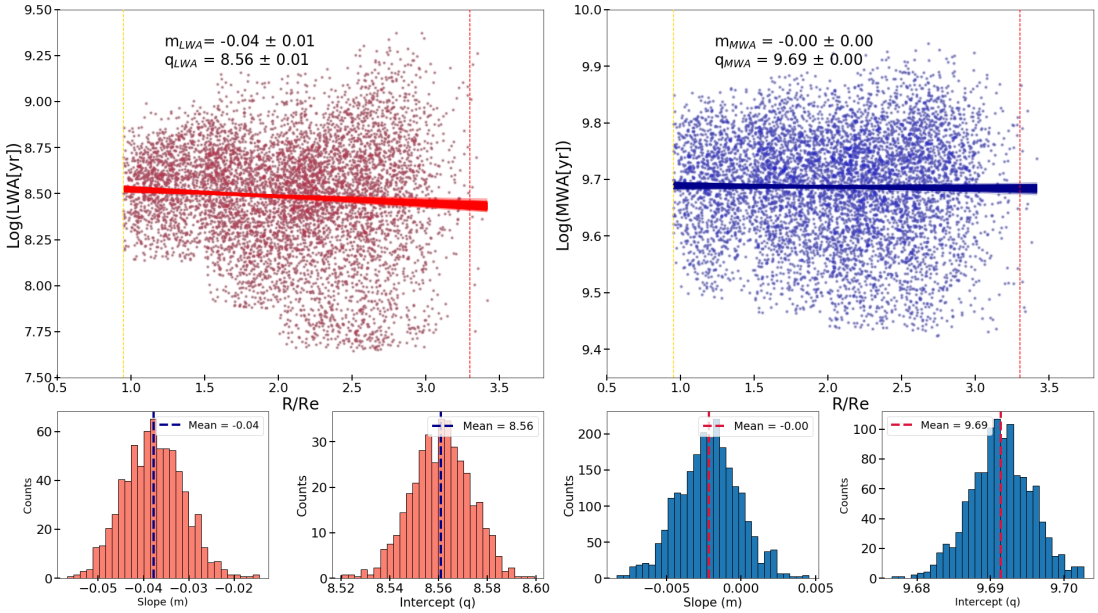

Figure 3.19: Estimating age gradients using the third method to bootstrap all pixels in the range of R_{bulge} to R_{max}. The obtained values are annotated in the text for luminosity weighted (left panel) and mass-weighted (right panel) ages.

3.9.3 Age Gradient 3: Bootstrapping all the data points

After obtaining age gradient estimates using the binned points in the above two methods, it was also decided to check the reliability of using the binned points to represent the whole data sample. Hence in order to compare the previous obtained estimates, the bootstrapping of all the available data points as shown in dark grey in Figure 3.16 was also done.

Figure 3.19 represents the same technique of bootstrapping repeated 2000 times as in the previous section. However the data sample this time has much more points and hence the resampled data set also had an equivalent increase in points. It should be noted here that the grey points of Figure 3.16 are shown in the Figure 3.19 in red and blue for LWA and MWA respectively in order to highlight that all these colored points have been bootstrapped.

3.9.4 Comparative study

The three methods were used to estimate the age gradient values for all the 34 galaxies of our sample. Table 3.1 summarises the values obtained for the age gradient and Age at $0R_e$ using the three methods for galaxy A3376_B_0261.

As can be seen from the table, the values are indeed very close to each other, thus confirming the consistency of the result. This check was performed for all 34 galaxies and Figure

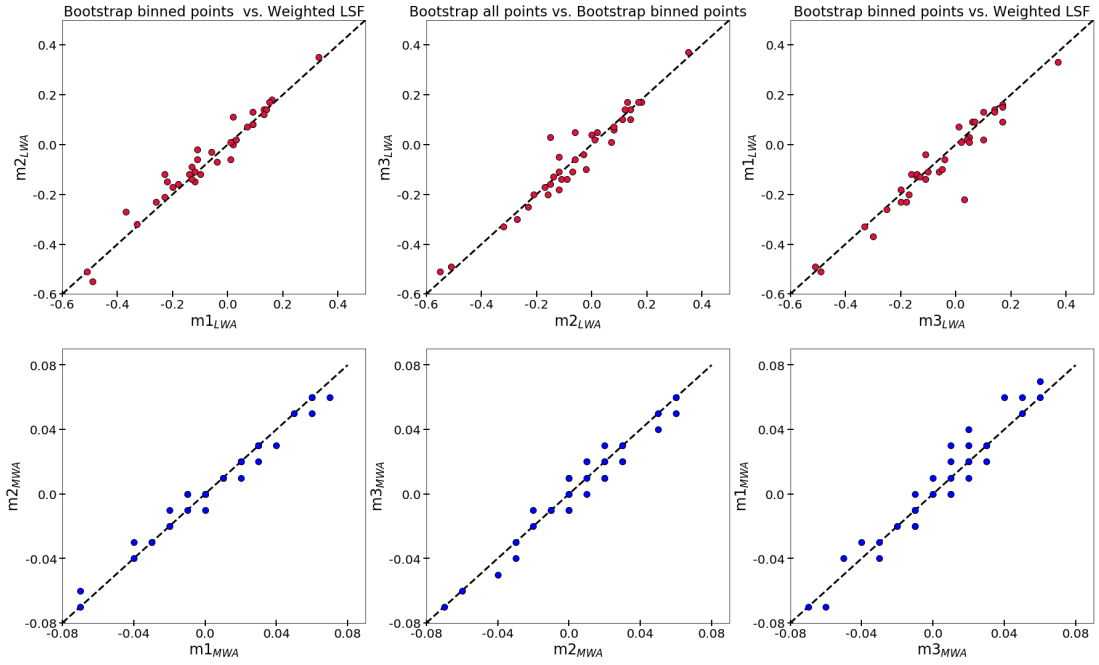

Figure 3.20: The figure presents a comparison of the slope values obtained with the three methods for luminosity-weighted (above panel) and mass-weighted (lower panel) ages. It is evident that all three methods give similar age gradient values.

Table 3.1: Table with the estimated values for age gradient and the age at centre for galaxy A3376_B_0261, using the above three methods.

LWA	**Method 1**	**Method 2**	**Method 3**
Age Gradient (m)	-0.05 ± 0.02	-0.01 ± 0.02	-0.04 ± 0.01
Age at centre (q)	8.61 ± 0.03	8.52 ± 0.04	8.56 ± 0.01
MWA	**Method 1**	**Method 2**	**Method 3**
Age Gradient (m)	-0.00 ± 0.00	-0.00 ± 0.00	-0.00 ± 0.00
Age at centre (q)	9.70 ± 0.01	9.69 ± 0.01	9.69 ± 0.00

3.20 presents the comparison between the three methods. As can be seen, the points seem to overlap with the 1:1 correlation line thereby ascertaining the accuracy of our age-gradient estimates. A same comparison can also be seen for the intercept values shown by Figure 3.21.

Since all the methods gave similar results, they seemed to be at par with each other. However, since in the bootstrapping technique we can resample our data multiple times to produce a new estimate every time, we prefer to use it as it helps increase the accountability of our result. Hence the method 2, i.e., error-weighted bootstrapping regression on the binned points for all the galaxies to obtain the respective age gradients was adapted to obtain the fi-

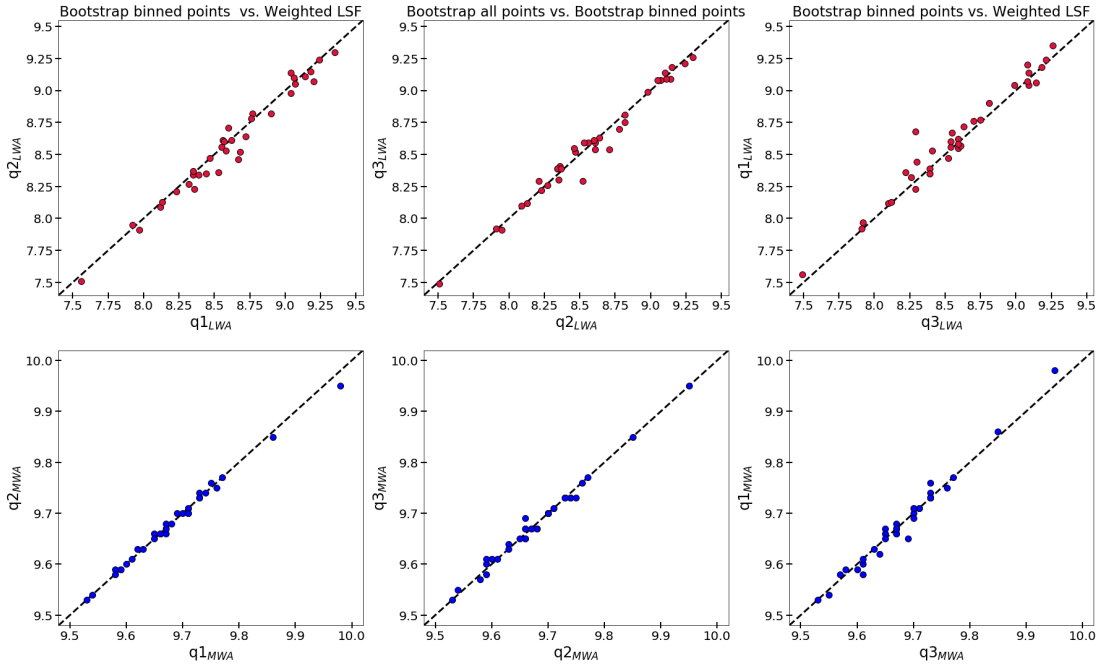

Figure 3.21: The figure presents a comparison of the intercept (q) values obtained with the three methods for luminosity-weighted (above panel) and mass-weighted (lower panel) ages. Again, we get similar values from all three methods for the ages at centre as well.

nal age gradient values. The plots illustrating the estimation of age gradients for all the other galaxies can be seen in Appendix A.1.

3.9.5 Average Age estimates

The LWA and the MWA were evaluated using the age gradient values at two radial positions of the galaxy namely, the galaxy centre and at $1R_e$.

1. Galaxy age at the centre
   - Using the data: Average value estimated from all the pixels within a radius of 5 Kpc from the centre.
   - Using the fit: The fit described in the previous section was extrapolated till $0R_e$ to obtain the central age value from the fit.

2. Galaxy age at $1R_e$
   - Using the data: The value of the binned data point corresponding to $1R_e$ from Figure 3.16
   - Using the fit: The value of the fit at a distance of $1R_e$ from the centre.

Very different values at the centre from the data and from the fit also highlight the presence of a break in the age radial profile which can be used as an indication for the presence of a bulge in the galaxy. Further, these different age estimates can be an effective way to look for broad spatial trends in the average ages of stellar populations as a function of the galactocentric distance.

3.10 Star Formation History

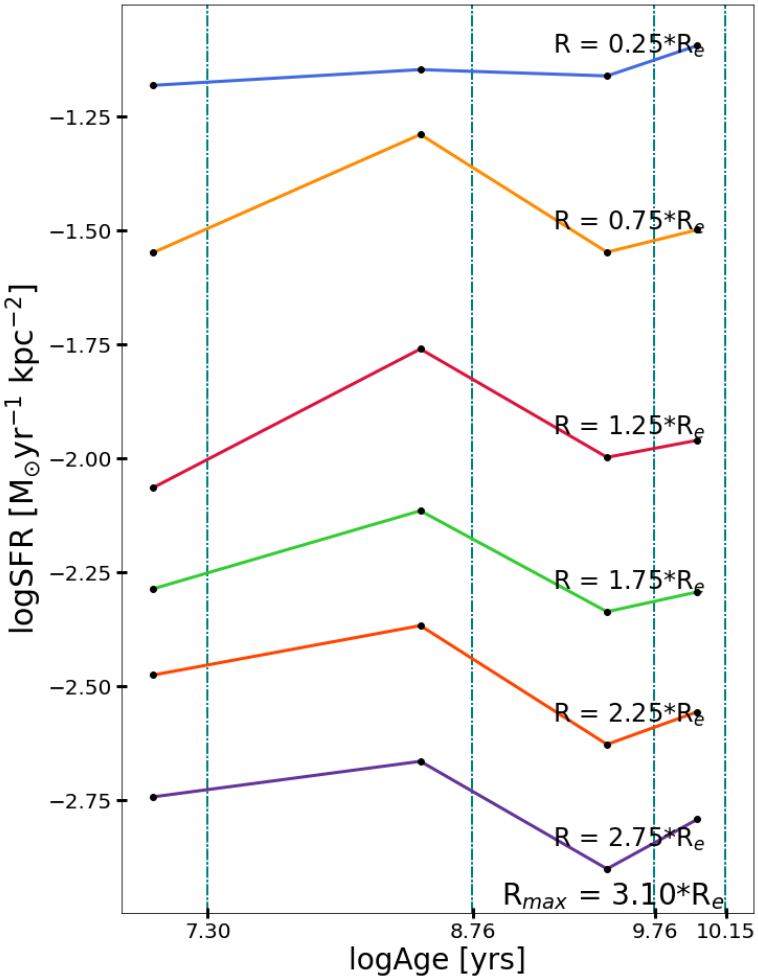

Figure 3.22: Star formation history for A3376_B_0261. The plot represents the SFR density in different regions of the galaxy, at steps of 0.5 R_e, plotted against the four main age bins. Both axis have log values.

The assembly of M_* is a long standing issue in the field of galaxy formation and evolution. To elucidate how M_* evolves, one would expect to recover the spatially resolved Star Formation History (SFH), both in space and time, for individual galaxies.

SFH is the fraction of stellar mass produced as a function of time in the form of SSPs. In fact, in practice the SFH of a galaxy is determined by finding the best fitting combination of SSPs that match its observed spectrum or spectral energy distribution.

The SFH in Figure 3.22 was obtained by using the SFRs in the four age bins computed with SINOPSIS and taking the average values in the radial bins. Both the SFR and the extinction, parametrized as E(B-V), was left completely free to vary, independent of the age (i.e. without assuming any analytical function). This allowed the SFR (and extinction) of the stellar populations of each age, to assume any value, without them being correlated.

In order to find possible trends in the SFH of the galaxies, as a function of their position, we plot the SFR of different regions w.r.t. the four different ages. Basically, for a spatial treatment, we divide our galaxy into different elliptical annuli at steps of 0.5 R_e, until the maximum radial distance of R_{max}. For each of these regions, we estimate the average SFR in the four different age bins. In Figure 3.22, we can see the SFH of the galaxy A3376_B_0261.

From the SFH plot, we can see that the SFR has been higher in the centre of the galaxy, as compared to the outskirts throughout the four age bins. Further, after the first SF episode, the galaxy underwent a decrease in the SF-activity, followed by a subsequent star formation episode. Relative to the previous SF episode, this second episode seems to be with a higher intensity in the outer regions of the galaxy than in the inner regions. Finally, in the most recent bin, the SF seems to have fairly subsided to lower rates all over the galaxy. We will discuss the implications of these results w.r.t. to the age gradients in the next chapter.

While the analysis in this thesis is based on the above mentioned assumptions and methods, it should be kept in mind that differences in, assumed cosmology, IMF, luminosity-to-SFR conversions, stellar population models, dust attenuation, and emission line contributions, can lead to differences in derived stellar masses and SFRs as high as a factor of two to three (Davies et al. 2016).

Table 3.2: Table listing all the values obtained from the photometric analysis, namely, Effective Radius (R_e), Photometric bulge radius ($R_{bulge,photo}$), ellipticity (e) and Position angle (PA). In addition to it, the table also summarises additional structural parameters like the R_{max} and the R_{bulge} as defined in section 3.7.1.

Galaxy	R_e ($''$)	e	PA ($^\circ$)	$R_{bulge,photo}$ (R_e)	e_{bulge}	PA_{bulge} ($^\circ$)	R_{bulge} (R_e)	R_{max} (R_e)
A3128_B_0148	2.3	0.541	119.3	0	0	0	0	3.2
A3266_B_0257	2.87	0.576	22.7	1.18	0.185	177	1.1	3.1
A3376_B_0261	4.51	0.052	141.1	1.06	0.016	36.4	0.95	3.2
A970_B_0338	3.86	0.705	4	0	0	0	1.1	2.8
JO102	2.86	0.649	32.6	0.86	0.388	36.6	0.3	2.9
JO128	6.69	0.077	95.4	2.1	0.561	91.6	0.6	2.3
JO138	4.15	0.708	1.2	2.36	0.46	174.8	0.75	2.9
JO159	3.81	0.231	69.9	0	0.319	33.9	0.75	3.3
JO17	6.78	0.494	63.5	0	0.38	87.2	0.5	2.4
JO180	3.56	0.1	150.7	0.28	0.08	34.5	0.6	2.2
JO197	4.14	0.438	3.4	0	0.452	4.3	0.8	2.8
JO205	3.66	0.41	138.8	1.65	0.188	125.6	0.75	2.8
JO41	5.08	0.102	77.2	1.27	0.329	110.9	0.55	2.1
JO45	3.8	0.443	99.3	0	0	0	0.65	2.6
JO5	3.88	0.269	23.5	0.24	0.129	32.2	1.1	3
JO68	4.4	0.433	66.3	0	0.425	64.7	1.1	2.3
JO73	4.24	0.162	75.3	0.83	0.408	156.8	0.5	2.5
P13384	3.37	0.125	171.2	0	0.109	148.4	0.9	2.5
P14672	2.93	0.113	12.1	0.75	0.181	131.6	0.55	3
P15703	5.08	0.571	153.8	0.97	0.139	162.6	0.8	4.2
P17945	4.08	0.252	40.3	0	0.222	50.3	0.5	2.4
P19482	4.75	0.419	126.9	0.23	0.058	10.6	1.1	4.5
P20769	2.55	0.444	53.9	0	0	0	0.6	3.2
P20883	4.24	0.438	166.4	0.37	0.221	169.5	0.5	2.5
P21734	6.76	0.152	110.6	0.43	0.117	85.8	0.65	3.4
P25500	8.12	0.353	105	1.03	0.075	101.1	0.5	3.3
P42932	5.75	0.233	130.3	0	0.161	125.9	0.8	2.6
P45479	5.24	0.391	32.3	0.76	0.166	42.8	0.25	2.7
P48157	5.95	0.342	114.9	0.6	0.131	91.7	0.8	3.1
P5215	5.17	0.266	133	0.65	0.059	139.1	0.7	2.4
P57486	4.18	0.448	100.5	0.25	0.106	104.3	0.55	2.6
P648	5.37	0.29	46.9	0.33	0.315	56.9	1.1	2.4
P669	6.36	0.157	147.5	1.16	0.184	125.1	0.6	2.4
P954	4.01	0.25	130.2	0.56	0.31	37.4	0.8	2.4

"Astronomy, as nothing else can do, teaches men humility."

- Arthur C. Clarke

4

Results and Discussions

The radial age gradients, of stellar populations are widely used as tools to understand galaxy evolution (Pérez et al. 2013; Ibarra-Medel et al. 2016; Pan et al. 2015; Goddard et al. 2017). Based on the sign of age gradients (positive or negative), galaxies can be categorized to grow using two types of progressions, inside-out and outside-in. This chapter presents the results obtained and the estimated age gradients for all the 34 galaxies of this sample using the methods described in the previous chapter. Further it discusses the dependence and variation of the gradients with respect to the stellar mass and morphology of the galaxy.

4.1 Observations and Outcomes

The structural parameters of each galaxy were recovered using a photometric analysis. With the values for effective radius, ellipticity and position angle, the deprojected distances could be obtained. Using these radial profiles of star formation and luminosity-weighted and mass-weighted stellar ages were derived as explained in Chapter 3. The photometric analysis revealed the presence of a bulge and/or a bar in some galaxies. Further the analysis of the surface brightness (SB) profile indicated the presence of a break resulting in an upward or downward bent in the SB profile. This is identified as a broken disk and is largely associated with the presence of a bar in late-type galaxies. This is discussed later in the chapter.

The stellar age profiles of some galaxies also displayed a break, thus featuring different

Table 4.1: Table enlisting the luminosity and mass weighted age gradient values as estimated from the error weighted bootstrapping technique for all the 34 galaxies of the sample. In addition, the age estimated at the centre, which translates to the intercept is also listed.

Galaxy	$\log M_*$ $[M_\odot]$	Age Grad_{LWA} [dex/R_e]	Age Grad_{MWA} [dex/R_e]	$\log LWA_{cent}$	$\log MWA_{cent}$
A3128B0148	9.85	0.20 ± 0.02	0.07 ± 0.01	8.04 ± 0.05	9.52 ± 0.02
A3266B0257	9.9	0.04 ± 0.02	0.03 ± 0.01	8.57 ± 0.04	9.65 ± 0.02
A3376B0261	10.5	-0.04 ± 0.02	-0.07 ± 0.00	8.58 ± 0.04	9.70 ± 0.01
A970B0338	10.1	0.07 ± 0.03	0.05 ± 0.01	8.70 ± 0.06	9.61 ± 0.02
JO102	10.0	0.23 ± 0.03	0.02 ± 0.01	8.17 ± 0.06	9.67 ± 0.01
JO128	9.9	-0.06 ± 0.05	0.01 ± 0.01	8.30 ± 0.07	9.67 ± 0.01
JO138	9.6	0.06 ± 0.02	0.03 ± 0.01	8.42 ± 0.04	9.64 ± 0.01
JO159	9.85	0.14 ± 0.02	0.01 ± 0.00	7.91 ± 0.05	9.62 ± 0.01
JO17	10.1	0.09 ± 0.02	0.06 ± 0.01	8.55 ± 0.03	9.58 ± 0.01
JO180	10.0	-0.08 ± 0.04	-0.01 ± 0.01	8.74 ± 0.06	9.71 ± 0.01
JO197	10.0	-0.04 ± 0.08	0.02 ± 0.01	8.36 ± 0.15	9.59 ± 0.02
JO205	9.52	-0.07 ± 0.03	0.06 ± 0.01	7.97 ± 0.06	9.52 ± 0.02
JO41	10.2	-0.14 ± 0.02	0.01 ± 0.00	9.08 ± 0.03	9.71 ± 0.00
JO45	9.18	-0.14 ± 0.04	0.02 ± 0.01	8.55 ± 0.07	9.64 ± 0.01
JO5	10.3	-0.60 ± 0.07	-0.01 ± 0.01	9.24 ± 0.15	9.64 ± 0.02
JO68	10.0	0.10 ± 0.03	-0.05 ± 0.02	8.40 ± 0.04	9.77 ± 0.03
JO73	10.0	-0.13 ± 0.07	-0.005 ± 0.01	8.37 ± 0.11	9.69 ± 0.01
P13384	9.85	0.38 ± 0.03	-0.02 ± 0.01	7.48 ± 0.05	9.71 ± 0.01
P14672	9.9	-0.17 ± 0.02	-0.004 ± 0.01	9.14 ± 0.04	9.73 ± 0.01
P15703	11.0	-0.12 ± 0.01	-0.06 ± 0.00	9.30 ± 0.03	9.96 ± 0.01
P17945	9.78	0.11 ± 0.05	0.05 ± 0.01	8.24 ± 0.08	9.60 ± 0.01
P19482	10.3	-0.33 ± 0.02	-0.006 ± 0.00	9.16 ± 0.05	9.70 ± 0.01
P20769	9.48	-0.16 ± 0.03	0.04 ± 0.01	8.63 ± 0.05	9.58 ± 0.01
P20883	9.9	0.15 ± 0.03	0.02 ± 0.01	8.30 ± 0.05	9.67 ± 0.01
P21734	10.8	-0.19 ± 0.03	-0.01 ± 0.00	8.67 ± 0.06	9.71 ± 0.01
P25500	10.8	-0.24 ± 0.02	-0.02 ± 0.00	8.99 ± 0.04	9.74 ± 0.01
P42932	10.5	0.03 ± 0.02	0.05 ± 0.01	8.58 ± 0.03	9.58 ± 0.01
P45479	10.6	-0.29 ± 0.02	-0.04 ± 0.01	9.09 ± 0.04	9.75 ± 0.01
P48157	10.6	-0.05 ± 0.04	0.03 ± 0.00	8.52 ± 0.09	9.61 ± 0.01
P5215	10.5	-0.03 ± 0.04	-0.03 ± 0.00	8.78 ± 0.07	9.77 ± 0.01
P57486	9.95	0.11 ± 0.02	-0.002 ± 0.01	8.17 ± 0.03	9.70 ± 0.01
P648	10.4	0.03 ± 0.08	-0.003 ± 0.01	8.58 ± 0.15	9.71 ± 0.02
P669	10.5	-0.23 ± 0.03	-0.09 ± 0.01	9.12 ± 0.05	9.87 ± 0.02
P954	9.6	0.02 ± 0.05	0.001 ± 0.01	8.29 ± 0.09	9.68 ± 0.02

slopes in different radial ranges. This hinted at the presence of a central sub-structure and indeed most of these galaxies showing a break, did have a bulge and/or a bar. From this observation, the definition of R_{bulge} adapted for this work was set to incorporate this break in the age profile. The presence of central sub-structures and breaks seen in stellar age and SB profile are summarised in Table 4.3 and are discussed thereafter in section 4.2.

To address the primary objective of this thesis, age gradients in the disk of the galaxy were to be computed. This called for considering only regions not significantly affected by the bulge. As described in the previous chapter, it was decided to use the technique of bootstrapped least square regression to estimate the disk age gradients for the galaxies of our sample. The plots describing the age gradient estimate for all the 34 galaxies are illustrated in Appendix A.1. This sample of regular galaxies displays a varying range of age gradients: flat, positive and negative, for both mass-weighted and luminosity-weighted ages. Table 4.1 enlists the estimated values for the LWA and MWA gradients (slopes) along with the age of galaxies at centre (intercepts).

4.1.1 Inside-Out or Outside- In

As summarised in Table 4.1, there is evidence for positive as well as negative slopes. The findings are presented taking an example galaxy of each gradient-type. Figure 4.1 shows the LWA and MWA radial profiles for two galaxies of different M_*:

1. P45479, a high mass galaxy, $M_* \sim 3.7 \times 10^{10}$ $M_\odot$
2. A3128_B_0148, a comparatively low mass galaxy, $M_* \sim 0.7 \times 10^{10}$ $M_\odot$

The black fitted-line in each plot traces the estimated age-gradient for each galaxy (for values, see Table 4.1). The bulge dominated region has been ignored for P45479, indicated by the region before the green line at 0.25 R_e. In order to only consider the disk region, the fitting was carried out only for a radial range from R_{bulge} to R_{max}. As can be seen from this comparison, while P45479 shows a negative age gradient, with older insides and younger outsides, thus presenting an inside-out scenario. In contrast to this, A3128_B_0148 galaxy shows a clearly positive nature of gradients with younger insides and older outsides and thus hinting at an outside-in progression. Hence, we see both evolution mechanisms coming to light.

Thus we can conclude, that the galaxies of our sample show radial dependence with the negative gradients pointing to an "inside-out" progression of star formation, and the positive gradient to an "outside-in" progression. The inside-out progression suggests that some disk instability above threshold gas densities, may have induced star formation in the galaxy centre. In these galaxies, the outer regions are seen to be forming through much gentler processes with star formation driven by gradual accretion of cold IGM. However, understanding

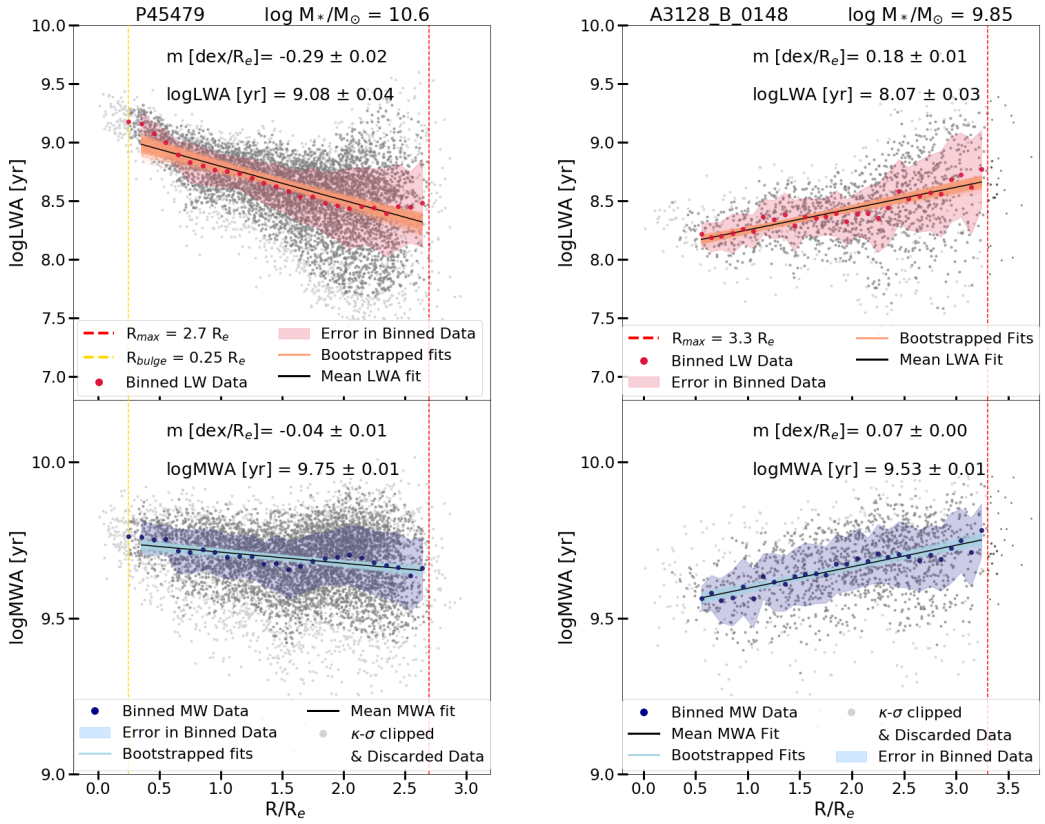

Figure 4.1: Radial variation of age for galaxy P45479 (left) and galaxy A3128_B_0148 (right). The upper panel is the mass weighted age and the lower panel the luminosity weighted age. In each sub-panel, the black line represents the fitted average age gradient for each case while the collection of lines behind the fitted line represents the range of fits from the bootstrap method, thus the confidence limit for the gradient values. The big dark red and blue points represent the binned values for MWA and LWA respectively and the shaded region is the associated error to each point. Notice the opposite nature of slopes for the two galaxies.

the main processes behind the outside-in formation scenario poses the main challenge. In order to ascertain our findings we also check the metallicity gradients of these galaxies. All the galaxies of this sample show negative metallicity gradients as estimated by Franchetto et al. (2018). The combination of flat to positive age gradients seen here, with negative metallicity gradients of these galaxies confirm an outside-in formation scenario in which star formation ceases slightly earlier in the outermost regions with younger, more metal rich stellar populations in the centre.

While outside-in progression is being reported for some galaxies, it should be cleared here that the current analysis does not attempt to discriminate between star formation quenching and rejuvenation. Quenching is when star formation subsides due to certain reasons and the galaxy is no longer actively forming stars. If the quenching progresses inwards, it would lead to a dormant galaxy outskirt with the inner regions still forming stars until they

are not quenched. Similarly, through a different approach of star formation revival in galaxy centres, a dormant galaxy may start to form stars again in the centre due to some disk anomalies. Hence, both inward progression of quenching and/or the rejuvenation of galaxy centres through late, residual star formation will lead to positive age gradients. Therefore, the outside-in formation reported here refers to the radial progression of star formation in galaxies, and not to galaxy assembly itself. In other words, the conclusions drawn here are not in conflict with the size evolution of galaxies and the fact that galaxies appear to have been more compact in the past. There is mounting evidence in support of the outside-in scenario in literature (Pérez et al. 2013, Wang et al. 2017). Various physical mechanisms maybe responsible for the same, which can be related to different galaxy properties as follows:

- Depending on galaxy stellar mass:
  Radial stellar migration, which may cause the older stars born in the centre to migrate to greater radial distances in low mass (and hence low potential) galaxies (El-Badry et al. 2016; Goddard et al. 2017)
- Depending on galaxy morphology:
  - Bulge dominated galaxies (Ellison et al. 2011; Wang et al. 2017)
  - Bar induced inflows of gas thus leading to enhanced SFR in the centre (Martel et al. 2013; Aumer et al. 2014; Fraser-McKelvie et al. 2019)
- Modifications to I-O mechanism due to angular momentum loss from reorientation of the galaxy disk or infalling gas with misaligned angular momentum (Aumer et al. 2014)

To understand the origin of this behaviour and to apprehend the different formation scenarios better, the dependence of age gradients on the above mentioned galaxy physical properties is analysed in the following sections.

4.1.2 Telltales from SFH

In an effort to corroborate our findings, we also compare the spatially resolved star formation history with the mass weighted age gradients for the two galaxies considered before. Figure 4.2 presents the SFH of both the galaxies. On following the peak of SF across different age bins, it can be seen that galaxy A3128_B_0148 had its peak star formation in the inner regions (uppermost gradient) during the youngest age bin (leftmost age bin) and in the outer regions (lowermost gradient) during older ages (rightmost age bin). This agrees well with the positive

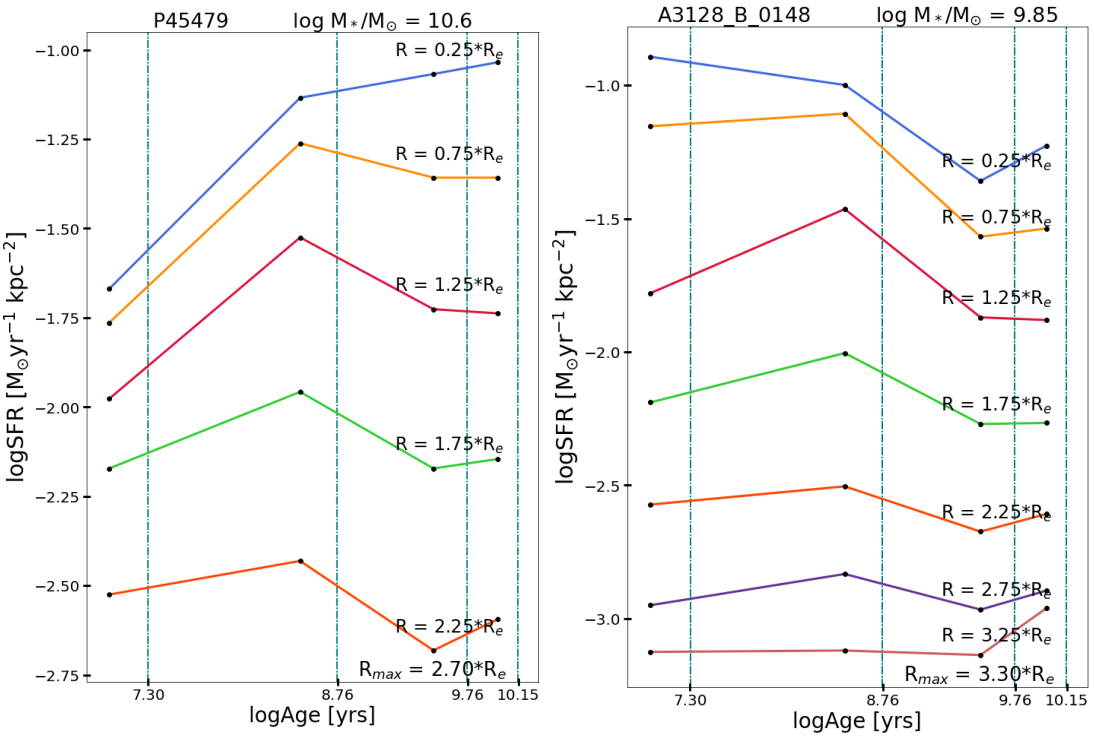

Figure 4.2: SFH of galaxy P45479 (left) and galaxy A3128_B_0148 (right). The different colors represent different annular regions of the galaxy divided at steps of 0.5R_e, from the inside of the galaxy (at the top) to the outskirts(at the bottom). As for all methods, the analysis is only till the R_{max} limit, indicated for both the galaxies. The opposite movement of the SF peaks can be seen clearly.

age gradient seen for this galaxy and testifies the outside-in nature. For galaxy P45479, we see an opposite behaviour with the peak of SF in the older ages in the inside of the galaxy and the peak of SF shifting gradually to the younger ages in the outskirts of the galaxy. For all the galaxies of our sample, we perform this check and barring a few exceptions, all the MWA gradients (which represent the overall star formation history) are seen to agree with the trends witnessed from the SFHs.

4.2 Dependence on galaxy physical properties

Various different physical processes contribute to the star formation and stellar mass assembly histories of galaxies. Observational evidence indicates that the spatial distribution of stellar mass build-up is related to the galaxy's physical properties, such as their stellar mass and morphology. In this section, we explore where and how strongly galaxies are forming their stellar mass as a function of their global properties.

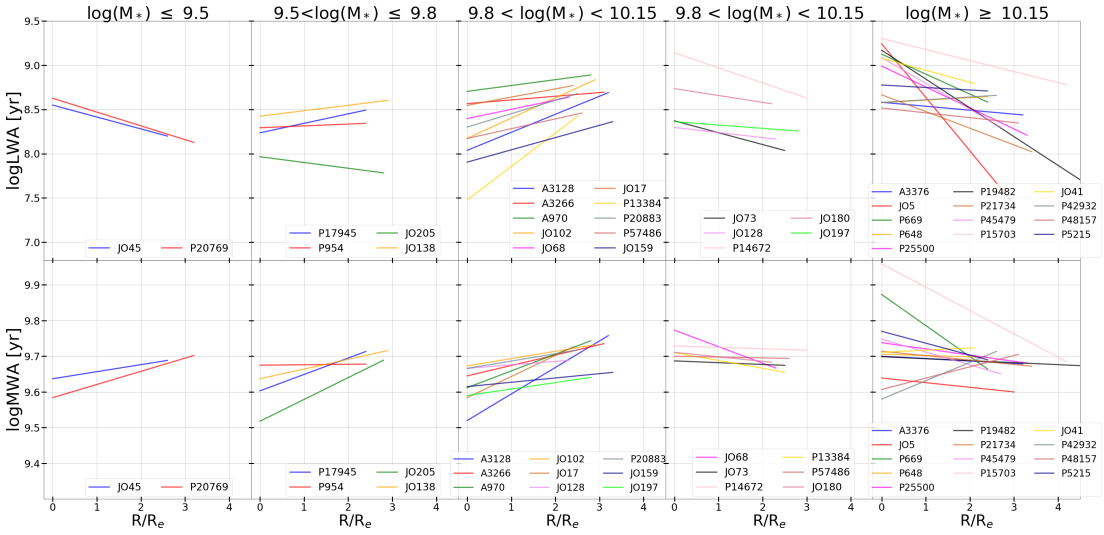

Figure 4.3: LW-age gradients (upper panel) and MW-age gradients (lower panel), divided in four M_* categories, with the third M_* bin divided in two, to visualise the positive and negative gradients separately.

4.2.1 Effects of galaxy Stellar Mass on age gradients

We investigate how galaxy mass assembly mode depends on stellar mass M_* using a resolved spatial study. The stellar mass of each galaxy was derived by SINOPSIS from the integrated spectrum of the galaxy main body, as described in Poggianti et al. (2017a). The continuum underlying Hα image was sliced in different count levels. The isophote enclosing the spaxels with surface brightness $\sim 1\sigma$ above the background level, was assumed to represent the galaxy main body. The galaxy spectrum was then integrated within this isophote and the SINOPSIS was run on this integrated spectrum to derive the global stellar mass. Our galaxy sample covers a stellar mass range of $9.18 < \log M_*/M_\odot < 11$. The total stellar mass of the galaxies are reported in Table 4.1.

In order to comprehend the reliance of age-gradients on the stellar mass, the $\log M_*$ range was divided into 4 different categories as below:

- $\log M_* \leq 9.5$
- $9.5 < \log M_* \leq 9.8$
- $9.8 < \log M_* < 10.15$
- $10.15 \leq \log M_* \leq 11.0$

Using these divisions based on M_*, the age gradients for galaxies falling in each category were plotted separately for mass and luminosity weighted ages as indicated in Figure 4.3. As

can be viewed in the figure, both the mass and luminosity weighted age gradients show clearly negative slopes for the high mass galaxies ($\log M_* \geq 10^{10.15}$) and mostly positive/flat slopes for lower masses ($\log M_* < 10^{10.15}$). There are inevitably also a few exceptions to this case. The stellar mass range of $\log M_* \in (9.8, 10.15)$, has been shown in two separate panels in Figure 4.3. This is done to clearly differentiate between both the positive and negative gradients seen in this range. Above and below this range, we can see an almost clear trend. It should be noted that there are also some galaxies that show opposite nature of gradients for mass and luminosity weighted gradients with one being positive and the other negative. For this analysis, these cases are termed as showing a 'mix' behaviour. Table 4.2 summarises the age gradients as seen in Figure 4.3 for different stellar mass ranges.

Table 4.2: Table summarising the different nature of gradients seen for the 34 galaxies.

Total Galaxies : 34			
Low Mass Galaxies : 21 ($\log M_*$<10.15)		High Mass Galaxies : 13 ($\log M_*$>10.15)	
inside-out (-ve)	3	inside-out (-ve)	12
outside-in (+ve)	10	outside-in (+ve)	1
mix*	8	mix	0

For an articulated view, Figure 4.4, presents the cumulative plot of the age gradients vs. the galaxy stellar mass for all 34 galaxies. It can be seen at once from this figure that the age gradients do show a pattern w.r.t M_*. While the high M_* galaxies show increasingly negative age gradients, the low M_* galaxies show positive or flat (zero) age gradients.

This reflects a transition trend from outside-in to inside-out for galaxies as the stellar mass increases (as can be witnessed from the negative slope in the Figure 4.4). It is not surprising to see that the galaxy assembly modes have strong dependence on M_*. This is since, it is the gravitational force that a galaxy can exert, which defines its capability to accrete new gas that rebuilds its outskirts, or retrieves the lost gas.

It should also be observed that mass-weighted age gradients, are in general increasingly flat as you move to the outskirts, with values very close to 0 (as can be seen from stellar age profiles in Figure 4.1 and the appendix plots). While the logLWA gradients cover a range from -0.7 to 0.4 dex/R_e, the logMWA gradients have ranges very close to flat from -0.08 to 0.09 dex/R_e (see Figure 4.4). This may hint at the fact that any excess of star formation in the out-

*As described before, the positive gradients represent an Outside-In mechanism while the negative gradients represent an Inside-Out phenomena. The "Mix" category represents the galaxies whose gradients for mass and luminosity weighted ages don't agree.

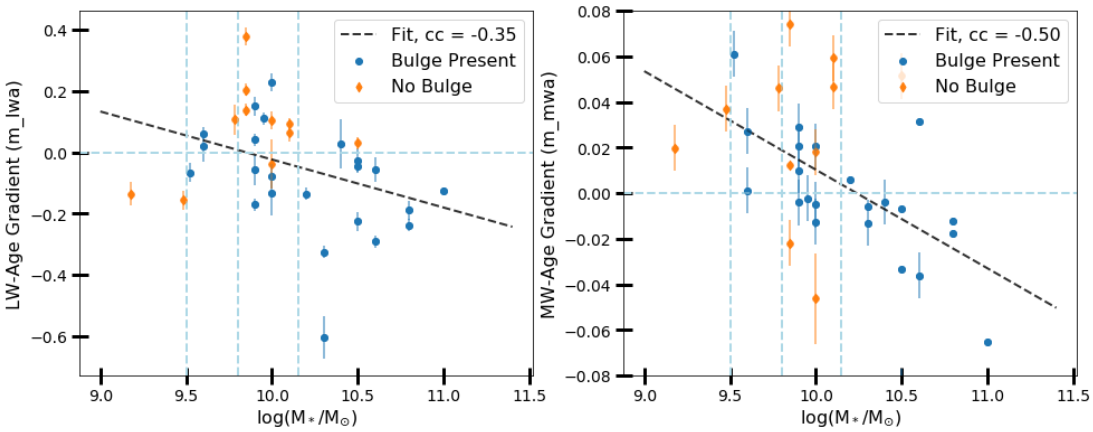

Figure 4.4: Analysing the dependence of LW (left) and MW (right) age gradient w.r.t. $\log(M_*/M_\odot)$. The vertical lines highlight the divisions of M_* as per the Figure 4.3.

skirts of galaxy disks compared to the centre must be small and hence does not contribute significantly to the overall mass budget.

In summary, we see that most of the low mass galaxies are forming their mass more strongly in the insides (positive gradients) thus supporting an outside in mechanism or everywhere and equally at all radii (flat gradients; Bernard et al. 2007; Gallart et al. 2008; Zhang et al. 2012; Pérez et al. 2013; Pan et al. 2015). In contrast to this, almost all of the high mass galaxies show inside-out phenomena (negative gradients; (Muñoz-Mateos et al. 2007; Bezanson et al. 2009; Patel et al. 2013; van de Sande et al. 2013; Tacchella et al. 2015; Goddard et al. 2017; Wang et al. 2018; Pérez et al. 2013; Rowlands et al. 2018). The analysis done for MaNGA galaxies by Rowlands et al. (2018), based on spatially resolved SFH did not quantify the rate at which mass is being built by star formation and they were thus unable to identify the mass-growth mechanism. This point was also made by Wang et al. (2018), who used traditional spectral indices to trace the recent SFH in MaNGA galaxies. They found no/weak radial gradients in tracers of recent star formation in low mass galaxies, and were hence unable to support either the inside-out or the outside-in picture. This analysis is hence capable of contributing to the current status of research in this field owing to the improved spatial resolution of the data which thus helps us estimate values for the age gradients. To understand the few exceptions that we see, especially in the case of luminosity/mass weighted age gradients, we analyse the dependence with respect to the galaxy morphology. But before that, we briefly mention two features imperative to the discussion in this section.

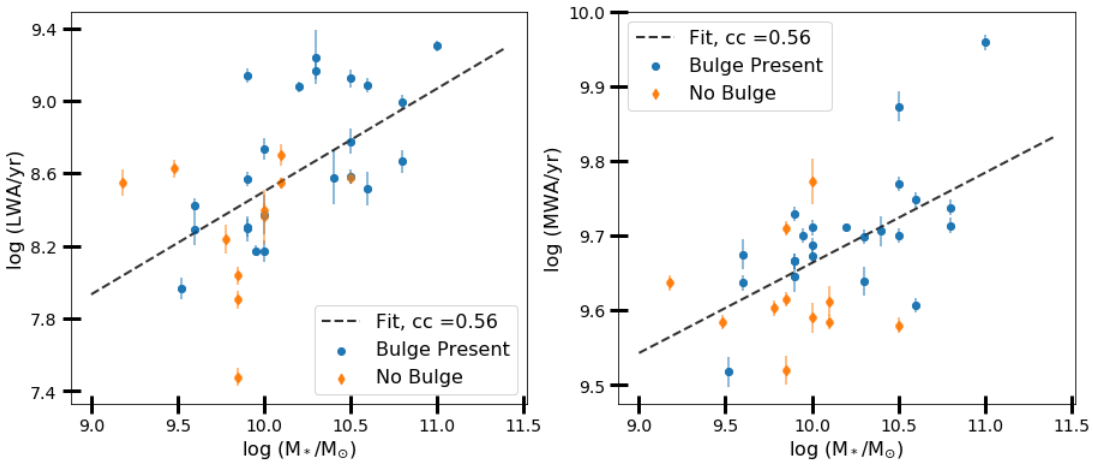

Figure 4.5: Variation of central ages w. r. t. M_* verifying the downsizing argument that massive galaxies are older.

Critical Mass Limit

Previous studies have reported a special mass or mass range around $M_* \sim 10^{10} M_\odot$, referred to as the critical or pivotal mass limit (Kauffmann et al. 2003a; Mateus et al. 2006; Leauthaud et al. 2012). This has been indicated as a special galaxy mass range where the SFR reaches higher values faster. Pan et al. (2015) confirmed that for $M_* < 10^{10.0} M_\odot$ galaxies mainly grow through outside-in mechanism and the importance of the inside-out mode steadily increases with M_*, and becomes dominant at around $M_* > 10^{10.5} M_\odot$. They thus defined a transition zone of $\log M_*/M_\odot \in [10,10.5]$ where the main galaxy assembly mode is transitioning from the outside–in mode to the inside–out mode. This is also in agreement with the mass limit of $M_* \sim 6 \times 10^{10} M_\odot$ estimated by Pérez et al. (2013).

From Figure 4.3, we can see that all the galaxy age gradients above $\log M_* > 10.15$ are seen to be negative without any exceptions. Hence, this study also provides evidence in favor of the critical mass limit and estimates it to about $\log M_*/M_\odot \sim 10.15$.

Downsizing

It is well established that the formation epochs of the stellar populations in galaxies follow a pattern such that the mean stellar age increases and the formation timescale decreases with increasing galaxy mass, which is often referred to as “downsizing”. This has been confirmed with widely different samples and methods for spatially unresolved data (Heavens et al. 2004; Pérez-González et al. 2008; Renzini 2006) and also for spatially resolved data (Pérez et al. 2013; Goddard et al. 2017; González Delgado et al. 2015).

Figure 4.5 depicts the stellar mass vs. stellar age relation for the galaxies of our sample. The ages considered here are estimated at the centre of the galaxies by extending the age gradient fits to 0 R_e. It can be seen from the figure that galaxies with greater stellar mass have a greater mass weighted as well as luminosity weighted age thus confirming the downsizing phenomena.

Hence, this work demonstrates that the stellar mass is the main driver of the global mass growth histories, with more massive galaxies assembling their masses earlier (downsizing). However for a given mass, the global growth histories may show dependence with respect to other galaxy properties like morphological type, which we will explore in the next section.

4.2.2 Effects of galaxy Morphology on age gradients

There have been quite a few studies analysing the importance of morphology in the spatial distribution of stellar ages (González Delgado et al. 2015; Goddard et al. 2017; Rowlands et al. 2018) and in the quenching of galaxies (Bell et al. 2012; Barro et al. 2013; Pan et al. 2014; Woo et al. 2015). Martig et al. (2009) found that the dependence of quenching with morphology is a consequence of the bulge-building mechanism. Bedregal et al. (2011) found outside-in progression for bulge-dominated galaxies i.e., cases where galaxy centres are more metal-rich, and star formation continues in central regions, while it has stopped in the outer regions. While González Delgado et al. (2015) concluded that the stellar population age and its radial variation are more closely linked to morphology than stellar mass, Rowlands et al. (2018) found that whether a spaxel is star forming or not depends on stellar mass and radius, before morphology. Since the galaxies of this sample are mostly late type galaxies, we use the presence or absence of a bulge/bar to differentiate between the morphologies. As discussed before, discontinuities in radial gradients can be seen due to the presence of central sub structures (bar, bulge, disk) in the galaxy. The following points summarise the expectations and the observations due to the presence of a bulge and/or a bar in a galaxy of our sample.

- **Presence of Bulge** : Bulges have been proposed as a possible reason causing the outside-in growth of stellar mass. Wang et al. (2017) studied 77 massive and bulge-dominated galaxies showing outside-in growth. They concluded that the galaxies of their sample were in a transition phase from normal SF to quiescent galaxies with rapid ongoing stellar mass assembly, thus causing bulge growth. Hence presence of bulge is also a possible indication of enhanced SF in the central regions. Since the analysis in this thesis is limited to stellar ages in the galaxy disk, we excluded the bulge region from

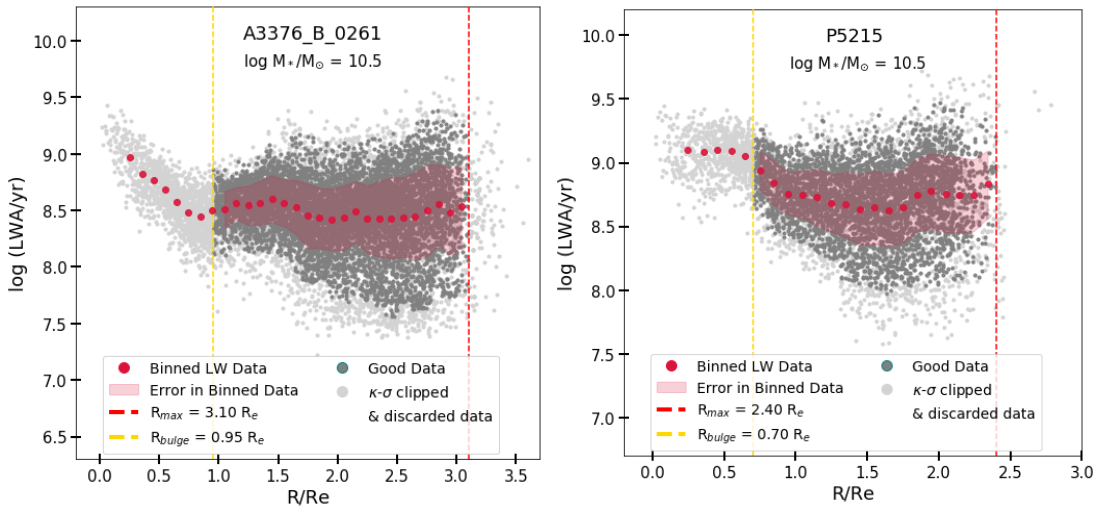

Figure 4.6: Radial age variation for two different galaxies showing the expected high ages and negative gradient in the luminosity weighted age due to the presence of a bulge, in the left panel for A3376_B_0261. In the right panel, the flattening of LW-age can be seen for galaxy P5215 which has a bar present.

our analysis. However, Figure 4.6 (left panel), shows the expected negative age gradient in the bulge and the discontinuity of age profile as we move from bulge to disk for a galaxy from our sample.

- **Presence of Bar** : Bars in galaxies are thought to stimulate both inflow of material and radial mixing along them. The increased inflow of material can cause increased SF in the centre, thus causing alterations to the IO mechanism by continuing to form stars in the centre while the SF in the outskirts has subsided. Further, the radial mixing can cause the bars to show a flat age gradient across them (Sánchez-Blázquez et al. 2009, Roškar et al. 2008). However, the observational evidence for this mixing has been inconclusive so far, limiting the evaluation of the impact of bars on galaxy evolution. The IFS data from GASP can be used to characterise the radial stellar ages along and outside the bar. It was found that age gradients are flatter in the barred regions of almost all the barred galaxies. Our results can thus be interpreted as observational evidence that bars are radially mixing material in galaxies of all stellar masses. Figure 4.6 (right panel), exhibits the radial distribution of stellar age for one of the barred galaxies from our sample.

The presence of breaks similar to those shown in Figure 4.6, lead to our definition of R_{bulge}, which ensured to ignore these central sub structures while analysing the disk age gradients. Similar to the breaks seen in the stellar age profiles, there were also breaks seen in the surface brightness profile, called the broken disk. The broken disk are mostly related to the presence of bars in late type galaxies. The Table 4.3 summarises the presence of these different features seen in the galaxies.

Table 4.3: Table summarising the presence of central substructures (bar/bulge) and breaks in the stellar age and surface brightness profile (broken disk) seen for galaxies of this sample.

Galaxy	Bulge	Bar	Broken Disk	Break in Age profile
A3128_B_0148			✓	
A3266_B_0257	✓		✓	✓
A3376_B_0261	✓			✓
A970_B_0338				✓
JO102	✓		✓	
JO128	✓	✓		
JO138	✓		✓	✓
JO159		✓	✓	
JO17		✓	✓	✓
JO180	✓		✓	✓
JO197			✓	✓
JO205	✓			✓
JO41	✓	✓	✓	✓
JO45			✓	✓
JO5	✓		✓	✓
JO68			✓	
JO73	✓			✓
P13384				✓
P14672	✓			
P15703	✓			✓
P17945				
P19482	✓	✓	✓	✓
P20769			✓	
P20883	✓		✓	✓
P21734	✓	✓		✓
P25500	✓			✓
P42932			✓	✓
P45479	✓	✓	✓	✓
P48157	✓	✓		✓
P5215	✓	✓	✓	✓
P57486	✓	✓	✓	✓
P648	✓	✓		✓
P669	✓			✓
P954	✓	✓		

To administer a comprehensive study of the dependence of age gradients on morphology, the Pearson's correlation coefficients (cc) were adapted. The galaxy sample was divided into two depending on the presence and absence of bulge and the variation of the LWA gradient and MWA gradient wrt to galaxy M_* was studied separately for galaxies with a bugle and otherwise. The findings from Figure 4.7, can be summarised as follows:

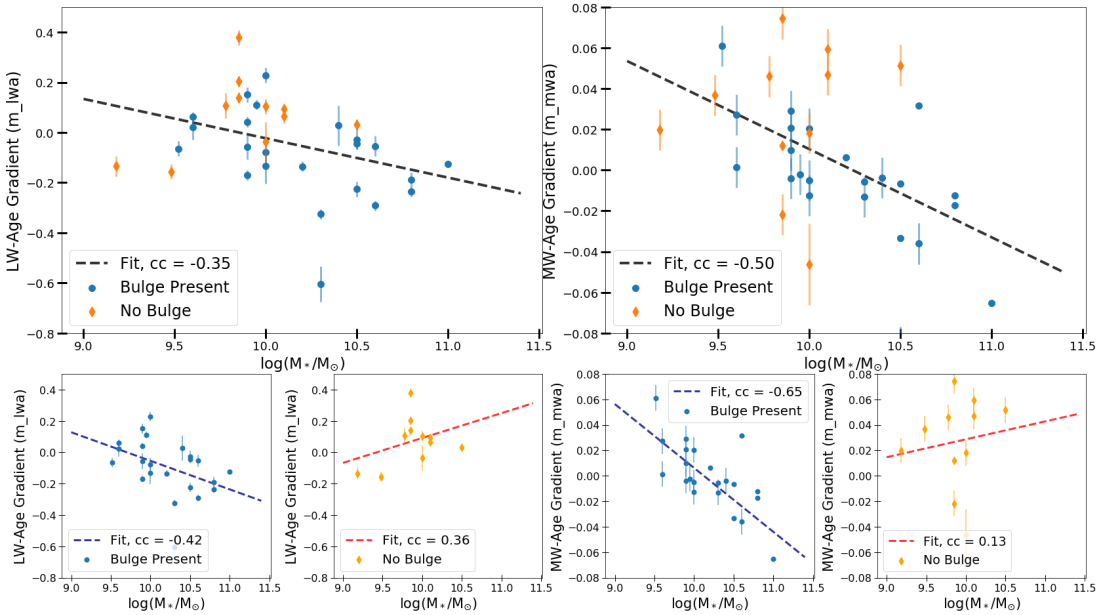

Figure 4.7: Analysing the correlation of LW (left) and MW (right) age gradient for galaxies with and without bulge with the stellar mass separately.

- LWA-gradient vs. M_* ; Overall cc = -0.35
  - Galaxies with Bulge, cc = -0.42
  - Bulgeless Galaxies, cc = 0.36

- MWA-gradient vs. M_* ; Overall cc = -0.50
  - Galaxies with Bulge, cc = -0.65
  - Bulgeless Galaxies, cc = 0.13

As can be seen from the correlation coefficients, for galaxies with a bulge, a stronger negative correlation (as compared to the entire galaxy sample) with the stellar mass is seen. On the contrary, bulgeless galaxies that are plotted separately in the sub panel, show a positive correlation with respect to the M_*. These correlations are seen for both the luminosity and the mass-weighted stellar ages. A deeper analysis is required to understand the origin of these correlations depending on presence/absence of bulges.

We now turn our attention to the galaxies showing inconsistent mass and luminosity weighted age gradients. These are the galaxies presented as the 'mix' category in Table 4.2. We examine the morphology of these galaxies using the photometric decomposition (presented in Table 4.3) and summarise the results in Table 4.4. As can be seen from the table, all the galaxies showing inconsistency also seem to have either a bar or bulge and also a broken disk.

Table 4.4: Table summarising the photometrically decomposed features seen for galaxies showing disagreement between the mass and luminosity weighted age gradients.

Galaxy	LWA_gradient	MWA_gradient	Decomposition
JO45	−	+	Broken Disk
P20769	−	+	Broken Disk
JO205	−	+	Bulge
JO68	+	−	Broken Disk
P13384	+	−	Bulge
P57486	+	−	Bar; Bulge; Broken Disk
JO128	−	+	Bar; Bulge
JO197	−	+	Bar; Bulge

According to the findings of Azzollini et al. (2008), the break due to the presence of a bar seen in surface brightness profile can be matched with a break seen in SF profile and also further the break corresponds to a minimum in the age profile. The Table 4.3 does show agreement between the presence of a broken disk (break in SBP) and the presence of a break in stellar age profiles of some galaxies. However, further evaluation is required to asses if the radial distance of these breaks match and if the age profiles shows an age minimum feature at these radii. Hence, the morphologies do seem to affect the age gradients. However to ascertain if morphologies can serve as an explanation for the inconsistencies seen in the age gradients, a much more detailed analysis is needed. The work in this thesis can be used as a starting step for a significant interpretation of the morphological affects on the age gradients of galaxies.

"Education is the passport to the future, for tomorrow belongs to those who prepare for it today."

- Malcolm X.

5

Summary and Future Outlook

This thesis presents a study of the spatially varying stellar ages and their properties for 34 regular galaxies observed with MUSE as part of the GASP program.

A study of the spatially varying stellar ages can help understand the mechanisms through which galaxies grow their mass thus further elucidating the galaxy evolution process as a whole. A few integral field surveys (CALIFA, MaNGA, SAMI, GASP) have been studying the spatial variation of stellar populations in a galaxy, thus providing significant contributions in this field. The work in this thesis, tries to derive from the existing works and build on it taking advantage of the unique spatial resolution ($\sim 0''.2$/pixel), field of view (~ 5 R_e) and sensitivity of MUSE.

In order to study the variation of stellar populations in the galaxy, the observations were run through a spectrophotometric code, SINOPSIS, which evaluated the best fraction of stellar populations of four different ages, representing the galaxy population. Using these outputs, maps of star formation rate could be produced for four different age bins. Along with this, maps of luminosity-weighted age and mass-weighted age were obtained for each galaxy, which gave the stellar age weighed by flux/mass respectively in each pixel of the galaxy. The structural parameters of the GASP data obtained in the Master thesis of Franchetto et al. (2018), were used. With these values, the radial variation of SFR in the four different age bins, LWA and MWA could be obtained for each galaxy, for a radial distance ranging from the centre to the galaxy outskirts. This radial range was then curbed to consider only the spaxels belonging to the disk region of the galaxy. The breaks seen in stellar age profiles indicated the

presence of central sub-structures like bar or/and a bulge in the galaxies. These breaks were hence used to extend the bulge radius (determined through photometry as $R_{bulge,photo}$) to incorporate these transitions in the stellar age profiles and define a more conservative definition of the bulge radius for this study as R_{bulge}. The galaxy spaxels were binned at steps of 0.1 R_e and a maximum radial limit (R_{max}) was identified to avoid the outer galaxy regions consisting of very few pixels with low signal-to-noise ratio. Hence, to estimate the age gradient of the galaxy disk, only the region between the limits of R_{bulge} and R_{max} was used.

The disk age gradients were computed using the binned values and applying the error-weighted bootstrapped regression technique. Since the distribution of values obtained with 2000 bootstrap repetitions was gaussian, the mean values from the distribution were used. To substantiate the results from this method, the age gradients were also examined using the technique of error-weighted least square regression for the binned points and bootstrapping of all the galaxy spaxels within the above mentioned range. The results from all the three methods were consistent thus proving the reliability of the results and of the method used for computing the age-gradients. Further, the star formation history resolved spatially into annular galaxy regions at steps of 0.5 R_e and resolved in time in 4 different age bins was obtained and analysed for each galaxy. The star formation histories and the age gradient profile for the galaxies together clued up how and where the mass is being built in galaxies through star formation.

The stellar ages were then analysed as a function of radius for the galaxy sample of this thesis. In agreement with the previous studies, two modes of stellar mass growth were observed, viz., the Inside-Out and Outside-In mode. The physical processes giving rise to these two different and opposite scenarios were discussed. While the inside-out progression follows the hierarchical order of galaxy formation, the outside in mechanism poses more novel quests that may help further our understanding of galaxy evolution.

The dependence of these age gradients was studied with respect to the galaxy stellar mass. The stellar mass was divided into four different bins and the age gradients of the galaxies within each bin were observed. A clear reliance was seen and it was concluded that the stellar mass of a galaxy does affect the distribution of the star-forming spaxels and hence influences the stellar ages. The findings show that as the stellar mass increases, the age gradients become increasingly negative thus establishing that while the high mass galaxy show an inside-out growth, the low mass galaxies show an outside-in progression. Above a certain mass limit, estimated as $\log M_*/M_\odot$=10.15, all galaxies ($\sim$12) are seen to show a negative age gradient

(except one) thus supporting the hypothesis of inside-out growth for high mass galaxies. We estimate this limit as the critical mass limit derived from our sample and also reported in earlier literature studies as the mass limit at which a break in stellar properties are reported. However, below this mass limit (which we refer to as low mass galaxies), we find a mix of age gradients. The low mass galaxies, consist of 10 galaxies with negative age gradient, 3 positive gradients and 8 showing a mix of gradients and thus representing the oddities of this sample. Even though many previous studies have hinted at the transition of stellar growth mechanisms from low to high stellar mass galaxies, there have also been studies that have reported the lack of a consistent behavior for the low mass galaxies.

The dependence of age gradients is then also analysed with respect to morphology. This is especially done for the galaxies forming the exception cases and also to understand if the morphology has a role to play in causing the outside-in mechanisms. Investigating the photometry of the 8 galaxies showing opposite slopes for mass-weighted and luminosity-weighted ages, it was found that each of those had a bulge, bar and/or a broken disk. The existence of a broken disk in late type galaxies can be directly correlated to the existence of a bar. The presence of a bulge and/or a bar, can both funnel more gas to the galaxy centres, thus increasing the star formation in the centre of the galaxies while it has already subsided in the outer regions.

The study also presents an almost flat range of mass weighed age gradients (-0.08 to 0.09 dex/R_e) for all galaxies while the luminosity weighted age gradients are comparatively much steeper (-0.7 to 0.4 dex/R_e). This observation can be potentially attributed to the radial migration of stars. Especially in low mass galaxies ($M_* < 10^{10.15}$ $M_\odot$), inflows and outflows of gas can cause strong radial migration of stars, with young stars experiencing the strongest short-timescale migration. The oldest stars will have migrated the furthest because they have experienced more periods of gas inflows/outflows, thus causing a flattening of age gradients. This flattening is also seen for the region of bars in the barred galaxies of our sample, thus testifying the proof of radial mixing in bars.

The galaxy sample also complies with the downsizing argument suggesting that older galaxies are also more massive.

Hence, within the statistical limitations of this sample, it was testified that the mass growth histories of the galaxies are mainly driven by stellar mass. We also see different and opposite correlations for galaxies with and without bulge with respect to the galaxy stellar mass. This points to a certain degree of reliance of the age gradients depending upon the galaxy morphology, which needs significant in-depth analysis for a complete understanding.

This work is a first step in the systematical study of the global stellar population properties of the galaxies. The next step in this analysis can be to statistically enhance the galaxy sample. This study of undisturbed galaxies can be used as a reference for the study of ram pressure stripped galaxies in the GASP sample, which are also called the jellyfish galaxies. The highly resolved integral field spectroscopic data from MUSE can enable a detailed study of these spectacular and complex objects. GASP also observes some post starburst galaxies. These galaxies are interpreted to be in the post-stripping evolutionary stage and are no longer actively forming stars. Hence, extending the study to these galaxies can ensure an overall study of the stellar population properties through the different evolutionary stages.

Most of the future work will focus on the search of physical interpretations capable to explain the observed outside-in growth mechanism and the exceptions seen for the galaxies in this sample.

The observational findings pertaining to the stellar ages of galaxies in this work can be combined with the observations of the metallicity gradients studied by Franchetto et al. (2018). A comparison of these observations to models can provide crucial conclusions. Models of galaxy evolution, encompassing the stellar evolution and the chemical evolution could provide a comparison platform for the observed properties of the regular galaxies. At the same time, hydro-dynamical models of ram-pressure stripping can also be used to further the understanding of jellyfish galaxy features from the observations.

Acknowledgments

I'd like to begin by thanking **Dr. Marco Gullieuszik**, for not just supervising my work but also for being a mentor and a great friend. I was fortunate to have my first research experience with him! He has helped me grow as a researcher with a lot of support and yet with enough freedom to explore my research potential. I'd also want to thank him for standing by and supporting me at every presentation of this thesis, be it in collaboration meetings, in annual retreats or even for my actual defense! I'd also like to thank the GASP team and to Prof. Giulia Rodighiero for supporting my work and reviewing it at every stage. I extend my gratitude to Dr. Paolo Cassata for refereeing my thesis and providing valuable insights to improve it.

I want to express my gratitude to my parents, **Nitin Girdhar** and **Dr. Mukta Girdhar** for always supporting my astrophysical dreams. I dedicate this work to you. Aai and Baba, if it was not for your constant support, it would have been so difficult for me to sustain in a new continent, new country and with new people, everytime. Thank you for always being there! Also a big thanks to my younger sister, **Ananya Girdhar** for keeping me always in touch with Physics with her many doubts and for always taking care of my parents. It is because of your presence that everyday I have slept in peace without having to worry about them.

Further, I want to thank **Dr. Ankur Sharma**, firstly for continuing to tease me for being "just" a Bachelors and for encouraging me to apply for Erasmus scholarships. It actually propelled me towards applying for Masters. And also for always helping me with the application processes for my Masters and PhD until he hadn't ensured I was eventually selected. Thanks for being a support, a friend and an advisor as and when it was needed.

Finally, thanks to this person who made Astromundus sustainable - **Hitesh Lala**! You've supported me at every stage and on every single day. Be it studying together for exams, helping me with my doubts, cooking for me, taking care of me when I was ill, and encouraging me to be a better researcher every time I was in doubt.

To Ankur and Hitesh, thanks for being my family away from home.

A big thanks from the depth of my entire being to Astromundus, University of Innsbruck, University of Padova, University of Belgrade, the committee and the professors. Thank you for giving me an international stage and the experience of living in 3 very different European countries. Every country and every University has contributed to my growth. None of these experiences were possible without the scholarship support. It has helped me train myself, it has given me the chance to learn what I love - Astrophysics with so much excitement and so many opportunities! At last, I thank my mentor, **Dr. Daisaku Ikeda** for encouraging me to become a better person and always reminding me to believe in myself and my dreams.

Thanks to you all, I have taken my first step towards becoming a better Astrophysicist with this thesis.

A
APPENDICES

A.1 **APPENDIX A:** Plots for all galaxies

The Appendix presents the following plots for all the 34 galaxies of the sample:

1. The Star Formation radial profiles in 4 different age bins
2. The Stellar Age profiles for luminosity-weighted and mass-weighted ages with the estimated gradient plotted for the disk
3. The spatially varying SFH resolved in 4 different age bins

1. **Galaxy A3376_B_0261**; Stellar Mass, log $M_*/M_\odot = 10.50$

Since all plots are already presented in Chapter 3 and Chapter 4, they are not included here.

2. **Galaxy A3128_B_0148**; Stellar Mass, log $M_*/M_\odot$ = 9.85

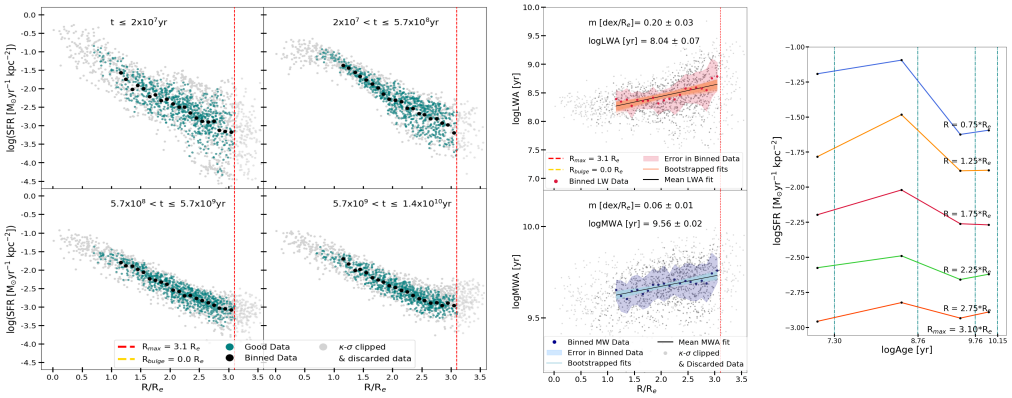

3. **Galaxy A3266_B_0257**; Stellar Mass, log $M_*/M_\odot$ = 9.90

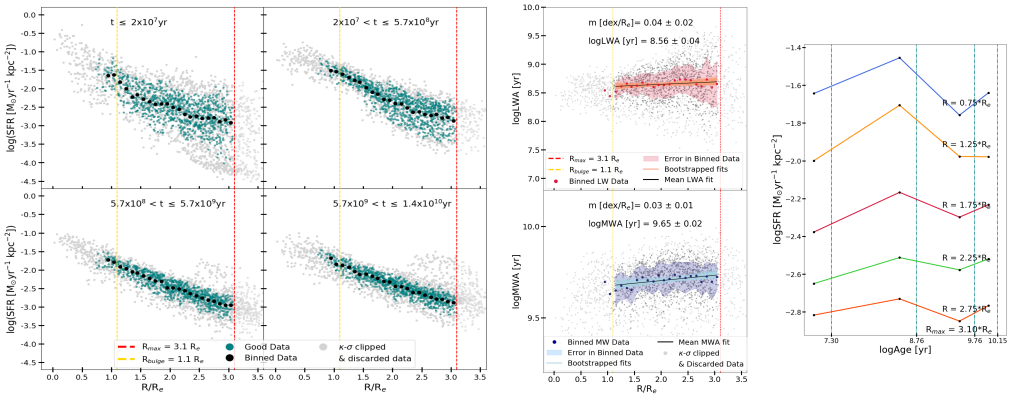

4. **Galaxy A970_B_0338**; Stellar Mass, log $M_*/M_\odot$ = 10.10

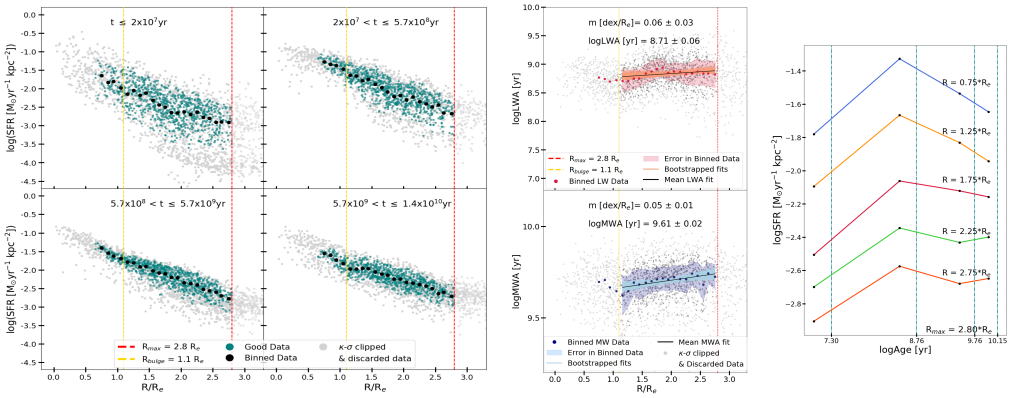

5. **Galaxy JO102**; Stellar Mass, log $M_*/M_\odot$ = 10.00

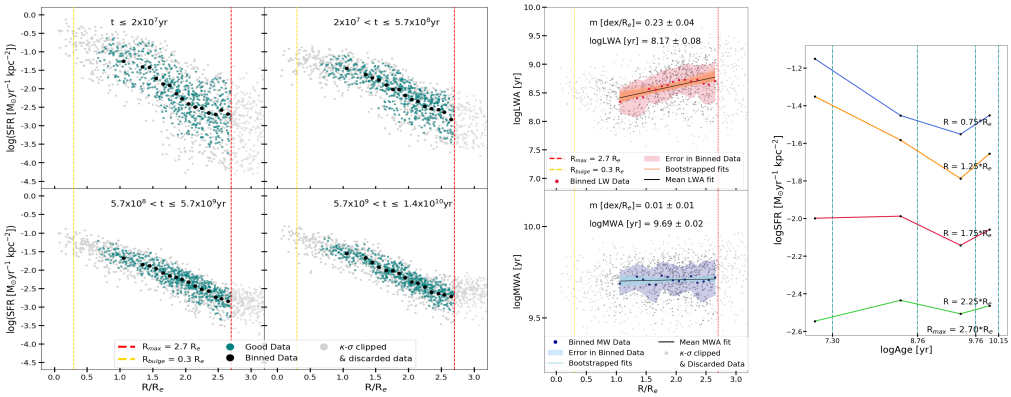

6. **Galaxy JO128**; Stellar Mass, log $M_*/M_\odot$ = 9.90

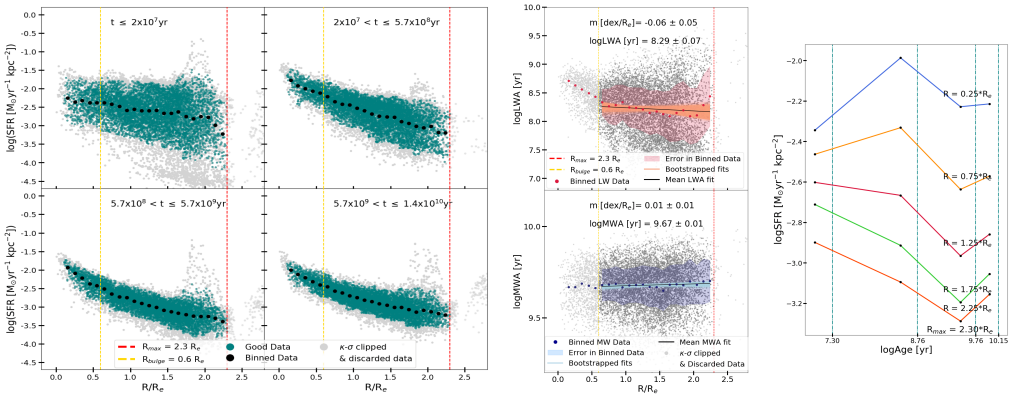

7. **Galaxy JO138**; Stellar Mass, log $M_*/M_\odot$ = 9.60

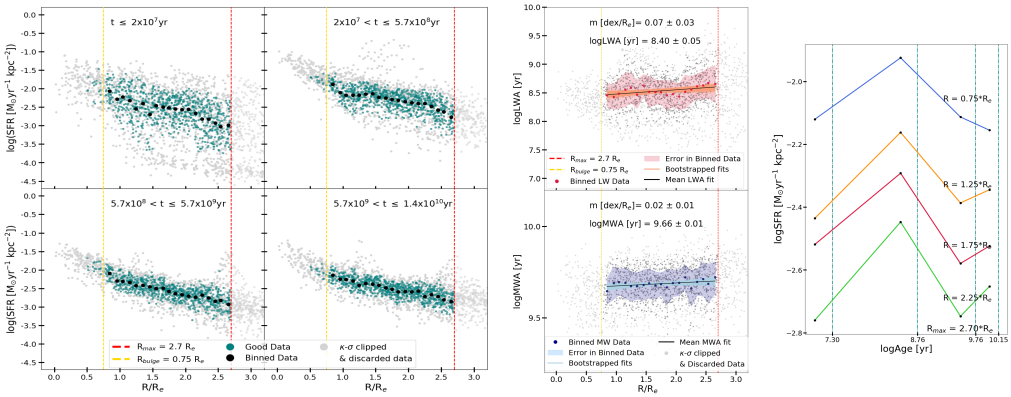

8. **Galaxy JO159**; Stellar Mass, log $M_*/M_\odot$ = 9.85

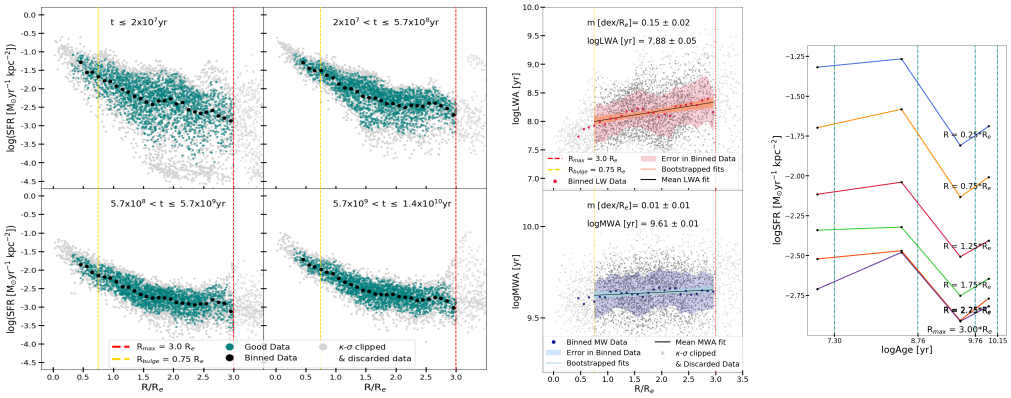

9. **Galaxy JO17**; Stellar Mass, log $M_*/M_\odot$ = 10.10

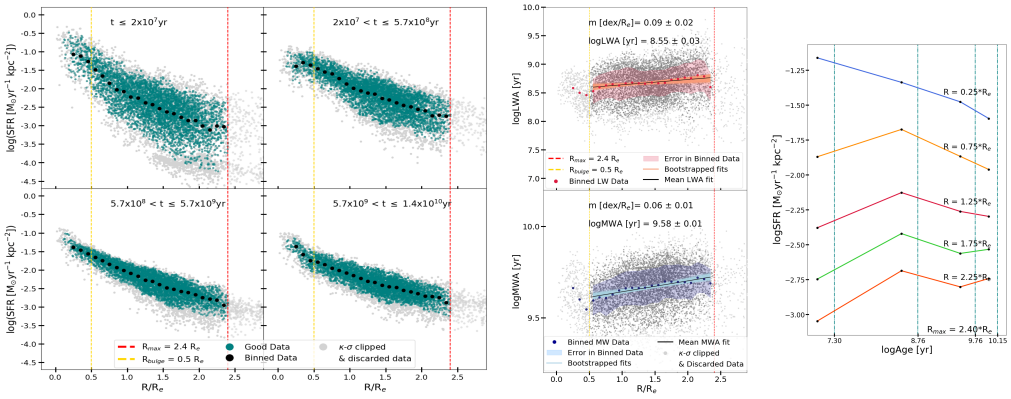

10. **Galaxy JO180**; Stellar Mass, log $M_*/M_\odot$ = 10.00

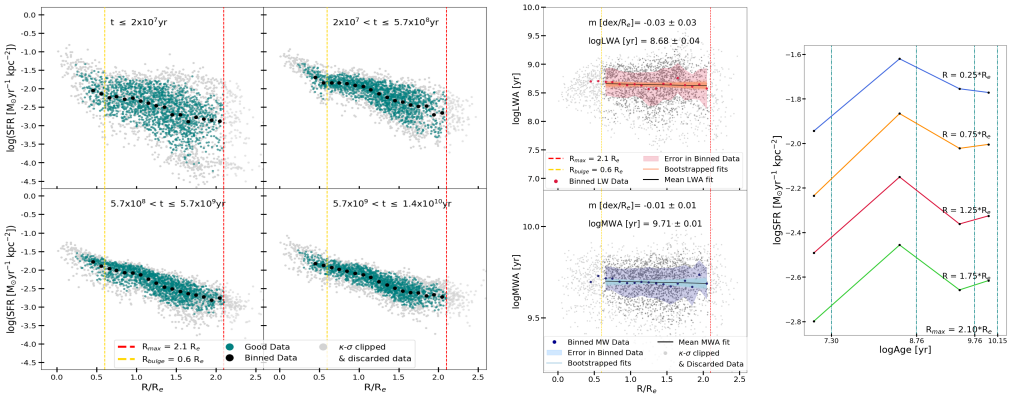

11. **Galaxy JO197**; Stellar Mass, log $M_*/M_\odot = 10.00$

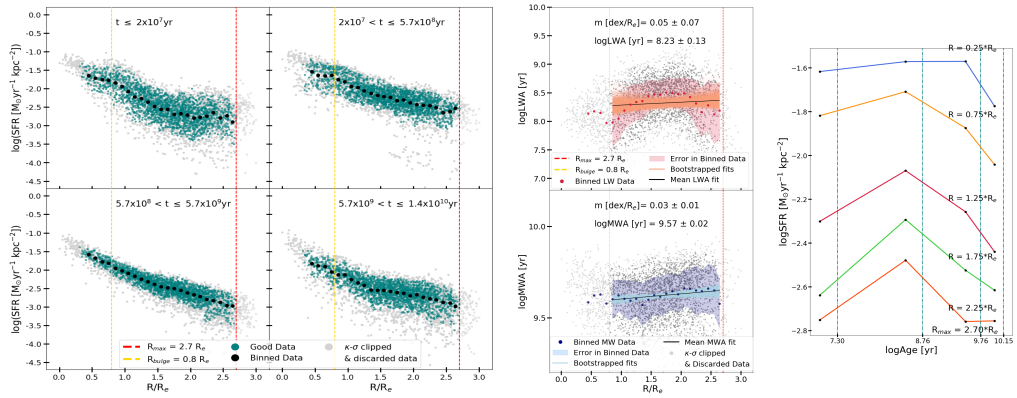

12. **Galaxy JO205**; Stellar Mass, log $M_*/M_\odot = 9.52$

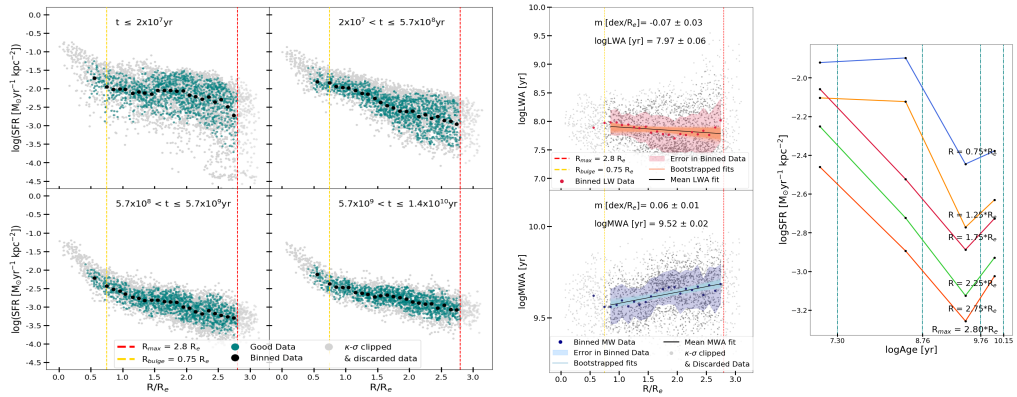

13. **Galaxy JO41**; Stellar Mass, log $M_*/M_\odot = 10.20$

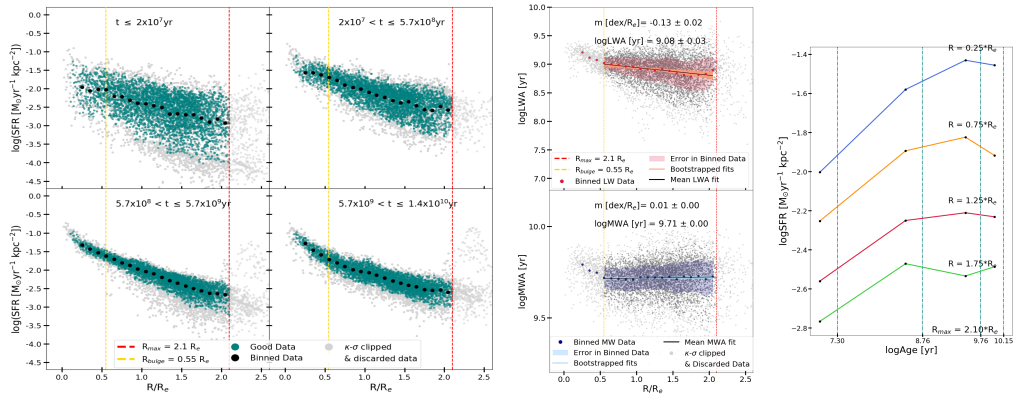

14. **Galaxy JO45**; Stellar Mass, log $M_*/M_\odot$ = 9.18

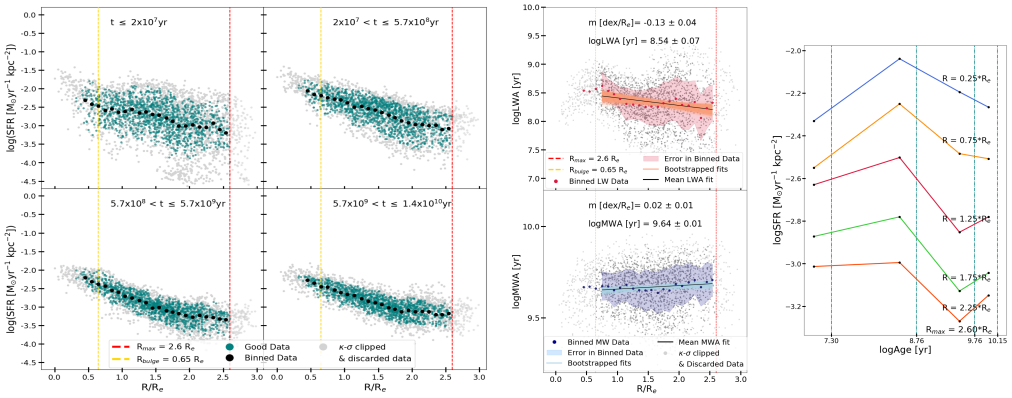

15. **Galaxy JO5**; Stellar Mass, log $M_*/M_\odot$ = 10.30

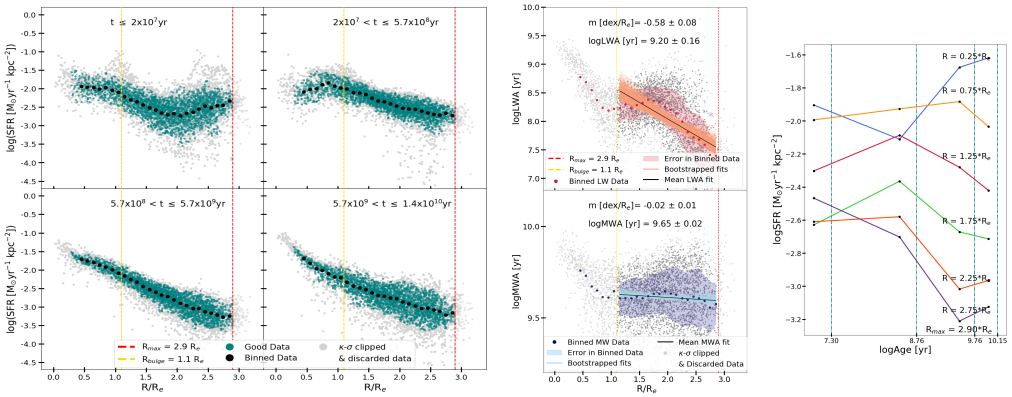

16. **Galaxy JO68**; Stellar Mass, log $M_*/M_\odot$ = 10.00

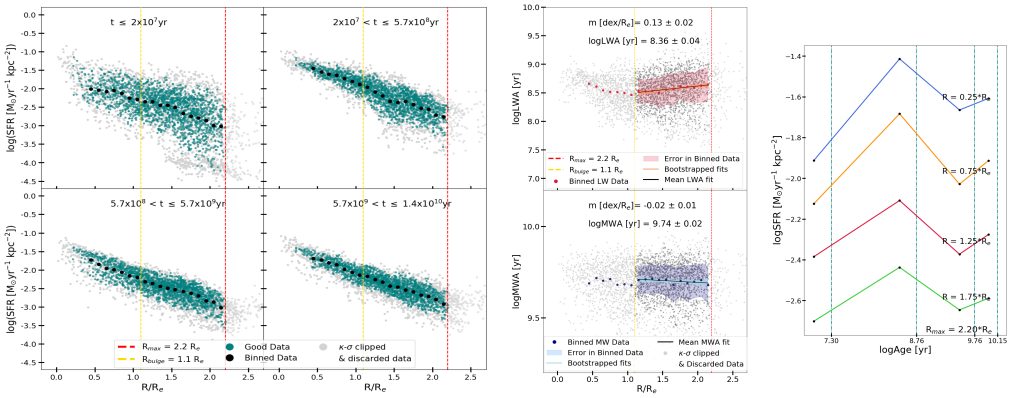

17. **Galaxy JO73**; Stellar Mass, log $M_*/M_\odot$ = 10.00

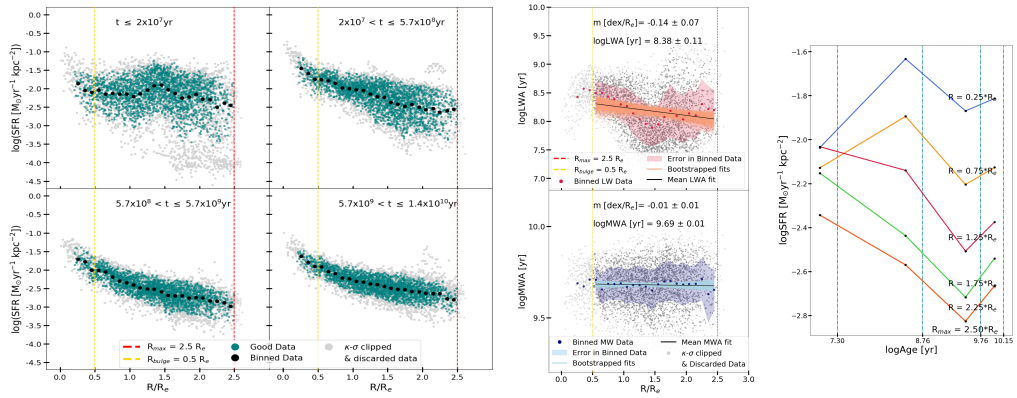

18. **Galaxy P13384**; Stellar Mass, log $M_*/M_\odot$ = 9.85

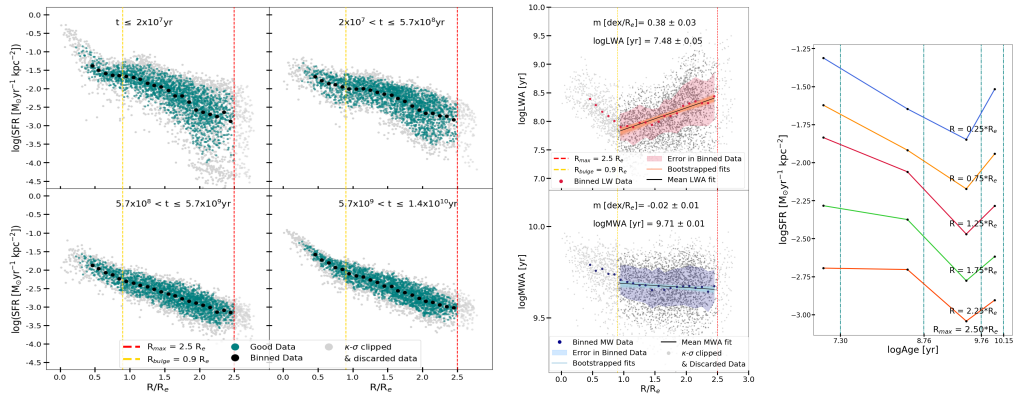

19. **Galaxy P14672**; Stellar Mass, log $M_*/M_\odot$ = 9.90

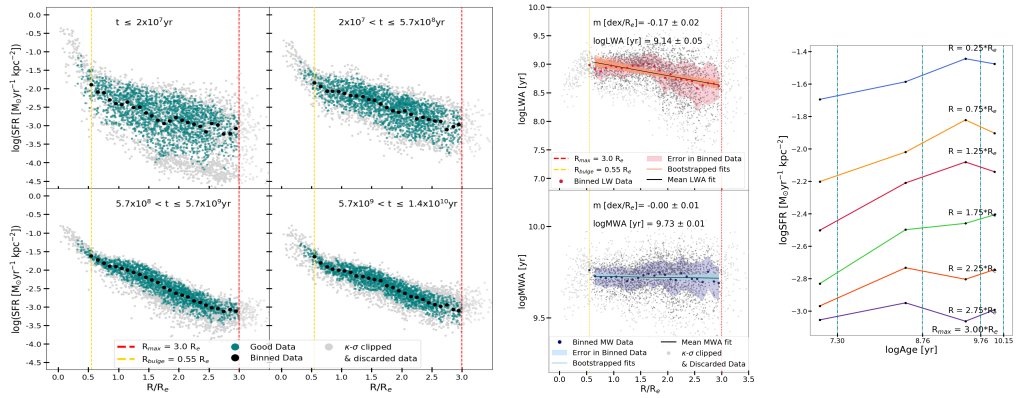

20. **Galaxy P15703**; Stellar Mass, log $M_*/M_\odot$ = 11.00

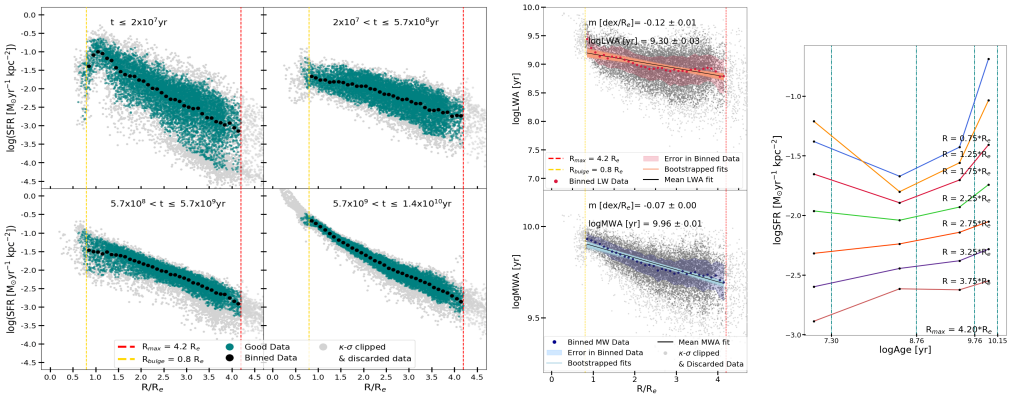

21. **Galaxy P17945**; Stellar Mass, log $M_*/M_\odot$ = 9.78

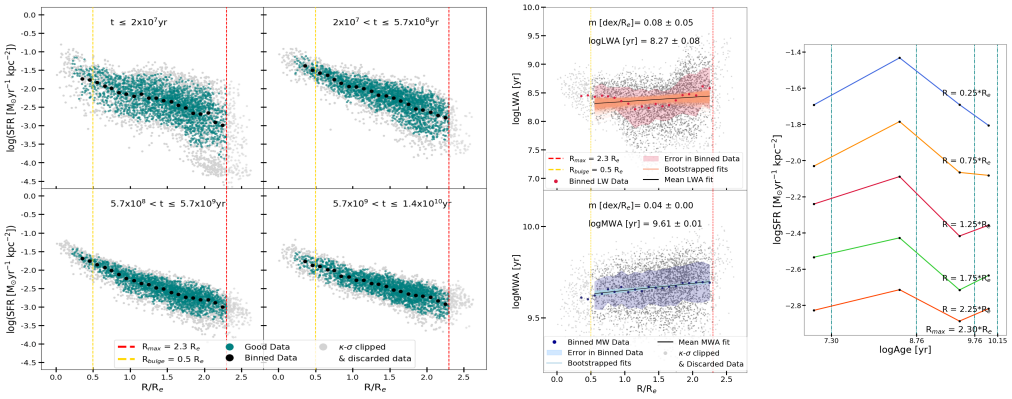

22. **Galaxy P19482**; Stellar Mass, log $M_*/M_\odot$ = 10.30

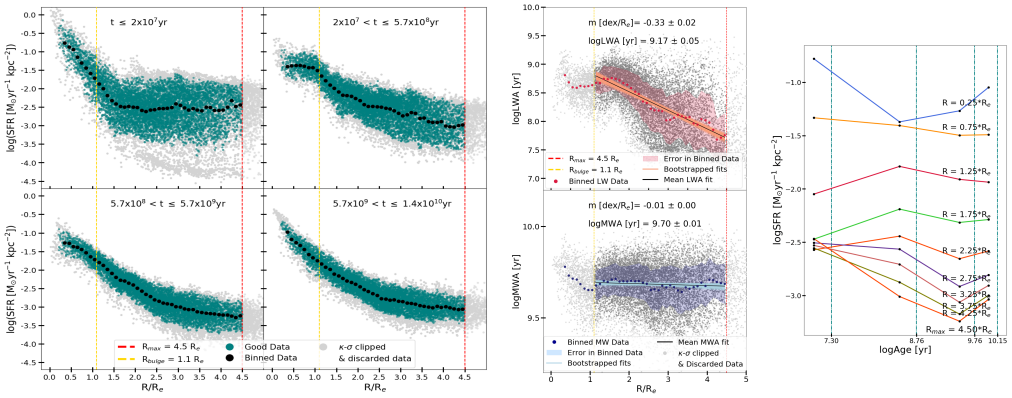

23. **Galaxy P20769**; Stellar Mass, log $M_*/M_\odot$ = 9.48

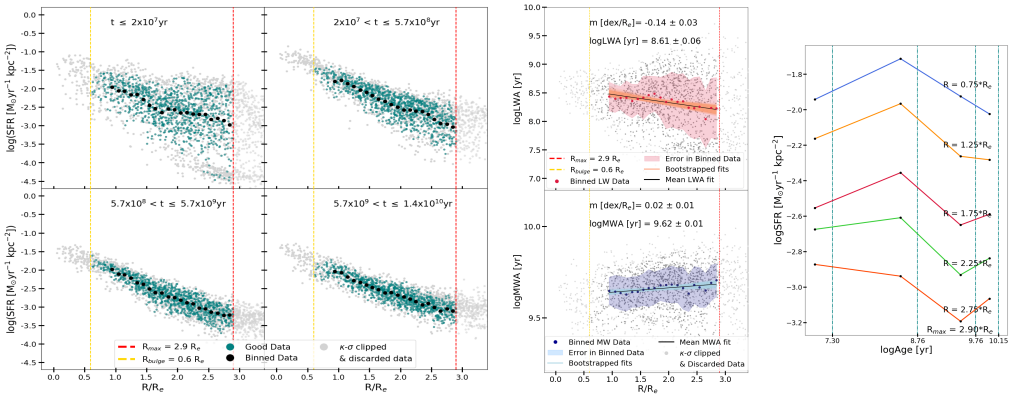

24. **Galaxy P20883**; Stellar Mass, log $M_*/M_\odot$ = 9.90

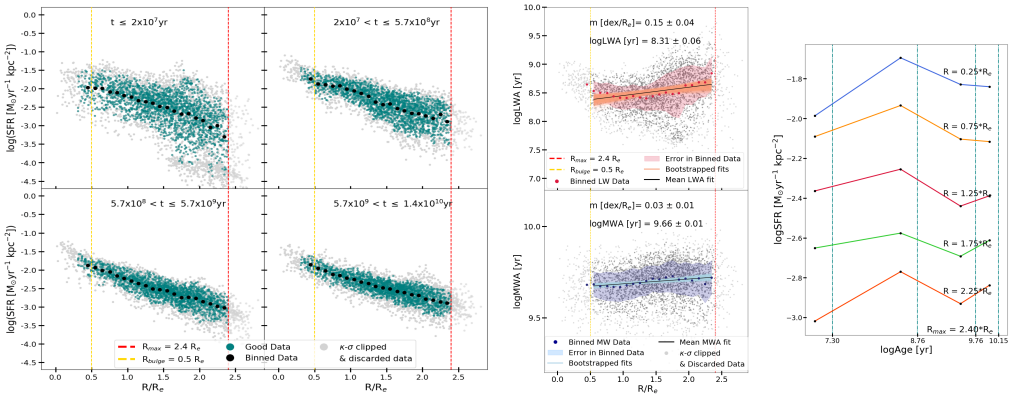

25. **Galaxy P21734**; Stellar Mass, log $M_*/M_\odot$ = 10.80

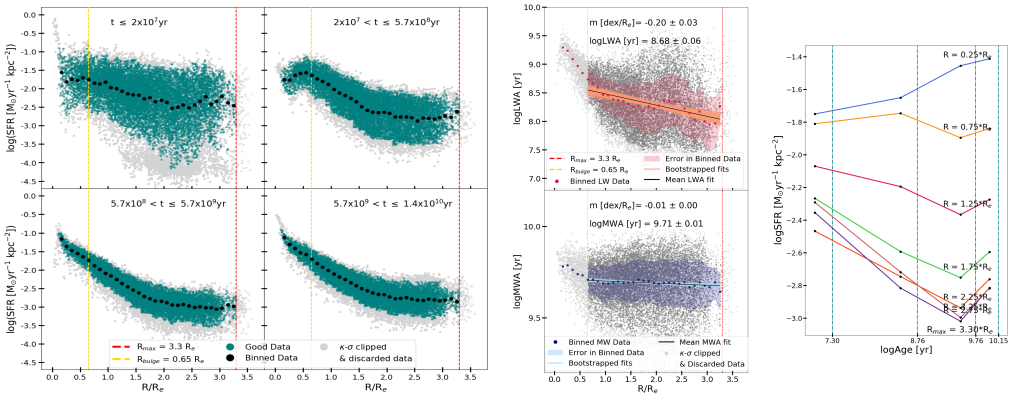

26. **Galaxy P25500**; Stellar Mass, $\log M_*/M_\odot = 10.80$

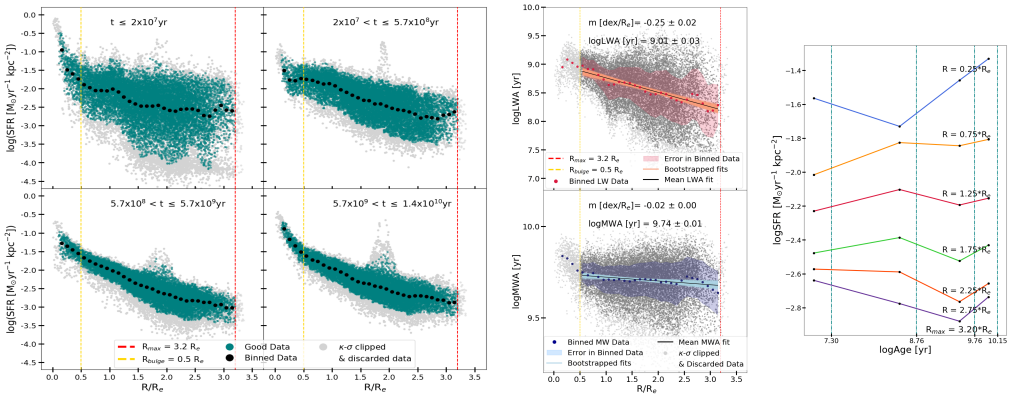

27. **Galaxy P42932**; Stellar Mass, $\log M_*/M_\odot = 10.50$

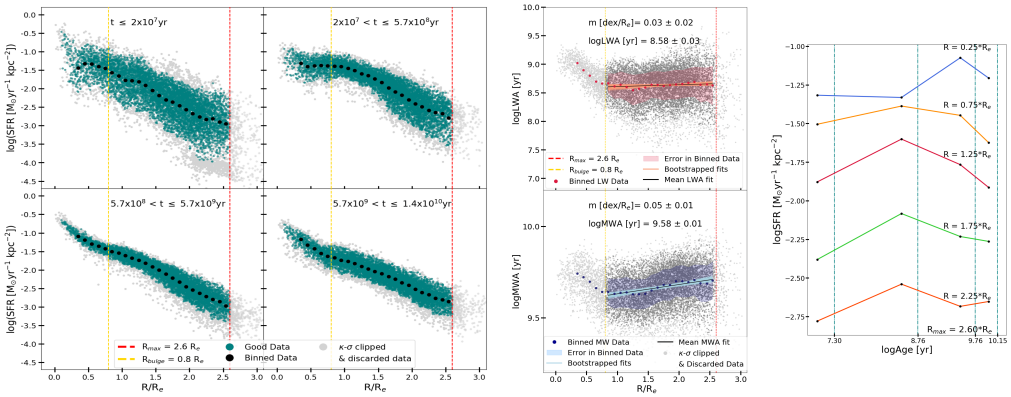

28. **Galaxy P45479**; Stellar Mass, $\log M_*/M_\odot = 10.60$

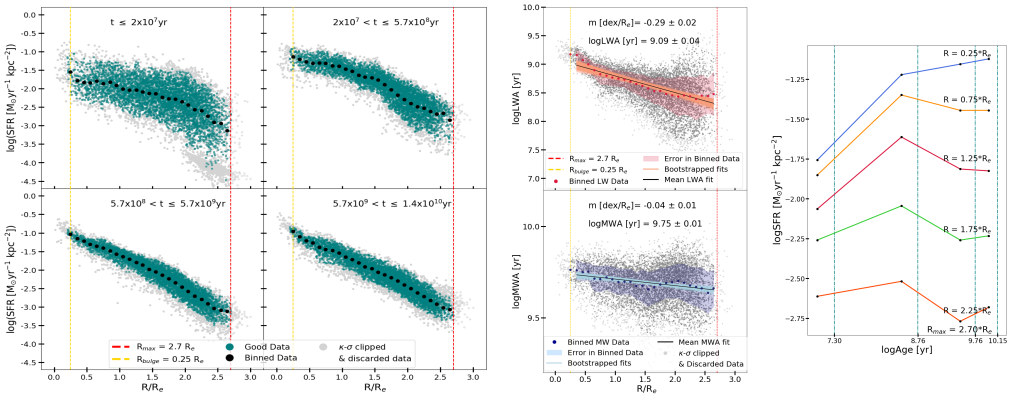

29. **Galaxy P48157**; Stellar Mass, log $M_*/M_\odot$ = 10.60

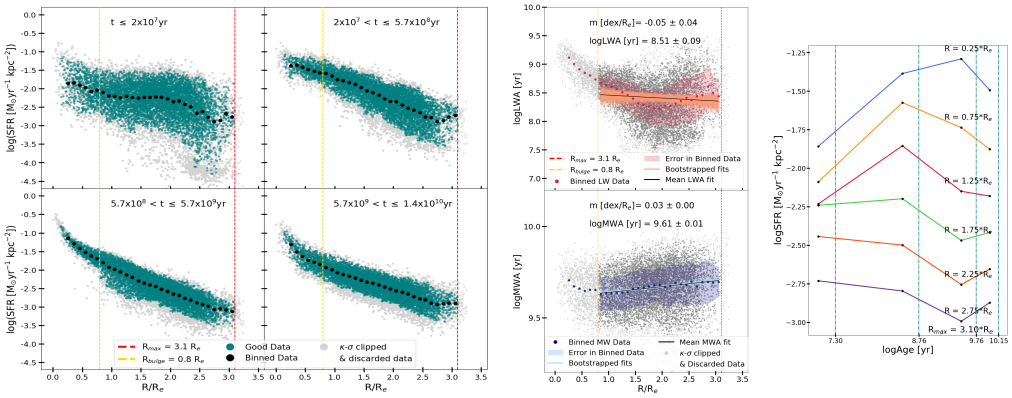

30. **Galaxy P5215**; Stellar Mass, log $M_*/M_\odot$ = 10.50

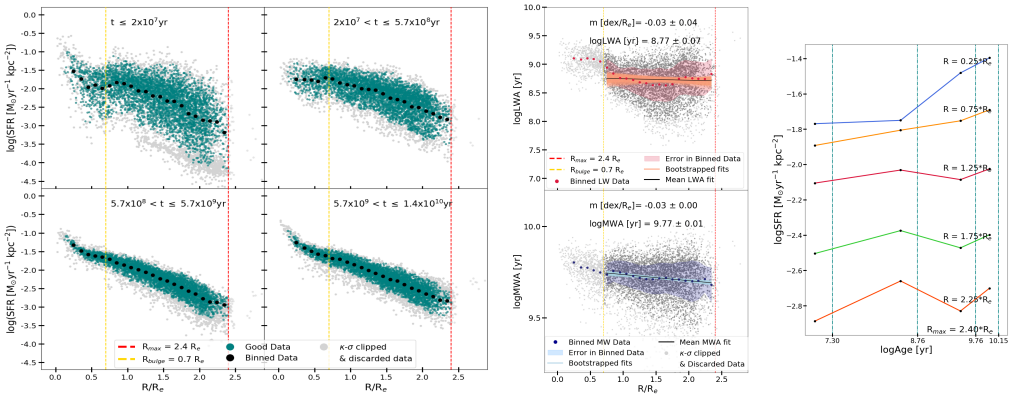

31. **Galaxy P57486**; Stellar Mass, log $M_*/M_\odot$ = 9.95

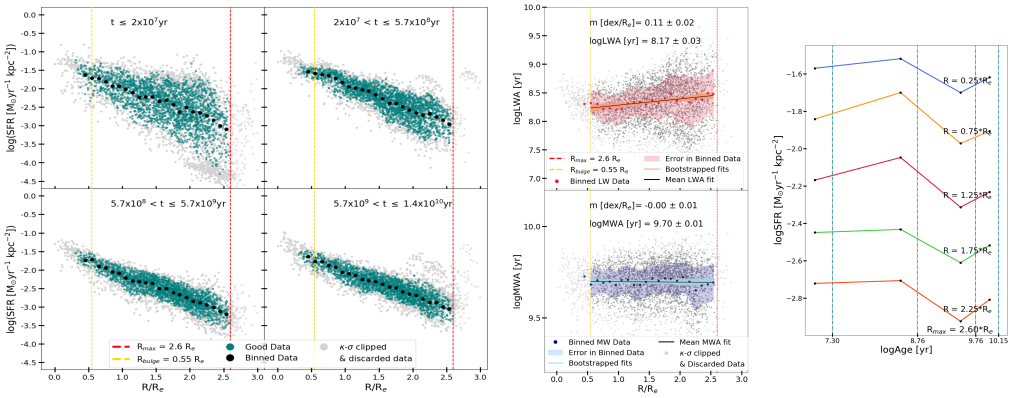

32. **Galaxy P648**; Stellar Mass, $\log M_*/M_\odot = 10.40$

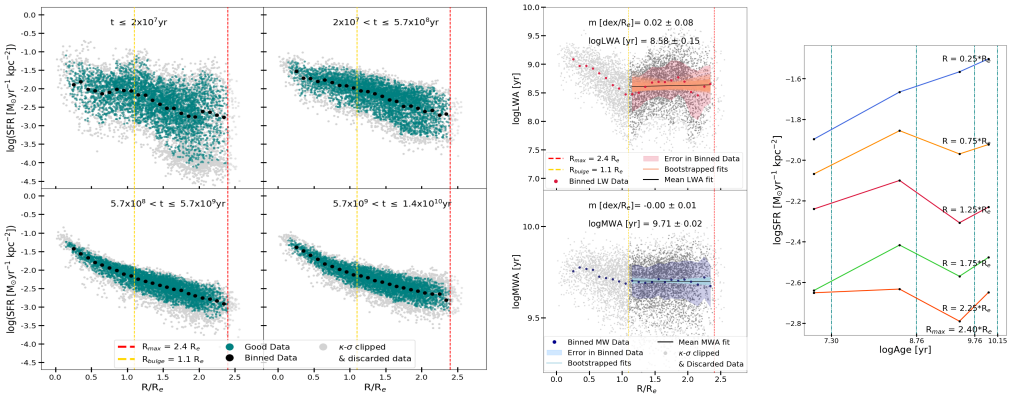

33. **Galaxy P669**; Stellar Mass, $\log M_*/M_\odot = 10.50$

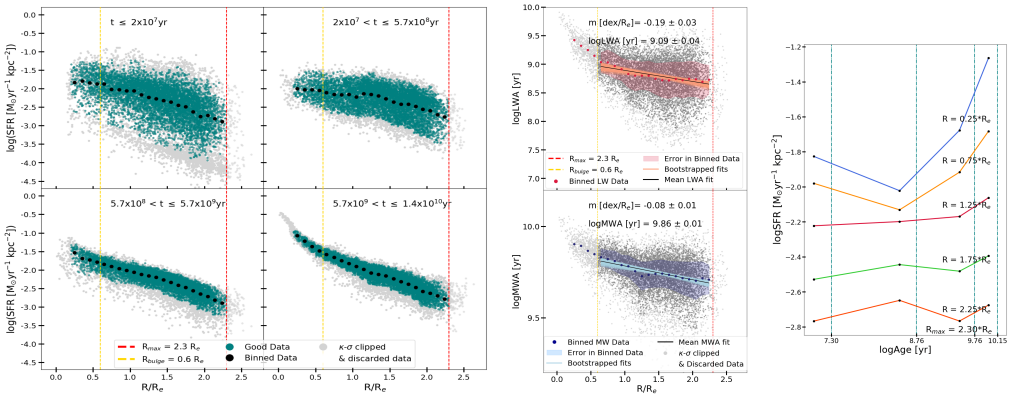

34. **Galaxy P954**; Stellar Mass, $\log M_*/M_\odot = 9.60$

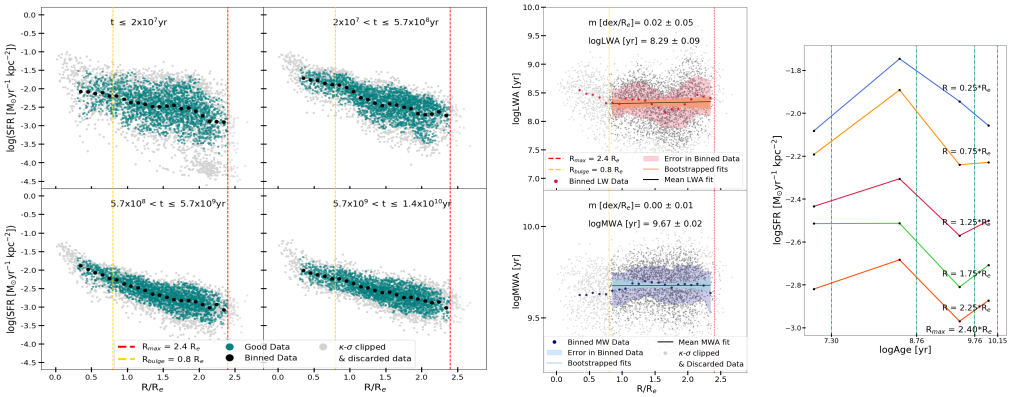

References

Aumer M., White S. D. M., Naab T., 2014, MNRAS, 441, 3679

Azzollini R., Trujillo I., Beckman J. E., 2008, in Funes J. G., Corsini E. M., eds, Astronomical Society of the Pacific Conference Series Vol. 396, Formation and Evolution of Galaxy Disks. p. 417

Bacon R., et al., 2001, MNRAS, 326, 23

Bacon R., et al., 2010, in Proc. SPIE. p. 773508, doi:10.1117/12.856027

Barro G., et al., 2013, ApJ, 765, 104

Bedregal A. G., Cardiel N., Aragón-Salamanca A., Merrifield M. R., 2011, MNRAS, 415, 2063

Bell E. F., de Jong R. S., 2000, MNRAS, 312, 497

Bell E. F., et al., 2012, ApJ, 753, 167

Bellhouse C., et al., 2017, ApJ, 844, 49

Bernard E. J., Aparicio A., Gallart C., Padilla-Torres C. P., Panniello M., 2007, AJ, 134, 1124

Bershady M. A., Verheijen M. A. W., Swaters R. A., Andersen D. R., Westfall K. B., Martinsson T., 2010, ApJ, 716, 198

Bezanson R., van Dokkum P. G., Tal T., Marchesini D., Kriek M., Franx M., Coppi P., 2009, ApJ, 697, 1290

Blanton M. R., et al., 2017, AJ, 154, 28

Bournaud F., et al., 2014, ApJ, 780, 57

Bressan A., Marigo P., Girardi L., Salasnich B., Dal Cero C., Rubele S., Nanni A., 2012, MNRAS, 427, 127

Brinchmann J., Charlot S., White S. D. M., Tremonti C., Kauffmann G., Heckman T., Brinkmann J., 2004, MNRAS, 351, 1151

Brough S., et al., 2013, MNRAS, 435, 2903

Bryant J. J., et al., 2015, MNRAS, 447, 2857

Bundy K., et al., 2015, ApJ, 798, 7

Calvi R., Poggianti B. M., Vulcani B., 2011, MNRAS, 416, 727

Calvi R., Poggianti B. M., Fasano G., Vulcani B., 2012, MNRAS, 419, L14

Calzetti D., Kinney A. L., Storchi-Bergmann T., 1994, ApJ, 429, 582

Cappellari M., Emsellem E., 2004, PASP, 116, 138

Cappellari M., et al., 2011, MNRAS, 413, 813

Cardelli J. A., Clayton G. C., Mathis J. S., 1989, ApJ, 345, 245

Chabrier G., 2003, PASP, 115, 763

Citro A., Pozzetti L., Moresco M., Cimatti A., 2016, A&A, 592, A19

Croom S. M., et al., 2012, MNRAS, 421, 872

Dale D. A., et al., 2016, AJ, 151, 4

Davies R. L., et al., 2001, ApJ, 548, L33

Davies L. J. M., et al., 2016, MNRAS, 461, 458

Dekel A., Burkert A., 2014, MNRAS, 438, 1870

Driver S. P., et al., 2009, Astronomy and Geophysics, 50, 5.12

Driver S. P., et al., 2011, MNRAS, 413, 971

Drory N., et al., 2015, AJ, 149, 77

Ebeling H., Stephenson L. N., Edge A. C., 2014, ApJ, 781, L40

El-Badry K., Wetzel A., Geha M., Hopkins P. F., Kereš D., Chan T. K., Faucher-Giguère C.-A., 2016, ApJ, 820, 131

Ellison S. L., Nair P., Patton D. R., Scudder J. M., Mendel J. T., Simard L., 2011, MNRAS, 416, 2182

Faber S. M., Dressler A., 1977, AJ, 82, 187

Fang J. J., Faber S. M., Salim S., Graves G. J., Rich R. M., 2012, ApJ, 761, 23

Fasano G., et al., 2006, A&A, 445, 805

Fasano G., et al., 2012, MNRAS, 420, 926

Ferland G. J., et al., 2013, Rev. Mexicana Astron. Astrofis., 49, 137

Ferrers N., 1877, QJ Pure Appl. Math, 14, 1

Fossati M., Fumagalli M., Boselli A., Gavazzi G., Sun M., Wilman D. J., 2016, MNRAS, 455, 2028

Franchetto A., Master Thesis Universita degli Studi di Padova Supervisors: Poggianti B., Rodighiero G., Gullieuszik M., 2018

Fraser-McKelvie A., et al., 2019, MNRAS, 488, L6

Fritz J., et al., 2007, A&A, 470, 137

Fritz J., et al., 2011, A&A, 526, A45

Fritz J., et al., 2017, ApJ, 848, 132

Fumagalli M., Fossati M., Hau G. K. T., Gavazzi G., Bower R., Sun M., Boselli A., 2014, MNRAS, 445, 4335

Gallart C., Stetson P. B., Meschin I. P., Pont F., Hardy E., 2008, ApJ, 682, L89

Gallazzi A., Charlot S., Brinchmann J., White S. D. M., Tremonti C. A., 2005, MNRAS, 362, 41

García-Benito R., et al., 2015, A&A, 576, A135

George K., et al., 2018, MNRAS, 479, 4126

George K., et al., 2019, MNRAS, 487, 3102

Girardi L., Bressan A., Bertelli G., Chiosi C., 2000, A&AS, 141, 371

Goddard D., et al., 2017, MNRAS, 466, 4731

González Delgado R. M., et al., 2015, A&A, 581, A103

González Delgado R. M., et al., 2016, A&A, 590, A44

González Delgado R. M., et al., 2017, A&A, 607, A128

Gullieuszik M., et al., 2015, A&A, 581, A41

Gullieuszik M., et al., 2017, ApJ, 846, 27

Gunn J. E., Gott J. Richard I., 1972, ApJ, 176, 1

Gunn J. E., et al., 2006, AJ, 131, 2332

Heavens A., Panter B., Jimenez R., Dunlop J., 2004, Nature, 428, 625

Huang M.-L., Kauffmann G., Chen Y.-M., Moran S. M., Heckman T. M., Davé R., Johansson J., 2013, MNRAS, 431, 2622

Husemann B., et al., 2013, A&A, 549, A87

Ibarra-Medel H. J., et al., 2016, MNRAS, 463, 2799

Jablonka P., Gorgas J., Goudfrooij P., 2007, A&A, 474, 763

Jaffé Y. L., et al., 2018, MNRAS, 476, 4753

Jedrzejewski R. I., 1987, in de Zeeuw P. T., ed., IAU Symposium Vol. 127, Structure and Dynamics of Elliptical Galaxies. pp 37–46, doi:10.1007/978-94-009-3971-4_3

Kauffmann G., White S. D. M., Guiderdoni B., 1993, MNRAS, 264, 201

Kauffmann G., et al., 2003a, MNRAS, 341, 33

Kauffmann G., et al., 2003b, MNRAS, 346, 1055

Kelz A., et al., 2006, PASP, 118, 129

Kewley L. J., Jansen R. A., Geller M. J., 2005, PASP, 117, 227

Leauthaud A., et al., 2012, ApJ, 744, 159

Li C., et al., 2015, ApJ, 804, 125

Lin L., Zou H., Kong X., Lin X., Mao Y., Cheng F., Jiang Z., Zhou X., 2013, ApJ, 769, 127

Lin L., et al., 2019, ApJ, 872, 50

Liu G., et al., 2013, ApJ, 778, L41

Maraston C., Pforr J., Renzini A., Daddi E., Dickinson M., Cimatti A., Tonini C., 2010, MNRAS, 407, 830

Markwardt C. B., 2009, in Bohlender D. A., Durand D., Dowler P., eds, Astronomical Society of the Pacific Conference Series Vol. 411, Astronomical Data Analysis Software and Systems XVIII. p. 251 (***arXiv:0902.2850***)

Martel H., Kawata D., Ellison S. L., 2013, MNRAS, 431, 2560

Martig M., Bournaud F., Teyssier R., Dekel A., 2009, ApJ, 707, 250

Mateus A., Sodré L., Cid Fernand es R., Stasińska G., Schoenell W., Gomes J. M., 2006, MNRAS, 370, 721

Mo H. J., Mao S., White S. D. M., 1998, MNRAS, 295, 319

Moran S. M., et al., 2012, ApJ, 745, 66

Morelli L., Corsini E. M., Pizzella A., Dalla Bontà E., Coccato L., Méndez-Abreu J., Cesetti M., 2012, The Messenger, 149, 28

Morelli L., Pizzella A., Corsini E. M., Dalla Bontà E., Coccato L., Méndez-Abreu J., Parmiggiani M., 2015, Astronomische Nachrichten, 336, 208

Moretti A., et al., 2014, A&A, 564, A138

Moretti A., et al., 2018, MNRAS, 475, 4055

Muñoz-Mateos J. C., Gil de Paz A., Boissier S., Zamorano J., Jarrett T., Gallego J., Madore B. F., 2007, ApJ, 658, 1006

Nelson E. J., et al., 2012, ApJ, 747, L28

Nelson E. J., et al., 2013, ApJ, 763, L16

Nelson E. J., et al., 2016, ApJ, 828, 27

Pan Z., Li J., Lin W., Wang J., Kong X., 2014, ApJ, 792, L4

Pan Z., Li J., Lin W., Wang J., Fan L., Kong X., 2015, ApJ, 804, L42

Patel S. G., et al., 2013, ApJ, 766, 15

Pérez-González P. G., et al., 2008, ApJ, 675, 234

Pérez E., et al., 2013, ApJ, 764, L1

Poggianti B. M., et al., 2016, AJ, 151, 78

Poggianti B. M., et al., 2017a, Nature, 548, 304

Poggianti B. M., et al., 2017b, ApJ, 844, 48

Poggianti B. M., et al., 2019, MNRAS, 482, 4466

Pracy M. B., Owers M. S., Couch W. J., Kuntschner H., Bekki K., Briggs F., Lah P., Zwaan M., 2012, MNRAS, 420, 2232

Radovich M., Poggianti B., Jaffé Y. L., Moretti A., Bettoni D., Gullieuszik M., Vulcani B., Fritz J., 2019, MNRAS, 486, 486

Rawle T. D., et al., 2014, MNRAS, 442, 196

Renzini A., 2006, ARA&A, 44, 141

Richards S. N., et al., 2016, MNRAS, 455, 2826

Rodriguez-Gomez V., et al., 2016, MNRAS, 458, 2371

Roth M. M., Schönberner D., Steffen M., Monreal A., Sandin C., 2006, in Barlow M. J., Méndez R. H., eds, IAU Symposium Vol. 234, Planetary Nebulae in our Galaxy and Beyond. pp 17–20, doi:10.1017/S1743921306002699

Roškar R., Debattista V. P., Stinson G. S., Quinn T. R., Kaufmann T., Wadsley J., 2008, ApJ, 675, L65

Rowlands K., et al., 2018, MNRAS, 480, 2544

SDSS Collaboration Albareti F. D., et al., 2017, ApJS, 233, 25

Sánchez-Blázquez P., Courty S., Gibson B. K., Brook C. B., 2009, MNRAS, 398, 591

Sánchez-Blázquez P., et al., 2014, A&A, 570, A6

Sánchez S. F., et al., 2012, A&A, 538, A8

Sánchez S. F., et al., 2016, A&A, 594, A36

Schlafly E. F., Finkbeiner D. P., 2011, ApJ, 737, 103

Schneider P., 2006, Extragalactic Astronomy and Cosmology

Sersic J. L., 1968, Atlas de Galaxias Australes

Smee S. A., et al., 2013, AJ, 146, 32

Tacchella S., et al., 2015, Science, 348, 314

Tacchella S., Dekel A., Carollo C. M., Ceverino D., DeGraf C., Lapiner S., Mand elker N., Primack J. R., 2016, MNRAS, 458, 242

Vazdekis A., Sánchez-Blázquez P., Falcón-Barroso J., Cenarro A. J., Beasley M. A., Cardiel N., Gorgas J., Peletier R. F., 2010, MNRAS, 404, 1639

Vulcani B., et al., 2018, ApJ, 866, L25

Wang J., et al., 2011, MNRAS, 412, 1081

Wang E., Kong X., Wang H., Wang L., Lin L., Gao Y., Liu Q., 2017, ApJ, 844, 144

Wang E., et al., 2018, ApJ, 856, 137

White S. D. M., Frenk C. S., 1991, ApJ, 379, 52

Woo J., Dekel A., Faber S. M., Koo D. C., 2015, MNRAS, 448, 237

Wuyts S., et al., 2012, ApJ, 753, 114

Zhang H.-X., Hunter D. A., Elmegreen B. G., Gao Y., Schruba A., 2012, AJ, 143, 47

Zheng Z., et al., 2017, MNRAS, 465, 4572

van de Sande J., et al., 2013, ApJ, 771, 85